

Doctoral Dissertation (Censored)

博士論文 (要約)

Synthesis of Large Curved Nanocarbon Molecules by a Polygon Assembling Strategy  
(多角形組立戦略による大型湾曲ナノカーボン分子の合成)

A Dissertation Submitted for the Degree of Doctor of Philosophy

December 2021

令和3年12月博士(理学)申請

Department of Chemistry, Graduate School of Science,

The University of Tokyo

東京大学大学院理学系研究科化学専攻

Tatsuru Mio

美尾 樹





## Abstract

This thesis describes the newly developed synthetic strategy for an efficient synthesis of large phenine (benzene-1,3,5-triyl) nanocarbon molecules. Based on the strategy, two types of phenine nanocarbons were synthesized, and their characteristics including the structural features and dynamic behaviors were revealed by a combination of experimental and theoretical methods.

Chapter 1 describes the general introduction to the chemical synthesis of nanocarbon molecules. Methods to synthesize nanocarbon molecules and their limitations are discussed. Recently, the concept of phenine nanocarbons was introduced as a new approach for synthesizing large nanocarbon molecules. However, prior to this thesis, only two instances of phenine nanocarbons were known. To increase the structural diversity of phenine nanocarbons, a new synthetic strategy called the *polygon assembling strategy* was introduced.

Chapter 2 describes the synthesis and structures of a series of hoop-shaped phenine nanocarbon molecules. By assembling hexagonal parts, three congeners of the hoop comprising three to five hexagonal panels were synthesized. Their structures and flexibility were disclosed by spectroscopy, crystallography and theoretical calculations. In addition, host-guest interaction between one of the congeners and C<sub>70</sub> was revealed through Job plot and crystallographic analysis.

Chapter 3 describes the synthesis and dynamic behavior of a hemispherical phenine nanocarbon molecule. The molecule was synthesized by assembling six pentagonal parts of two different types. A combination of spectroscopy, crystallography and theoretical calculations revealed its rapid structural fluctuation, proving the flexibility of highly defective nanocarbon surfaces.

Chapter 4 describes a new method for structural analysis of phenine nanocarbon molecules. The method allows us to quantify the pyramidalization of a phenine unit and the inter-phenine torsion. It was then applied to known phenine nanocarbon molecules to illustrate their structural features.

Chapter 5 summarizes the present studies.

## Table of Contents

<b>Abstract.....</b>	<b>1</b>
<b>Chapter 1. General Introduction .....</b>	<b>5</b>
1.1 Curved nanocarbons .....	5
1.2 Curved nanocarbon molecules .....	8
1.2.1 Circulenes .....	8
1.2.2 Macrocyclic molecules .....	11
1.2.3 Flash vacuum pyrolysis .....	13
1.3 Phenine nanocarbon molecules .....	14
1.4 New strategies for larger and more diverse structures .....	15
1.5 References .....	17
<b>Chapter 2. Hoop-shaped Phenine Nanocarbons .....</b>	<b>19</b>
2.1 Introduction .....	19
2.2 Synthesis.....	20
2.3 Spectroscopic properties.....	20
2.4 Crystal structures .....	22
2.5 Fluctuation of structures.....	23
2.6 Porosity of crystals .....	24
2.7 Host–guest chemistry .....	25
2.8 Conclusion.....	27
2.9 Supplementary data .....	28
2.10 References .....	56
<b>Chapter 3. Hemispherical Phenine Nanocarbon.....</b>	<b>59</b>
3.1 Introduction .....	59
3.2 Synthesis.....	60
3.3 Spectroscopic properties.....	62
3.4 Crystal structures .....	63
3.5 Dynamic structure .....	64
3.6 Structural analyses.....	65
3.7 Host–guest interaction.....	66
3.8 Conclusion.....	69

3.9 Supplementary data .....	70
3.10 References .....	95
<b>Chapter 4. Quantitative Description of the Geometry of Phenine Nanocarbons..</b>	<b>98</b>
4.1 Introduction .....	98
4.2 Definition of the normal vector .....	99
4.3 Effectiveness of CPNV analysis for phenine nanocarbon structures .....	100
4.4 CPNV analysis of phenine nanocarbon molecules.....	101
4.5 Origin of the deformation of the hemispherical phenine nanocarbon molecule .....	102
4.6 Estimation of physical properties.....	105
4.7 Automation of CPNV analysis .....	106
4.8 Conclusion.....	107
4.9 Supplementary data .....	107
4.10 References .....	114
<b>Chapter 5. Summary.....</b>	<b>116</b>
<b>List of Publications.....</b>	<b>119</b>
<b>Acknowledgments .....</b>	<b>120</b>

## List of abbreviations

APCI	atmospheric pressure chemical ionization
APPI	atmospheric pressure photoionization
Bpin	pinacolatoboryl, 4,4,5,5-tetramethyl-1,3,2-dioxaborolan-2-yl
bpy	2,2'-bipyridine
<i>t</i> -Bu	<i>t</i> -butyl
cod	cycloocta-1,5-diene
CMP	cyclo- <i>meta</i> -phenylene
CNT	carbon nanotube
CPNV	curved normal phenine vector
CPP	cyclo- <i>para</i> -phenylene
DFT	density functional theory
DMF	<i>N,N</i> -dimethylformamide
DMSO	dimethyl sulfoxide
dppf	1,1'-bis(diphenylphosphino)ferrocene
dtbpy	4,4'-di- <i>tert</i> -butyl-2,2'-bipyridine
ESP	electrostatic potential
FVP	flash vacuum pyrolysis
GPC	gel permeation chromatography
GPF	geodesic phenine framework
HPLC	high-performance liquid chromatography
MALDI	matrix-assisted laser desorption ionization
MS	mass spectrum/spectrometry
NMR	nuclear magnetic resonance
NOESY	nuclear Overhauser effect spectroscopy
POAV	$\pi$ -orbital axis vector
rt	room temperature
THF	tetrahydrofuran
TMS	trimethylsilyl
TOF	time-of-flight
UV-vis	ultraviolet/visible light

## Chapter 1. General Introduction

### 1.1 Curved nanocarbons

Carbon is an element of indescribable importance, being the very foundation of our life itself. Besides our biological life, the element is also ubiquitous in our civilization with the entire field of organic chemistry dedicated to it. What makes carbon so special is its high ability to be catenated, that is, the ability to form chains or even networks of atoms, forming various allotropes and compounds with completely different characteristics.

Among such networked carbon allotropes, nanocarbons have been attracting increasing attention for their unique structures and physical properties since the discovery of buckminsterfullerene in 1985.<sup>1</sup> For example, carbon nanotubes (CNTs) have a tubular structure equivalent to a carbonaceous sheet rolled into a cylinder (Figure 1a). Stimulated by their discovery by Iijima in 1991 (Figure 1b),<sup>2</sup> extensive research on CNT was conducted by various groups to reveal their flexibility,<sup>3</sup> isomer dependence of conductivity, *etc.*<sup>4</sup> However, most of these studies depended on theoretical calculations and microscopy, and precise analyses such as titration have generally not been applied to nanocarbons (Figure 1c). This is largely because they are often mixtures of various isomers of different sizes rather than molecular entities with a single definite structure. Thus, to better understand the characteristics of nanocarbons, molecular models for them are highly called for, and various curved nanocarbon molecules have since been designed and synthesized as such (Figure 2). Although a few molecules which would later be called nanocarbons had been known before fullerenes and CNTs, larger and more diverse nanocarbon molecules started to appear one after another following their discovery. In this process, some different strategies were established to synthesize nanocarbon molecules, which will be detailed in the following section.

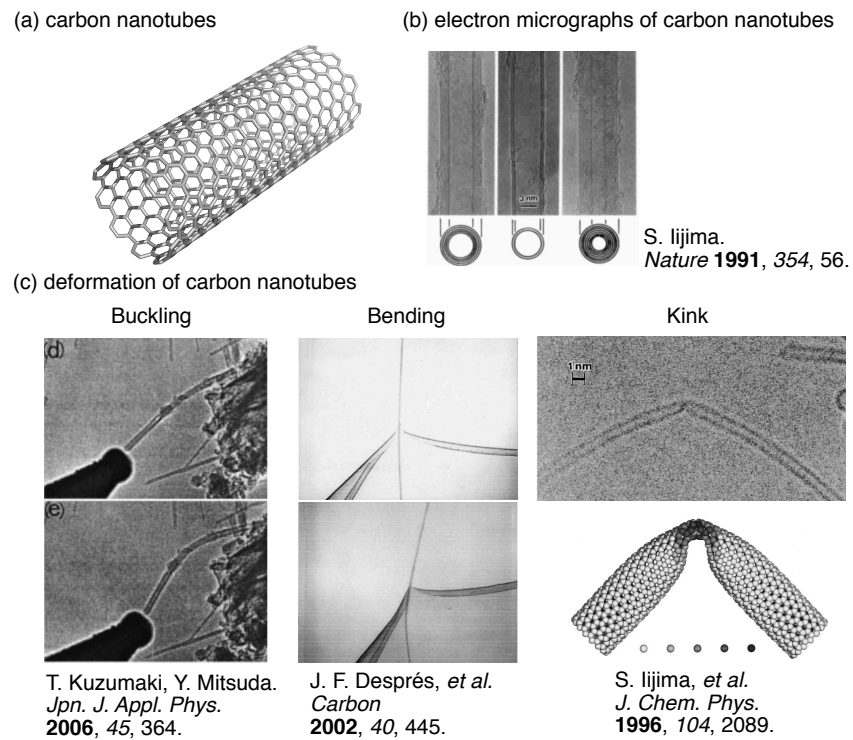


**Figure 1.** (a) Structure and (b) electron micrographs of carbon nanotubes. (c) Various studies on the mechanical characteristics of carbon nanotubes. Adapted from refs. 2, 5, 6 and 7 by permissions from Springer Nature, Copyright 1991; The Japan Society of Applied Physics, Copyright 2016; Elsevier, Copyright 2002; AIP Publishing, Copyright 1996.

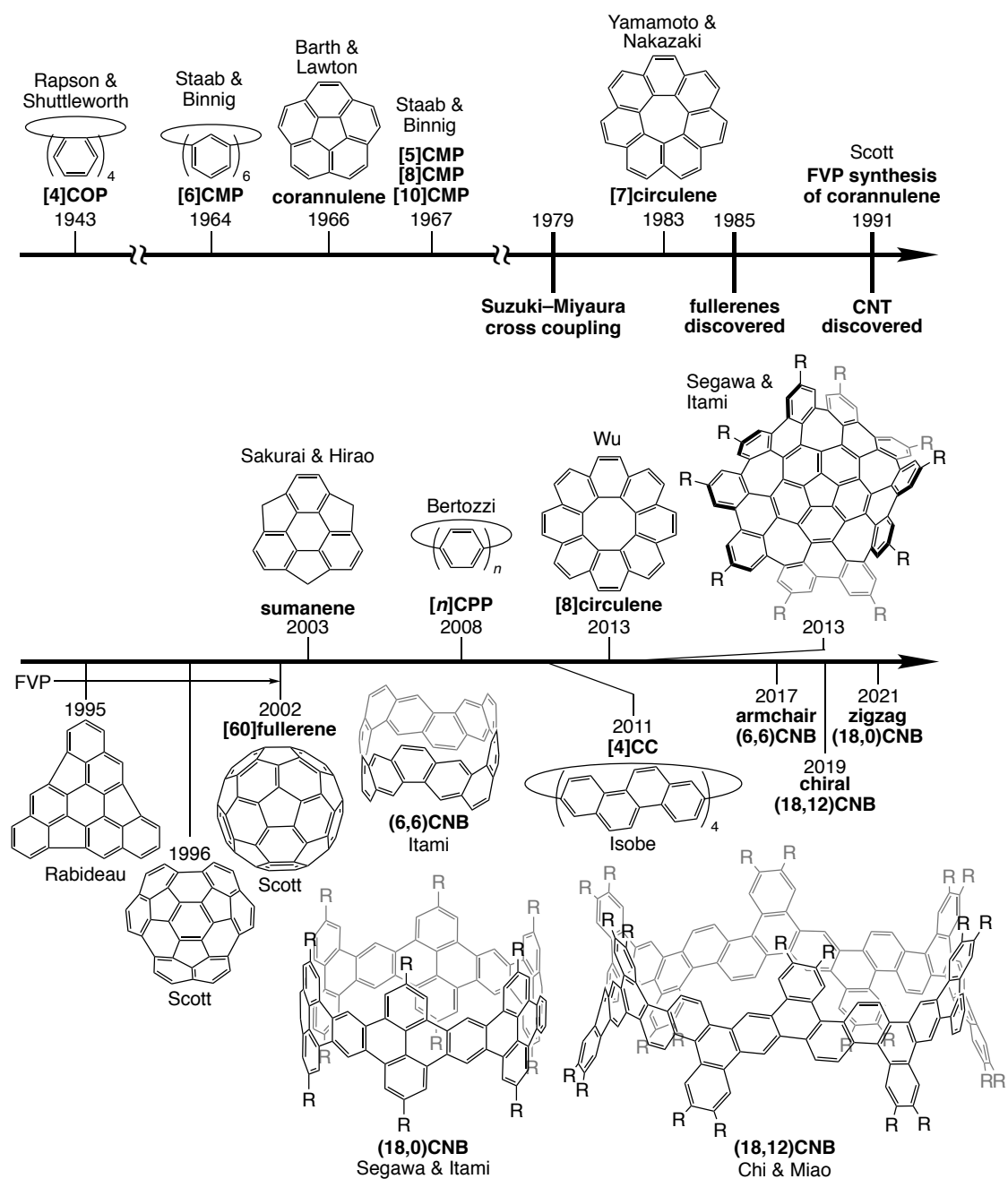


**Figure 2.** Timeline of chemically synthesized nanocarbon molecules.

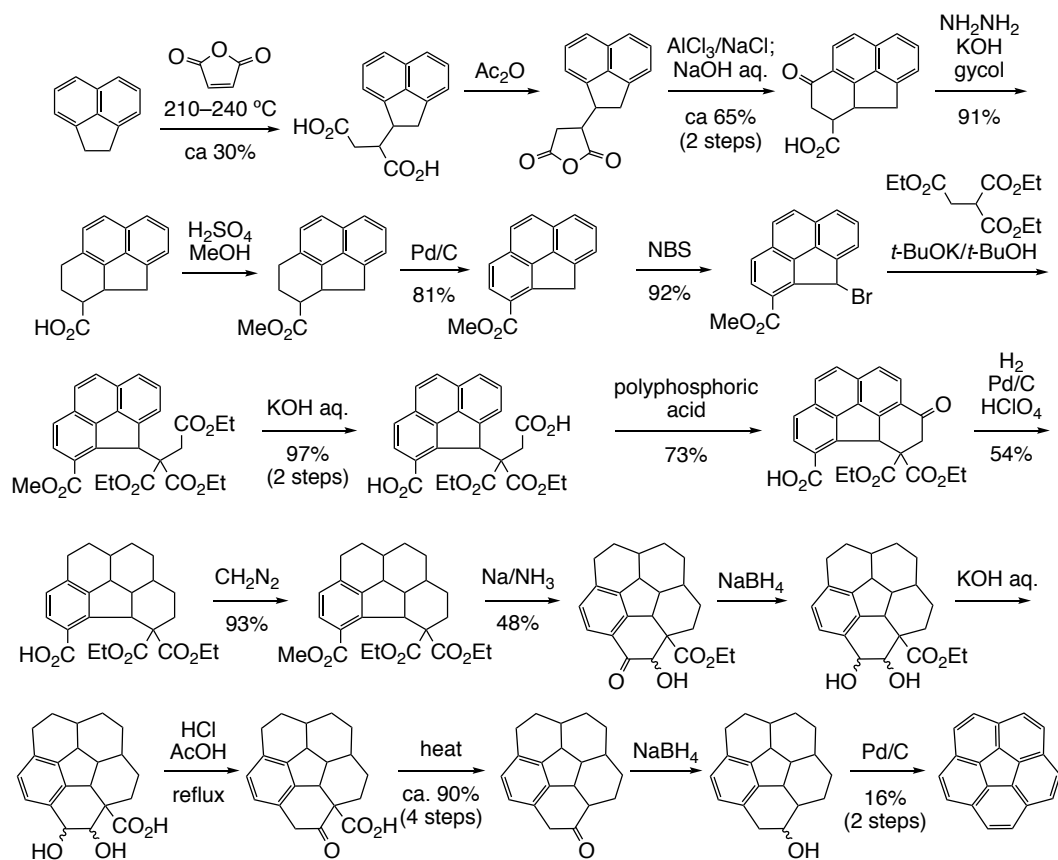
## 1.2 Curved nanocarbon molecules

Synthesis of curved nanocarbon molecules commonly faces an inherent difficulty of the target compound being "a chunk of carbon atoms" with no or very few functional groups. Thus, to synthesize a nanocarbon molecule, one must employ a carefully designed synthetic route, or an established strategy which is applicable for some classes of nanocarbon molecules. In subsection 1.2.1, the former approach will be detailed by taking circulenes as examples. In subsections 1.2.2 and 3, the latter approach will be explained.

### 1.2.1 Circulenes

As models of such curved nanocarbons,  $[n]$ circulenes are featured with the simplest curved structures, which consist of a central  $n$ -membered ring surrounded with fused benzene rings.<sup>8</sup>  $[n]$ Circulenes are positively curved like a bowl for  $n = 4$  and 5, or negatively curved like a saddle for  $n = 7$  and 8. Among them,  $[5]$ circulene, or corannulene (**1**) appeared as the first class of compound that was synthesized in 1966 (Scheme 1; see Figure 4a).<sup>9</sup> This precedes the discovery of fullerenes and CNTs by decades, but the molecule started to attract renewed attention as a partial model for  $[60]$ fullerene.<sup>10</sup> The original synthetic route by Barth and Lawton<sup>9</sup> comprises as many as 19 steps from 1,2-dihydroacenaphthylene with an overall yield of 0.33%. It works by forming a fused six-membered rings around the central five-membered ring present from the beginning. The skeleton of the target molecule is completed in 13 steps, which are then followed by six more steps to remove unnecessary functional groups and to aromatize the molecule. Since then, efforts to prepare corannulene more efficiently has been continued, and in 2012, Siegel and co-workers reported a nine-step synthesis with a remarkable overall yield of 8.7%, enabling kilogram-scale preparation (see Figure 4b).<sup>11</sup> In both synthetic routes, most of the individual steps are classical reactions such as Friedel–Crafts acylation/alkylation, aldol condensation and Diels–Alder reaction, except for Siegel's fourth step, where Girard's reagent is used for chromatography-free removal of the undesirable isomer. The fact that it took nearly half a century for a scalable synthesis to be developed illustrates the inherent difficulty of chemical preparation of nanocarbon molecules in solution, even for small and basic ones like corannulene.





**Scheme 1.** Summarized synthetic procedures of circulenes.

Nevertheless, having the real substance in hand provides a great opportunity to reveal the detailed properties. In 1976, Hanson and Nordman reported the crystal structure of corannulene, revealing the expected but then-unverified bowl-like geometry (Figure 3a).<sup>12</sup> In 1991, Scott *et al.* synthesized a corannulene derivative with a 2-hydroxypropan-2-yl substituent on the edge and proved the presence of bowl-to-bowl inversion (Figure 3b).<sup>13</sup> By observing the coalescence of  $^1\text{H}$  NMR resonances of the desymmetrized corannulene, they experimentally determined the inversion barrier  $\Delta G^\ddagger$  of  $10.2 \pm 0.2$  kcal/mol (209 K). Without a precisely synthesized model molecule like corannulene, it would have been impossible to reveal the behavior of nanocarbons in such detail.

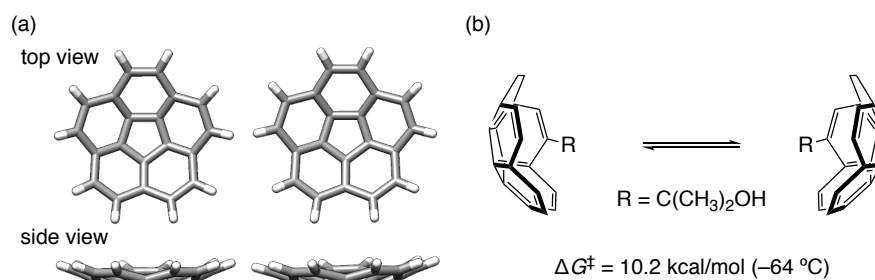


**Figure 3.** Experimentally revealed properties of corannulene: (a) crystal structures and (b) thermodynamics of bowl-to-bowl inversion.

[7]Circulene is another example of molecular nanocarbons known before CNT. Just as corannulene is a model for bowl-shaped defect in a graphene sheet, [7]circulene serves as one for a saddle-shaped sheet, and it was first synthesized in 1983 by Yamamoto *et al*<sup>14</sup> as a next higher circulene after [5]- and [6]circulene. The synthesis was performed in 13 steps with an overall yield of 0.27%. The authors were also successful in obtaining a single crystal, which precisely revealed the saddle-shaped surface of graphene sheet induced by the heptagon at the center. After this work, uniqueness of curved geometry of carbonaceous sheets was recognized by the advent of fullerenes and CNTs, which further gives rise of [4]circulene<sup>15</sup> and [8]circulene<sup>16</sup> in 2010. The synthetic strategies of [n]circulenes are summarized in Figure 4. For the construction of the curved structures of [n]circulenes, each target requires an elaborate synthetic route to be devised. Although these studies on the structures of [n]circulenes indeed provided the most fundamental knowledge of curved nanocarbons, the difficulty of synthesis poses a limitation for achievable structures, hampering investigation of larger or more complex nanocarbon molecules.

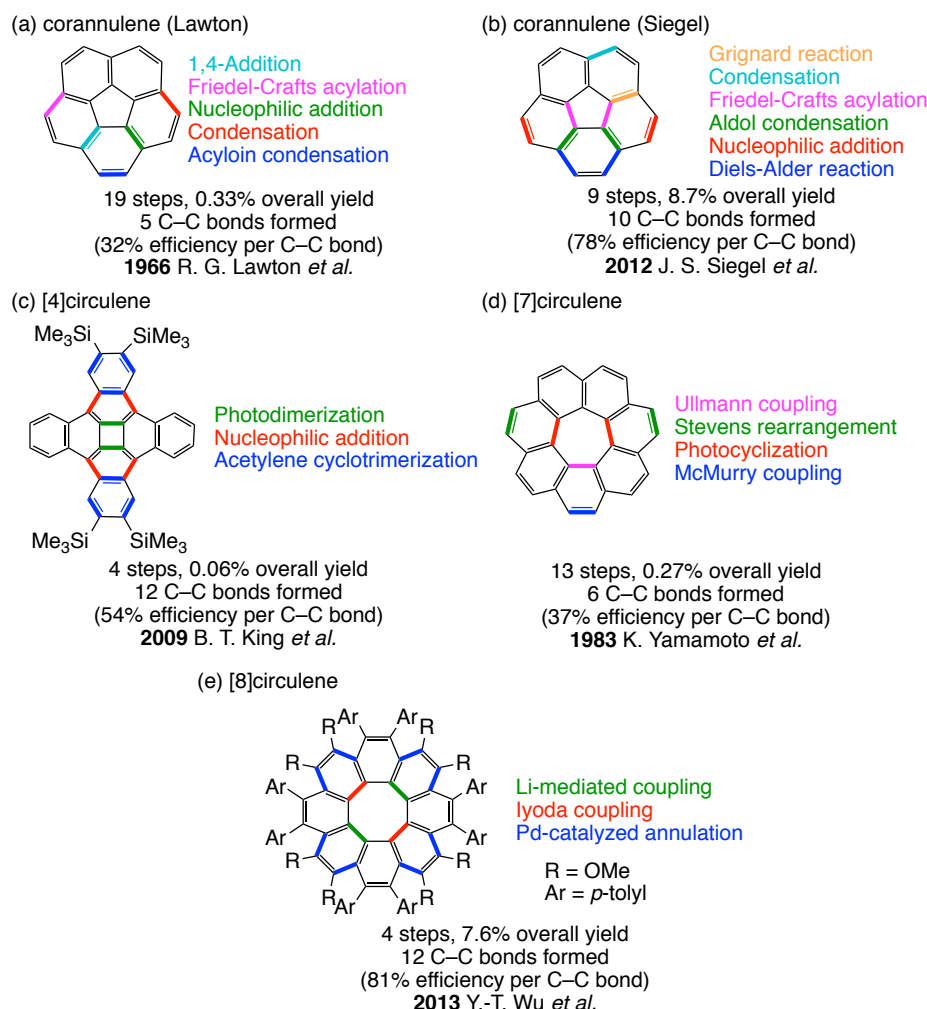


**Figure 4.** Summarized synthetic procedures of circulenes.

### 1.2.2 Macrocyclic molecules

As an alternative approach towards curved nanocarbon molecules, macrocyclization of relatively simple aromatic units has been also employed (Figure 5). Among the simplest and earliest examples are [*n*]cyclo-*ortho*-phenylenes, *n* benzene rings circularly linked by the *ortho*-position, which was first reported by Rapson in 1943<sup>17</sup> for *n* = 4, again long before the advent of CNTs. This approach is quite productive, because a variety of structures can be designed and synthesized by macrocyclizing different arenes. The macrocyclic structure can force arylene panels, otherwise planar, to adopt a curved shape, making them a model for nanotubes or defective surfaces, depending on the design. The introduction of curvature, however, is also a synthetic challenge, and has been overcome by some methods. For example, a two-step approach

consisting of 1) strain-free linking of aryl panels with angled corner units and 2) straightening the corner units is very common, where the corner units can be *cis*-1,4-dimethoxy-2,5-cyclohexadiene-1,4-diyl,<sup>18</sup> *cis*-1,4-dihydroxy-cyclohexane-1,4-diyl<sup>19</sup> (aromatized into *p*-phenylene, Figure 5a) or a square planar Pt center<sup>20</sup> (removed by reductive elimination, Figure 5b), *etc.* The latter approach is essentially a coupling reaction, and in addition to commonly employed, sophisticated coupling reactions, such as Suzuki–Miyaura cross coupling, less common metal centers are used. They are sometimes more suitable for macrocyclization owing to their superior capability to form metallacycle intermediates.

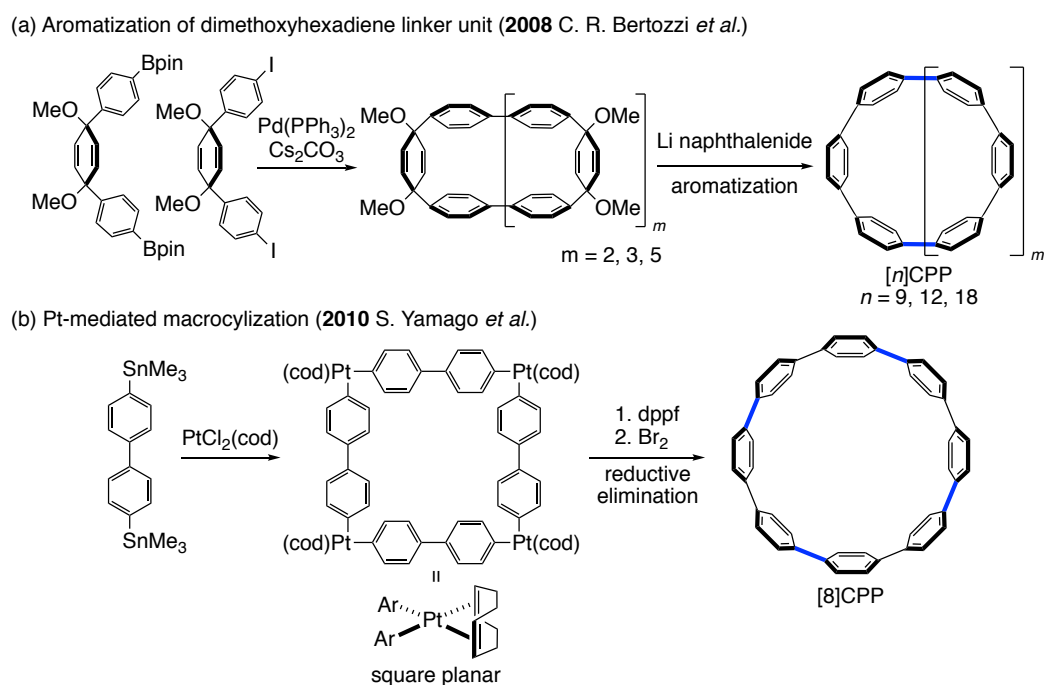


**Figure 5.** Synthesis of  $[n]$ CPP.

Coupling reactions can play an essential role in synthesizing nanocarbon molecules of this class since the units to be linked are already aromatic. Many of the important coupling reactions require the carbon atoms involved to be  $sp^2$ -hybridized. For cycloarylene molecules, the condition is automatically met, which is often not the case for other nanocarbon molecules. Thus, despite the development of efficient coupling reactions, their applicability is limited in the field of chemical synthesis of nanocarbon molecules.

Some of the molecules of this class have also been playing an important role as very

short, or minimal, model molecules of CNTs. For example, [4]cyclo-2,8-chrysenylene ([4]CC) by Isobe group, was synthesized in 2011 by connecting four chrysene panels by Pt-mediated reaction.<sup>21</sup> The belt-like geometry was persistent at room temperature, which allowed the authors to separate six stereoisomers (including two enantiomeric pairs and two meso isomers). The chiral [4]CC isomers were later employed to exhibit asymmetric catalytic activity<sup>22</sup> and self-sorting behavior<sup>23</sup>, providing an important insight into the chemistry of chiral nanocarbons.

### 1.2.3 Flash vacuum pyrolysis

Aside from the conventional solution chemistry, flash vacuum pyrolysis (FVP) serves as an alternative for the synthesis of curved nanocarbon molecules.<sup>24</sup> In 1991, Scott *et al.* reported yet another synthetic method for corannulene ending with an FVP reaction where 7,10-diethynylfluoranthene was passed through a 1000 °C oven to result in the formation of two 6-membered rings.<sup>25</sup> Since this discovery, FVP has been extensively used in the synthesis of curved nanocarbon molecules, especially those which are a fragment of buckminsterfullerene (Figure 6a & b). In fact, the development of FVP techniques went as far as achieving the first chemical synthesis of buckminsterfullerene itself in 2002 (Figure 6c).<sup>26</sup> Although FVP's ability to assemble a net of polyhedrons into curved nanocarbon molecules is obvious, it is not a silver bullet; the difficulty of synthesizing net-like precursors persists, and not every precursor can survive FVP's harsh conditions.<sup>27</sup>

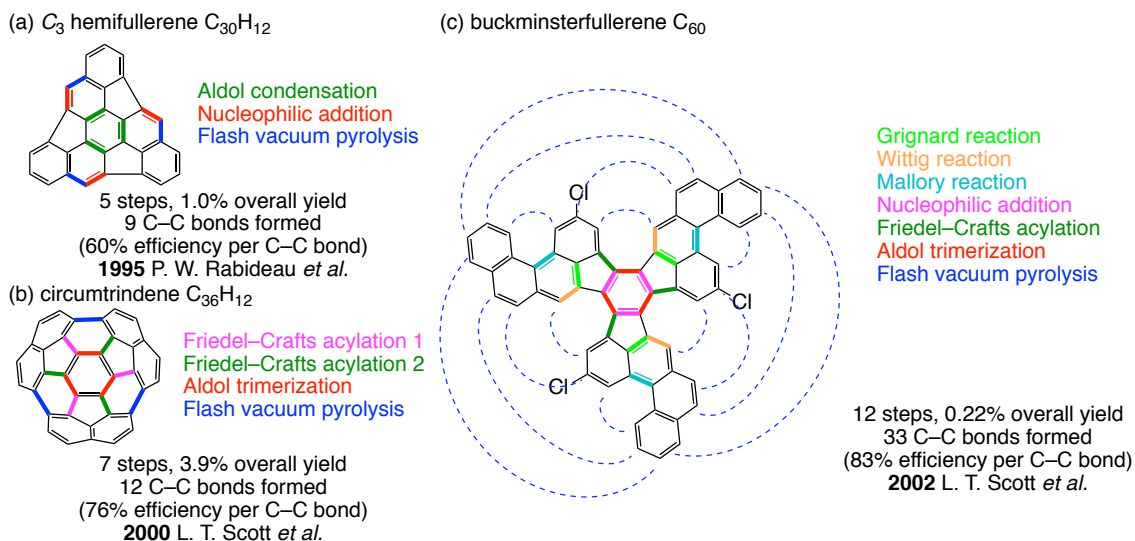


**Figure 6.** Synthesis of nanocarbon molecules by flash vacuum pyrolysis.

### 1.3 Phenine nanocarbon molecules

As discussed in the previous section, conventional methods to synthesize nanocarbon molecules are not readily applicable to larger molecules. As a possible answer to this challenge, Ikemoto *et al.* established a new concept for designing and synthesizing large nanocarbon molecules (coined geodesic phenine frameworks (GPFs)) in 2017.<sup>28</sup> In the concept, the unit of the molecule is benzene-1,3,5-triyl (called *phenine*) rather than  $sp^2$ -carbon (Figure 7a). Since they share the same trigonal planar geometry, a similar network can be formed with phenine units and with  $sp^2$ -carbon atoms. Thus, one can design a magnified version of known/proposed nanocarbon molecules by replacing  $sp^2$ -carbon atoms with phenine units. Noteworthy is that a network of phenine units becomes a highly defective network of  $sp^2$ -carbons to produce nanocarbon molecules with periodic defects.

The fact that all the carbon atoms in a phenine unit is  $sp^2$ -hybridized is also very convenient in synthesis since we can make full use of highly efficient and robust coupling reactions. Despite the potential as a powerful designing principle, only two GPFs, each being a phenine analogue to corannulene and [7]circulene, were known before starting my Ph.D. thesis work.<sup>28,29</sup> In addition, the same synthetic strategy was used for both: a terphenyl unit was attached to the pentagonal/heptagonal omphalos unit and then the terphenyl units were connected with each other to form the outer rings (Figure 7b). With

this strategy, only magnified circulene structures are accessible, and different strategies to achieve more structural diversity are highly sought after.

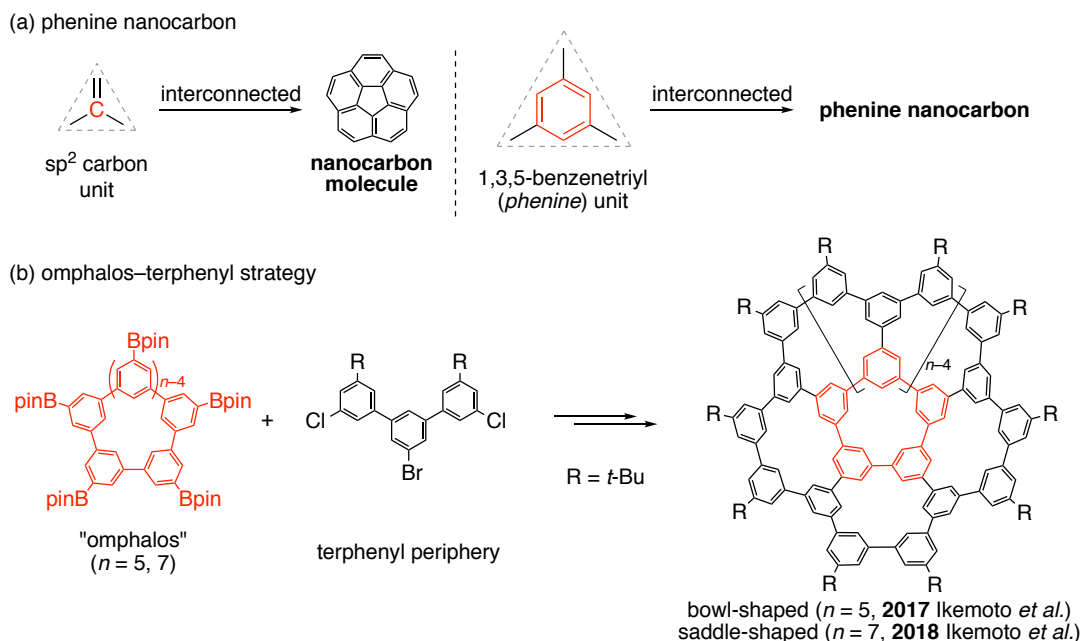


**Figure 7.** (a) Concept of phenine nanocarbons. (b) Synthesis by the omphalos–terphenyl strategy of circulene-based phenine nanocarbons.

#### 1.4 New strategies for larger and more diverse structures

In this work, I developed a new synthetic strategy, a polygon assembling strategy, for phenine nanocarbons (Note: In this thesis, I opt for the more general term *phenine nanocarbon* instead of *geodesic phenine framework* because the target was no longer analogs of geodesic polyarenes having non-hexagons). In this strategy, the target molecule is divided into polygonal parts with a skeleton of  $[n]$ cyclo-*meta*-phenylene ( $[n]$ CMP), and these parts are first formed to be assembled in the later stage of synthesis (Figure 8). Synthesis based on this strategy is expected to be more efficient because 1) the route will be convergent and 2) we can avoid performing multiple strain-inducing macrocyclization reactions in late stages. In this thesis, I synthesized two different classes of phenine nanocarbons by the strategy, and the details of their synthesis and structural characteristics are discussed in the following chapters.

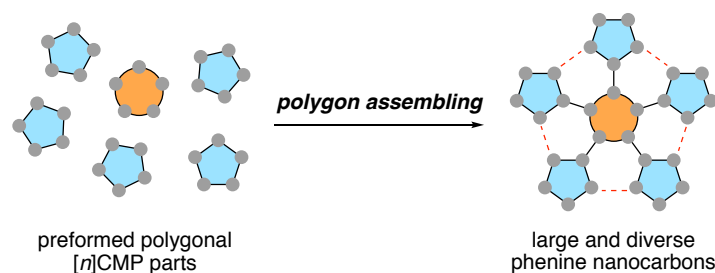


**Figure 8.** Schematic depiction of the polygon assembling strategy.

In **Chapter 2**, a series of hoop-shaped phenine nanocarbons is discussed. The molecules were synthesized by assembling three to five hexagonal [6]CMP units into macrocycles isorecticular to  $[n]$ cyclo-*para*-phenylenes ( $[n]$ CPPs). The combination of experimental and computational analyses revealed the panel number-dependence of their flexibility. The host–guest interaction between one of the hoops and  $C_{70}$  was also analyzed by titration experiments and single-crystal X-ray diffraction.

In **Chapter 3**, a hemispherical molecule composed of 30 phenine units is discussed. The molecular design is based on a bisection of  $C_{60}$ , and the hemispherical molecule was synthesized by assembling six pentagonal [5]CMP units of two different types. The interesting dynamic structure of the hemisphere was revealed through a detailed analyses by spectroscopic, crystallographic and computational methods.

In **Chapter 4**, a method to describe the geometry of phenine nanocarbons is discussed. The method was developed with a focus on the phenine units rather than carbon atoms to allow for the comparison of phenine nanocarbons with geometrically similar nanocarbon molecules. The structure of the hemispherical molecule introduced in Chapter 3 was further discussed with the new method to reveal the origin of its peculiar dynamic structure, along with other phenine nanocarbons known.

Finally, in **Chapter 5**, the summary and perspective of this work are discussed.



## 1.5 References

1. H. W. Kroto, J. R. Heath, S. C. O'Brien, R. F. Curl, R. E. Smalley, *Nature* **1985**, 318, 162-163.
2. S. Iijima, *Nature* **1991**, 354, 56-58.
3. (a) T. Koyama, T. Tsuji, K. Yoshida, H. Takano, Y. Tsusaka, Y. Kagoshima, *Jpn. J. Appl. Phys.* **2006**, 45, L1159-L1161. (b) J. F. Després, E. Daguerre, K. Lafdi, *Carbon* **2002**, 40, 460-462. (c) S. Iijima, C. Brabec, A. Maiti, J. Bernholc, *J. Chem. Phys.* **1996**, 104, 2089-2092.
4. N. Hamada, S. Sawada, A. Oshiyama, *Phys. Rev. Lett.* **1992**, 68, 1579-1581.
5. T. Kuzumaki, Y. Mitsuda, *Jpn. J. Appl. Phys.* **2006**, 45, 364-368.
6. J. F. Després, E. Daguerre, K. Lafdi, *Carbon*, **2002**, 40, 445-462.
7. S. Iijima, C. Brabec, A. Maiti, J. Bernholc, *J. Chem. Phys.* **1996**, 104, 2089-2092.
8. J. H. Dopper, H. Wynberg, *Tetrahedron Lett.* **1972**, 9, 763-766.
9. (a) W. E. Barth, R. G. Lawton, *J. Am. Chem. Soc.* **1966**, 88, 380-381. (b) L. T. Scott, M. M. Hashemi, D. T. Meyer, H. B. Warren, *J. Am. Chem. Soc.* **1991**, 113, 7082-7084.
10. E. Osawa, *Kagaku* **1970**, 25, 854.
11. A. M. Butterfield, B. Gilomen, J. S. Siegel, *Org. Process Res. Dev.* **2012**, 16, 664-676.
12. J. C. Hanson, C. E. Nordman, *Acta Crystallogr. B* **1976**, 32, 1147-1153.
13. L. T. Scott, M. M. Hashemi, M. T. Bratcher, *J. Am. Chem. Soc.* **1992**, 114, 1920-1921.
14. (a) K. Yamamoto, T. Harada, M. Nakazaki, T. Naka, Y. Kai, S. Harada, N. Kasai, *J. Am. Chem. Soc.* **1983**, 105, 7171-7172. (b) K. Yamamoto, T. Harada, Y. Okamoto, H. Chikamatsu, M. Nakazaki, Y. Kai, T. Nakao, M. Tanaka, S. Harada, N. Kasai, *J. Am. Chem. Soc.* **1988**, 110, 3578-3584.
15. R. B. Bharat, T. Bally, A. Valente, M. K. Cyrański, Ł. Dobrzycki, S. M. Spain, P. Rempała, M. R. Chin, B. T. King, *Angew. Chem. Int. Ed.* **2010**, 49, 399-402.
16. (a) C.-N. Feng, M.-Y. Kuo, Y.-T. Wu, *Angew. Chem. Int. Ed.* **2013**, 52, 7791-7794. (b) Y. Sakamoto, T. Suzuki, *J. Am. Chem. Soc.* **2013**, 135, 14074-14077.
17. W. S. Rapon, R. G. Shuttleworth, J. N. van Niekerk, *J. Chem. Soc.* **1943**, 326-327.
18. R. Jasti, J. Bhattacharjee, J. B. Neaton, C. R. Bertozzi, *J. Am. Chem. Soc.* **2008**, 130, 17646-17647.
19. H. Takaba, H. Omachi, Y. Yamamoto, J. Bouffard, K. Itami, *Angew. Chem. Int. Ed.*

- 2009**, *48*, 6112-6116.
20. S. Yamago, Y. Watanabe, T. Iwamoto, *Angew. Chem. Int. Ed.* **2010**, *49*, 757-759.
21. S. Hitosugi, W. Nakanishi, T. Yamasaki, H. Isobe, *Nat. Commun.* **2011**, *2*, 492.
22. S. Hitosugi, A. Matsumoto, Y. Kaimori, R. Iizuka, K. Soai, H. Isobe, *Org. Lett.* **2014**, *16*, 645-647.
23. T. Matsuno, S. Sato, A. Yokoyama, S. Kamata, H. Isobe, *Angew. Chem. Int. Ed.* **2016**, *55*, 15339-15343.
24. R. F. C. Brown, *Pure Appl. Chem.* **1990**, *62*, 1981-1986.
25. L. T. Scott, M. M. Hashemi, D. T. Meyer, H. B. Warren, *J. Am. Chem. Soc.* **1991**, *113*, 7082-7084.
26. L. T. Scott, M. H. Boorum, B. J. McMahon, S. Hagen, J. Mack, J. Blank, H. Wegner, A. De Meijere, *Science* **2002**, *295*, 1500-1503.
27. (a) V. M. Tsefrikas, L. T. Scott, *Chem. Rev.* **2006**, *106*, 4868-4884. (b) L. T. Scott, *Angew. Chem. Int. Ed.* **2004**, *43*, 4994-5007
28. K. Ikemoto, R. Kobayashi, S. Sato, H. Isobe, *Angew. Chem. Int. Ed.* **2017**, *56*, 6511-6514.
29. K. Ikemoto, J. Lin, R. Kobayashi, S. Sato, H. Isobe, *Angew. Chem. Int. Ed.* **2018**, *57*, 8555-8559.

## Chapter 2. Hoop-shaped Phenine Nanocarbons

### 2.1 Introduction

As mentioned in the previous chapter, hoop-shaped molecules formed by circularly linking arylene panels predate the discovery of CNTs. However, it was not until 2008 that the long-sought  $[n]$ cyclo-*para*-phenylenes ( $[n]$ CPPs) were synthesized by Jasti *et al.* despite the simple structures.<sup>1</sup> Following the success of Jasti *et al.* with  $[9]$ -,  $[12]$ - and  $[18]$ CPP, active efforts to synthesize other congeners, smaller ones especially, continued,<sup>2,3</sup> and  $[5]$ CPP was finally synthesized in 2014 by Jasti's group.<sup>4</sup> As the name suggests,  $[n]$ CPP is a macrocycle of  $n$  phenylene panels linked by the para-position, and as a model of CNTs,  $[n]$ CPP represents an armchair-type nanotube denoted by chiral indices  $(n, n)$ .<sup>5</sup>

By applying the phenine nanocarbon concept to  $[n]$ CPP, we can design hoop-shaped phenine nanocarbons with  $n$  circularly-linked  $[6]$ cyclo-*meta*-phenylene ( $[6]$ CMP) panels (Figure 1). This molecule, hereafter called **hoop  $\Phi_{6n}$**  with  $\Phi$  representing "phenine" and  $6n$  the total number of phenine units, can be synthesized by the polygon assembling strategy by dividing it into hexagonal parts with a  $[6]$ CMP skeleton. In addition, **hoop  $\Phi_{6n}$**  itself can be considered a defective armchair-type CNT with chiral index of  $(3n, 3n)$ , making it an interesting subject of structural studies on defective nanotubes. Thus, I synthesized **hoop  $\Phi_{6n}$**  with  $n = 3-5$  by the polygon assembling strategy, and revealed their structural features by spectroscopy, crystallography and theoretical calculations. Furthermore, the unique host-guest interaction of **hoop  $\Phi_{6n}$**  with the  $C_{70}$  guest enabled by its flexibility will be discussed in this chapter.

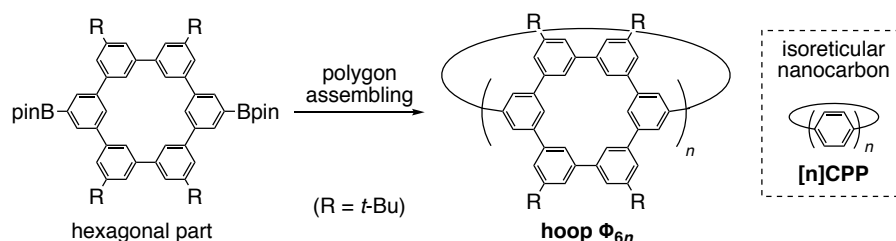
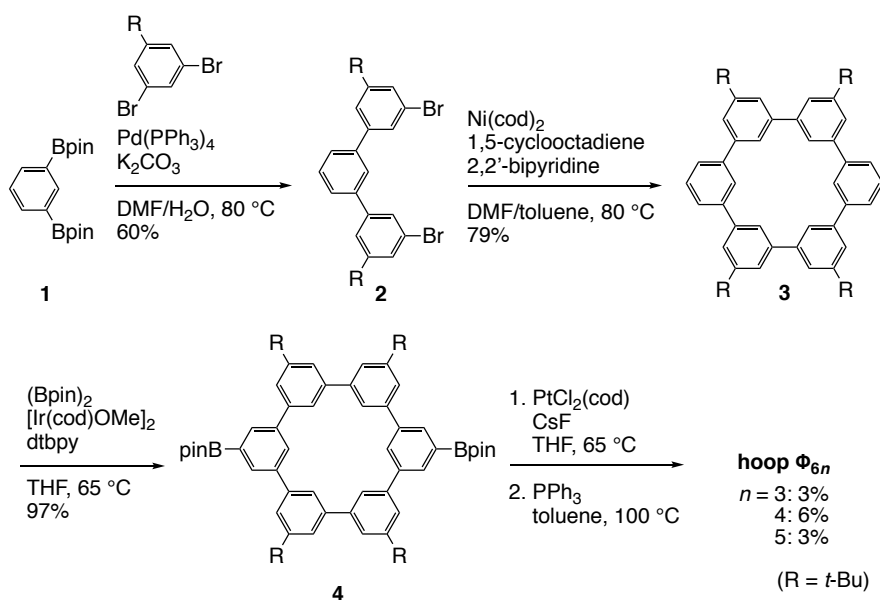


**Figure 1.** Polygon assembling strategy applied to hoop-shaped phenine nanocarbon isorecticular to  $[n]$ CPP.

## 2.2 Synthesis

To study the fundamental structures, we synthesized a series of **hoop**  $\Phi_{6n}$  molecules as hydrocarbons devoid of heteroatoms via a synthetic route established for the pNT molecules.<sup>6,7</sup> Thus, terphenyl **2** with *t*-Bu end groups was synthesized by Suzuki coupling,<sup>8</sup> and a subsequent [3+3] cyclization with Yamamoto-type coupling afforded [6]cyclo-*meta*-phenylene ([6]CMP) precursor **3** (Scheme 1).<sup>6,9</sup> An Ir-catalyzed C-H borylation of **3** proceeded in a site selective manner to furnish [6]CMP with boryl handles at the "*para*" positions.<sup>10</sup> Finally, the Pt-mediated macrocyclization with **4** was performed to afford three **hoop**  $\Phi_{6n}$  molecules that possessed different numbers of the [6]CMP panels. Thus, unlike the macrocyclization for the small CPP molecules,<sup>3</sup> the Pt-mediated macrocyclization proceeded with multiple [6]CMP panels for the nanometer-sized congeners of **hoop**  $\Phi_{6n}$  in a non-selective manner with  $n = 3, 4$  and  $5$ .<sup>6,11</sup> The small congeners with panel numbers of 3 and 4 have not been synthesized with phenylene [*n*]CPP structures.<sup>12</sup> Although we do not understand the reason, the replacement of trimethylsilyl (TMS) groups on [6]CMP panels with *t*-Bu groups affected the yields and the product distributions.<sup>6</sup> Synthetically, the TMS/*t*-Bu replacement is the key design for lengthening of cylinders.



**Scheme 1.** Synthesis of the hoop-shaped phenine nanocarbons.

## 2.3 Spectroscopic properties

Spectroscopic analyses of the **hoop**  $\Phi_{6n}$  molecules were carried out. MALDI mass

spectrometry confirmed the enormous molecular weights of 2037, 2716 and 3394 ( $m/z$  values of  $[M]^+$ ) for  $n = 3$  ( $C_{156}H_{162}$  with 108  $sp^2$ -carbon atoms), 4 ( $C_{208}H_{216}$  with 144  $sp^2$ -carbon atoms) and 5 ( $C_{260}H_{270}$  with 180  $sp^2$ -carbon atoms), respectively (Figure 2a). Photophysical properties were investigated by UV-vis absorption and fluorescence spectroscopy. As shown in Figure 2b, intense absorption peaks were observed at approximately 250 nm, commonly, for **hoop**  $\Phi_{6n}$  with  $n = 3, 4$  and 5, and fluorescence peaks were likewise observed at approximately 360 nm. Independence of the absorption peaks from the panel numbers was similarly observed with  $[n]$ CPP.<sup>13</sup> A small yet evident difference in the absorption spectra was noted with **hoop**  $\Phi_{18}$  as a broad shoulder at approximately 300 nm. Such redshifts are most likely due to rigid belt shapes that effectively extend the  $\pi$ -conjugations.<sup>11,12,14</sup> We did not observe dependency of the fluorescence peaks on the panel numbers, which was different from previous observations with small isorecticular  $[n]$ CPPs. Photochemical properties of  $[n]$ CPP molecules are currently under intense investigation,<sup>15</sup> and the present observations provide another experimental basis for further in-depth theoretical studies.

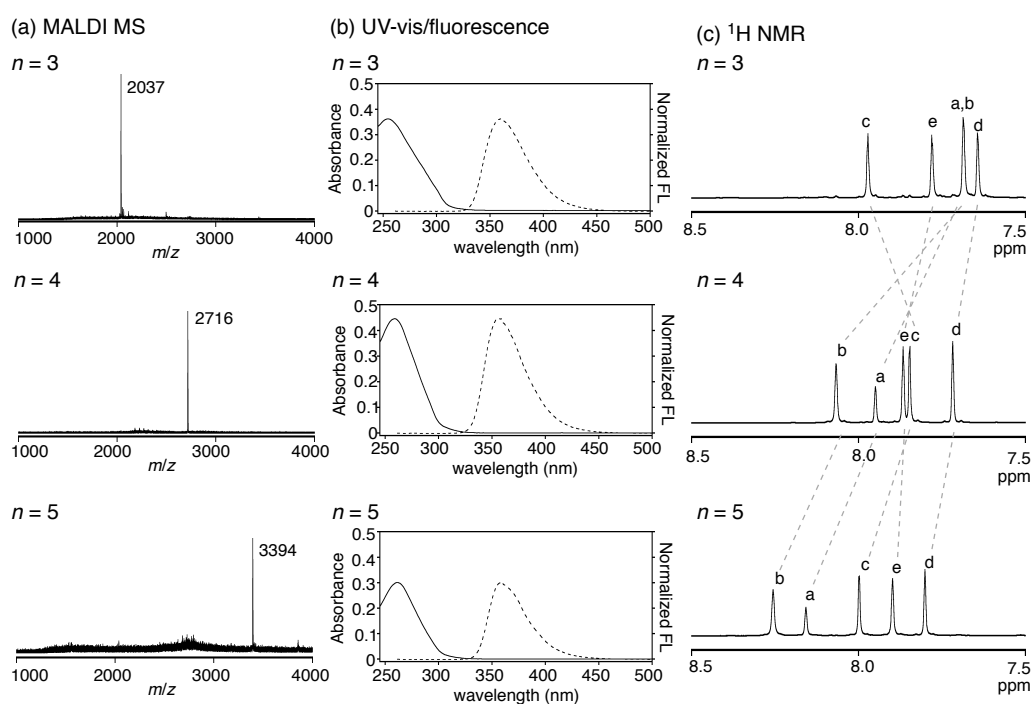


**Figure 2.** Representative spectra of hoop-shaped phenine nanocarbons. (a) MALDI mass spectra (positive). Matrix = pyrene. (b) UV-vis/fluorescence spectra in  $CHCl_3$ . Concentrations:  $1.37 \times 10^{-6}$  M ( $n = 3$ ),  $1.03 \times 10^{-6}$  M ( $n = 4$ ) and  $5.94 \times 10^{-7}$  M ( $n = 5$ ). Excitation for fluorescence = 254 nm. (c) Aromatic regions of proton NMR spectra in

CDCl<sub>3</sub>.

Aromatic regions of <sup>1</sup>H NMR spectra (CDCl<sub>3</sub>) are shown in Figure 2c. The number of aromatic protons in **hoop**  $\Phi_{6n}$  are 54 ( $n = 3$ ), 72 ( $n = 4$ ) and 90 ( $n = 5$ ). These multiple aromatic protons of **hoop**  $\Phi_{6n}$  converged into four ( $n = 3$ ) and five ( $n = 4$  and 5) resonances in <sup>1</sup>H NMR spectra and were fully assigned with the aid of NOESY spectra (see supplementary data). The number of resonances was consistent with the highest reachable point symmetry of  $D_{nh}$  ( $n = 3-5$ ), and the  $D_{nh}$  cylindrical shapes of molecules were spectroscopically indicated as time-average structures. However, the presence and validity of the symmetric structures in solution should be carefully examined (see below).<sup>16,17</sup> Although most of the resonances shifted towards downfield regions upon increasing the numbers of panels (except proton "c"),<sup>18</sup> we do not think that this tendency can be ascribed to a single origin, as mentioned in the discussion of crystal structures and theoretical dynamic structures (see below).

## 2.4 Crystal structures

Molecular structures of the **hoop**  $\Phi_{6n}$  congeners were fully revealed by X-ray crystallographic analysis of single crystals. As shown in Figure 3, **hoop**  $\Phi_{6n}$  molecules commonly exhibited nanometer-sized pores at the center of macrocyclic structures. Overall shapes deviated from the expected cylindrical shapes, and the structural deviations were dependent on the panel numbers. Severe deformations were particularly apparent with larger **hoops**  $\Phi_{24}$  and  $\Phi_{30}$  molecules, and the deviations from cylinders were quantified in terms of dihedral angles. The dihedral angles of the three biaryl linkages (c-c, a-b and b-b) were thus measured (Figure 3d), revealing that the smallest structural deviation was exhibited by the **hoop**  $\Phi_{18}$  molecule. As was observed with pNT molecules with a cylindrical shape,<sup>6</sup> the dihedral angles were small at the circumference for the **hoop**  $\Phi_{18}$  molecule, and the smallest coplanar value of  $0.8 \pm 0.7^\circ$  was recorded at the biaryl bonds connecting the [6]CMP panel (c-c). The standard deviations of the dihedral angles were also small for the **hoop**  $\Phi_{18}$  molecule. These observations indicated persistency of the molecular structure as well as the cylindrical shape (see below). The larger congeners possessed large dihedral angles and deviated from a cylindrical shape. Except for the c-c dihedral angles of **hoop**  $\Phi_{24}$ , the standard deviations were also considerably large. These observations indicated fluctuating structures of larger

congeners, which was consistent with the theoretical pictures (see below).

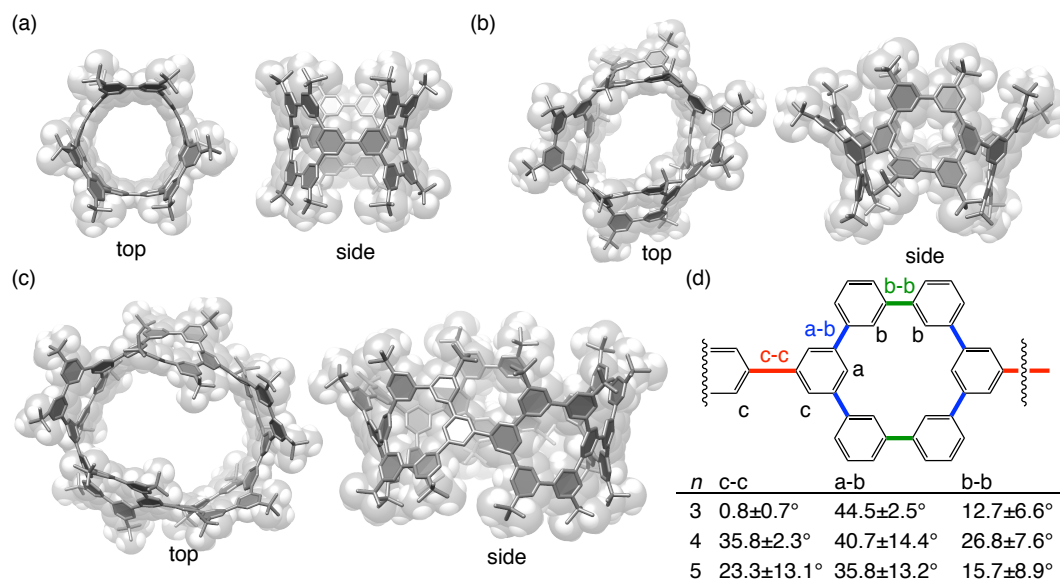


**Figure 3.** Crystal structures of the hoop-shaped phenine nanocarbon molecules.

## 2.5 Fluctuation of structures

To elucidate intrinsic structural fluctuations of the phenine frameworks, we performed conformation search calculations of **hoop**  $\Phi_{6n}(\text{H})$  congeners lacking *t*-Bu groups. Thus, MMFF94 force field calculations<sup>19</sup> with a low-mode sampling sequence<sup>20</sup> exploiting 2000 structures were performed to afford the  $\leq 5$ -kcal/mol conformers shown in Figure 4. As was indicated by the crystal structure, the smallest **hoop**  $\Phi_{18}(\text{H})$  did not show conformational flexibility with small structural deviations from the global minimum. The structure of the global minimum was similar to the crystal structure possessing the cylinder-like shape. This result was consistent with the solution-phase UV-vis spectrum showing redshifted shoulders that indicated  $\pi$ -extension over the rigid structure.<sup>11,17,21</sup> In contrast, the largest congener, **hoop**  $\Phi_{30}(\text{H})$ , showed a diverse range of conformations, suggesting a flexible molecular structure. In addition, as was indicated by the c-c dihedral angles ( $23.3 \pm 13.1^\circ$ ) of the crystal structure of **hoop**  $\Phi_{30}$ , the planarity at the circumference of the molecule was not observed in the conformers.<sup>16</sup> These two characteristics (*i.e.*, flexible structure and non-cylindrical shape) of the largest congener were in stark contrast to those found with the smallest **hoop**  $\Phi_{18}$  congener. As expected, the middle-size congener, **hoop**  $\Phi_{24}(\text{H})$ , showed intermediary characteristics. Thus, as was seen in the conformation picture, the deviation of the conformers from the global

minimum was not as extreme as that observed with **hoop**  $\Phi_{30}$ . However, deviations of conformations from a cylindrical shape were noticeable, mostly due to the large c-c dihedral angles at the circumference. As was observed in the crystal structure as  $35.8 \pm 2.3^\circ$ , the dihedral angles of c-c linkages were mostly found around a standard biaryl angle of *ca.*  $30^\circ$ .<sup>13,16</sup> The observations showed that the cylindrical shape found in the lengthened molecule [(12,12)-pNT] with the identical width originated from the doubly/triply connected frameworks.<sup>6</sup> Such unique comparisons have not been made with polyarenes, as fully belted congeners of [n]CPP have scarcely been prepared.<sup>22</sup> The dependency of the structural flexibility of **hoop**  $\Phi_{6n}$  on the panel numbers was similarly observed in small cyclonaphthylenes.<sup>23</sup>

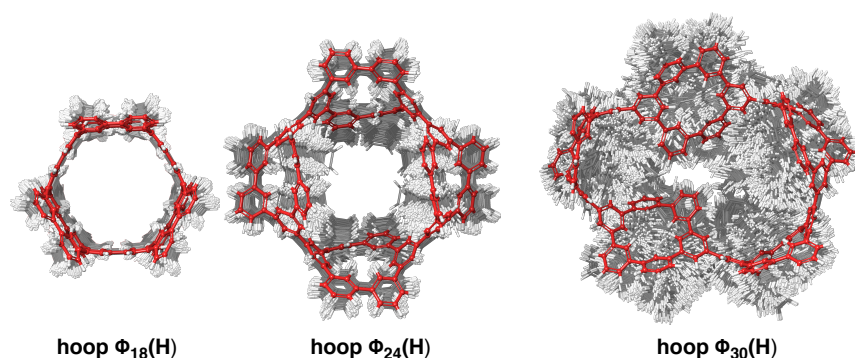


**Figure 4.** Lowest-energy conformers of **hoop**  $\Phi_{6n}(\text{H})$  ( $\leq 5$  kcal/mol). Global minima are shown in red. The conformation search was performed with the MMFF94 force field for low-mode sampling of 2000 structures.

## 2.6 Porosity of crystals

Close examination of the crystal packings revealed an interesting porous nature of the crystals. As was observed with the pNT molecules,<sup>6</sup> cylindrical pores of molecules were aligned to form nanopores with **hoops**  $\Phi_{18}$  and  $\Phi_{30}$  molecules (Figure 5). The packing structure of **hoop**  $\Phi_{24}$  was different, and a pore of one molecule was crowned by a rim of neighboring molecules. Because the **hoop**  $\Phi_{24}$  molecule possessed the identical geometrical width as the (12,12)-pNT molecule, we did not expect this packing deviation with **hoop**  $\Phi_{24}$  molecules. Among various factors that could affect packing structures, we think that the flexibility of the molecule may play an important role. Indeed, the shape of **hoop**  $\Phi_{24}$  was severely deformed as oval shapes in the crystal (see Figure 3). The difference in the packing structure also resulted in a difference in the void fractions.<sup>24</sup> Thus, the void fractions of nanoporous crystals of **hoops**  $\Phi_{18}$  and  $\Phi_{30}$  exceeded 50%,



whereas that of **hoop**  $\Phi_{24}$  was below 50% (Figure 5).

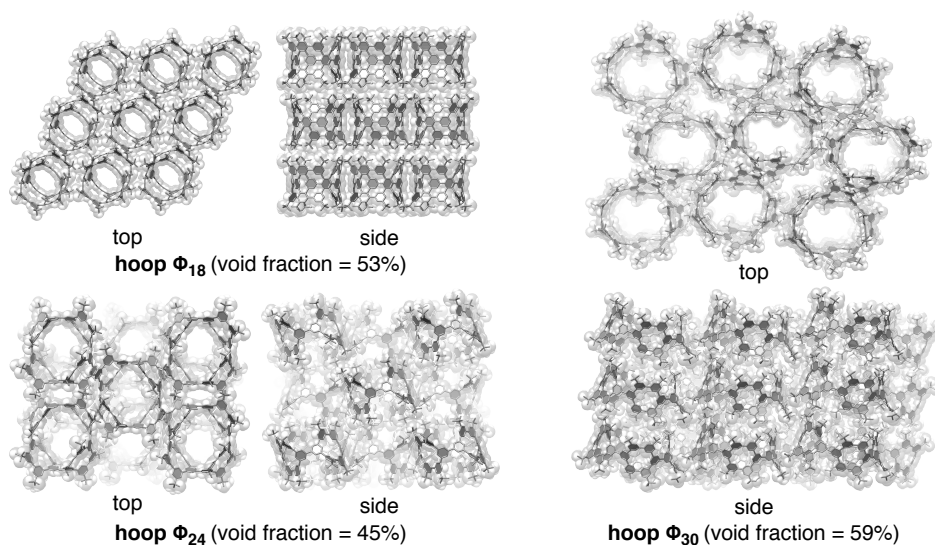


**Figure 5.** Crystal packings of **hoop**  $\Phi_{6n}$ . The void fractions were calculated at procrystal electron density of 0.002 au.

## 2.7 Host–guest chemistry

Considering the void spaces in the crystalline state, we investigated the host–guest chemistry of **hoop**  $\Phi_{6n}$  molecules to find unique supramolecular complexes with fullerene molecules. In their ideal cylindrical shapes, the diameters of **hoop**  $\Phi_{6n}$  are 1.24, 1.65 and 2.06 nm for  $n = 3, 4$  and  $5$ , respectively.<sup>5,25</sup> The diameter of **hoop**  $\Phi_{18}$  PF was smaller than those of [10] and [11]CPP (1.37/1.51 nm) that were known as hosts for  $C_{60}/C_{70}$  fullerenes.<sup>26,27</sup> On the other hand, the diameters of **hoop**  $\Phi_{24}$  and  $\Phi_{30}$  were larger than those of [10] and [11]CPP hosts. Thus, the changes noted by NMR spectroscopy were not fully expected. When we mixed each of the **hoop**  $\Phi_{6n}$  molecules with  $C_{60}$  or  $C_{70}$ , we noted considerable changes in the  $^1\text{H}$  NMR spectra with a combination of **hoop**  $\Phi_{24}$  and  $C_{70}$  among the six possible combinations (Figure 6). The middle-sized molecule, **hoop**  $\Phi_{24}$ , hence accommodated  $C_{70}$  in solution, which was unexpected, given that [12]CPP with an identical diameter failed to serve as a host for  $C_{60}/C_{70}$ .<sup>26</sup> As shown in Figure 6, the aromatic  $^1\text{H}$  NMR resonances of **hoop**  $\Phi_{24}$  shifted towards upfield regions upon increasing the  $C_{70}$  guest, which also indicated the presence of rapid in-and-out exchange processes.<sup>28,29</sup> The stoichiometry of the complexation was determined to be 1:1 by the Job plot analysis with the most affected resonance (proton c; Figure 6). The association constant was also determined to be  $4.7 \times 10^4 \text{ M}^{-1}$ , which was slightly lower

than that reported for a smaller host of [11]CPP ([11]CPP $\supset$ C<sub>70</sub>,  $K_a = 5.3 \times 10^5 \text{ M}^{-1}$ ).<sup>26</sup>

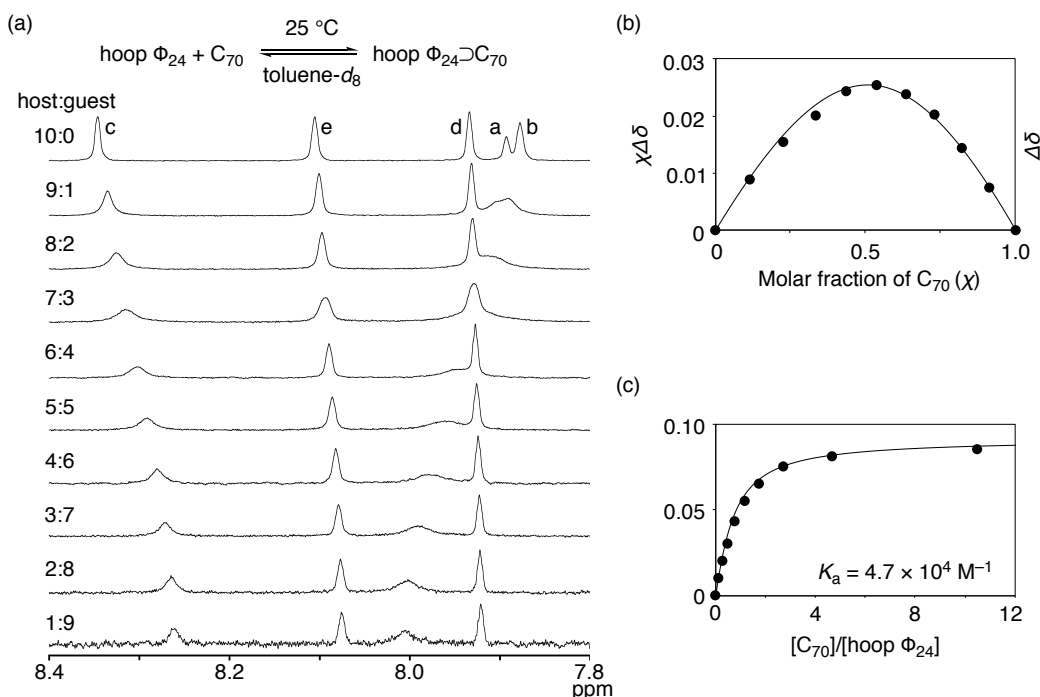


**Figure 6.** Solution-phase complexation of **hoop Φ<sub>24</sub>** with C<sub>70</sub>. (a) Aromatic region of <sup>1</sup>H NMR spectra in toluene-*d*<sub>8</sub> (25 °C, total concentration =  $4.3 \times 10^{-5} \text{ M}$ ; see Supporting Information for details). Resonances were assigned by the NOESY spectrum (see Supporting Information). The resonance of proton c showed the largest change upon addition of C<sub>70</sub> and was used for the Job plot and binding analyses. (b) The Job plot. (c) Fitting analysis to determine the association constant.

Single crystals of **hoop Φ<sub>24</sub>** encapsulating C<sub>70</sub> were obtained, but we were surprised by unexpected compositions and structures. Single crystals were grown with two different host-to-guest ratios, *i.e.*, 1:1 and 1:2, to reveal common structures having an unexpected host-to-guest ratio (see Supporting Information for details). Thus, as shown in Figure 7, a 1:3 complex of **hoop Φ<sub>24</sub>** and C<sub>70</sub> was found in the crystal with one C<sub>70</sub> molecule entrapped at the center and two C<sub>70</sub> molecules located at the side (Figure 7). As we only detected the 1:1 complex in the solution-phase analyses, we believe that the two extra C<sub>70</sub> molecules at the side were entrapped to fill the void space potentially created by **hoop Φ<sub>24</sub>** in the absence of C<sub>70</sub> (void fraction = 45%; see Figure 5). This filling effect of C<sub>70</sub> may also account for the 1:3 complex of (12,12)-pNT and C<sub>70</sub> molecules in the crystal.<sup>6</sup> The structural deformation of the **hoop Φ<sub>24</sub>** host was another interesting feature noted for

the co-crystal of C<sub>70</sub>. Thus, the dihedral angles of the C<sub>70</sub>-free crystal were 35.8±2.3° (c-c), 40.7±14.4° (a-b) and 26.8±7.6° (b-b) (Figure 3d), which were altered to 42.9±6.0° (c-c), 40.1±9.1° (a-b) and 14.2±10.0° (b-b) upon complexation with C<sub>70</sub>. Thus, the C-C bonds located at the circumference were considerably deformed to encapsulate the C<sub>70</sub> guests.

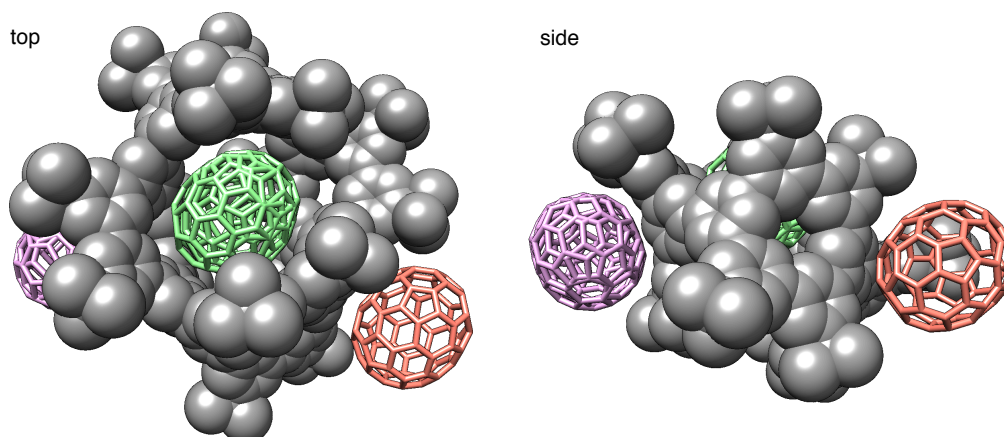


**Figure 7.** Crystal structures of the hoop-shaped phenine nanocarbon ( $n = 4$ ) with C<sub>70</sub>. Solvent molecules and hydrogen atoms are omitted for clarity. Three locations of C<sub>70</sub> are shown in different colors.

## 2.8 Conclusion

In summary, we have synthesized phenine nanocarbon that possess isorecticular frameworks of [ $n$ ]CPP. The Pt-mediated macrocyclization allowed for the synthesis of three congeners with differing panel numbers. A combination of various structural analyses revealed structural features unique to each panel number. The smallest **hoop**  $\Phi_{18}$  congener possessed a rigid cylindrical shape that can be regarded as a (9,9)-carbon nanotube segment with periodic vacancy defects ( $t_f = 4.0$ ,  $F_a = 67\%$ ,  $F_b = 57\%$ ).<sup>6,17</sup> A unique fluctuating structure was indicated with the largest **hoop**  $\Phi_{30}$  congener. The structural fluctuations of the middle-size **hoop**  $\Phi_{24}$  congener resulted in an apparent change in the packing structure, which showed a stark difference from that found with the lengthened, rigid pNT molecules. The induced-fit encapsulation of C<sub>70</sub> is another unique feature of the flexible phenine nanocarbons. We believe that explorations of the **hoop**  $\Phi_{6n}$  derivatives should enrich the chemistry related to [ $n$ ]CPP. To deepen our understanding of periodic defects with the nanocarbon molecules, further careful analyses of unique structures are particularly important.

## 2.9 Supplementary data

### General

All the reactions were performed under N<sub>2</sub> atmosphere. Flash silica gel column chromatography was performed on silica gel 60N (spherical and neutral gel, 40–50 μm, Kanto). Gel permeation chromatography was performed on YMC LC-forte/R (columns: YMC GPC T2000 and T4000) and JAI LC-9104 (columns: JAIGEL-1H-40, 2H-40 and 2.5H-40) both equipped with UV and RI detectors with chloroform as the eluent. Preparative high-performance liquid chromatography (HPLC) was performed on JASCO LP-2000 Plus series systems equipped with a UV detector with COSMOSIL Buckyprep 20 φ × 250 mm or COSMOSIL Cholest 20 φ × 250 mm. Analytical HPLC was performed on JASCO LP-2000 Plus series systems with COSMOSIL Buckyprep 4.6 φ × 250 mm at the flow rate of 1.0 mL/min at 40 °C in a column oven under UV detection at 260 nm. Proton (<sup>1</sup>H), carbon (<sup>13</sup>C) NMR spectra were recorded on JEOL JNM-ECA 600 II (<sup>1</sup>H: 600 MHz; <sup>13</sup>C: 150 MHz) and JEOL JNM-ECS 400 (<sup>1</sup>H: 400 MHz; <sup>13</sup>C: 100 MHz). Chemical shift values are given in ppm relative to internal CHCl<sub>3</sub> (<sup>1</sup>H NMR: δ 7.26; <sup>13</sup>C NMR: δ 77.16). Ultraviolet-visible (UV-vis) spectroscopy was performed on JASCO V-670 equipped with JASCO ETC-717 temperature controller. Fluorescence spectroscopy was performed on JASCO FP-8500 equipped with JASCO ETC-815 temperature controller. High-resolution mass spectrometry was performed on Bruker autoflex speed by matrix-assisted laser desorption/ionization (MALDI) method and on Bruker micrOTOF II by atmospheric pressure photoionization (APPI) and atmospheric pressure chemical ionization (APCI) methods.

Solvents and reagents were purchased from TCI Co., Ltd., Wako Pure Chemical Industries, Ltd., Kanto Chemical Co., Inc., and Sigma-Aldrich Co. Anhydrous THF, DMF and toluene were purified by a solvent purification system (GlassContour) equipped with columns of activated alumina and supported copper catalyst (Q-5). All other chemicals were of reagent grade and used without any further purification.

### Synthesis of Substrates

*1,3-Benzenediboronic acid bis(pinacol) ester (1)*: To a mixture of bis(pinacolato)diboron (59.2 g, 233 mmol), PdCl<sub>2</sub>(dppf)•CH<sub>2</sub>Cl<sub>2</sub> (8.66 g, 10.6 mmol) and

KOAc (52.0 g, 529 mmol) in DMSO (500 mL) was added 1,3-dibromobenzene (25.0 g, 106 mmol). The mixture was stirred at 80 °C for 16 h, and H<sub>2</sub>O (500 mL) was added to it. The precipitate was collected by vacuum filtration, washed with water and methanol, dried over Na<sub>2</sub>SO<sub>4</sub> and purified by silica gel chromatography (eluent: hexane/ethyl acetate = 10:1). The title compound was obtained as a white powder in 91% yield (31.8 g, 96.3 mmol). Spectra of **1** were identical to the data found in literature.<sup>30</sup>

*3,3''-Dibromo-5,5''-di-tert-butyl-1,1':3',1''-terphenyl (2)*: A mixture of diboronate ester **1** (2.00 g, 6.06 mmol), 1,3-dibromo-5-*tert*-butylbenzene (5.31 g, 18.2 mmol) and Pd(PPh<sub>3</sub>)<sub>4</sub> (350 mg, 0.303 mmol) and K<sub>2</sub>CO<sub>3</sub> (12.6 g, 91.2 mmol) in DMF (150 mL) was added a solution of K<sub>2</sub>CO<sub>3</sub> (4.18 g, 30.3 mmol) in water (30 mL). The mixture was stirred at 80 °C for 16 h and extracted with ethyl acetate (1 L). The organic layer was dried over Na<sub>2</sub>SO<sub>4</sub>, concentrated and purified by silica gel column chromatography (eluent: hexane) to afford the title compound as a colorless oil in 60% yield (1.80 g, 3.61 mmol). <sup>1</sup>H NMR (400 MHz, CDCl<sub>3</sub>) δ 7.66 (s, 1H), 7.58 (t, *J* = 1.6 Hz, 2H), 7.54–7.52 (m, 7H), 1.37 (s, 18H); <sup>13</sup>C{<sup>1</sup>H} NMR (100 MHz, CDCl<sub>3</sub>) δ 153.9, 142.8, 141.1, 129.3, 127.7, 127.5, 126.7, 126.3, 123.3, 122.8, 35.1, 31.2; HRMS (APCI) *m/z* [M]<sup>+</sup> calcd for C<sub>26</sub>H<sub>28</sub>Br<sub>2</sub> 500.0532, found 500.0546.

*[6]CMP derivative 3*: A mixture of Ni(cod)<sub>2</sub> (6.08 g, 22.1 mmol), 2,2'-bipyridine (3.42 g, 21.9 mmol) and cycloocta-1,5-diene (2.70 mL, 21.8 mmol) was stirred at 80 °C in a mixed solvent of DMF (120 mL) and toluene (400 mL) for 1 h. To the mixture was slowly added terphenyl **2** (3.63 g, 7.26 mmol) in toluene (200 mL) over 30 min. After an additional stir for 18 h, the mixture was cooled down to ambient temperature and was stirred overnight after addition of aqueous solution of HCl (3 M, *ca.* 500 mL). After removal of the aqueous layer, the organic layer was concentrated and the resulting solid was washed with methanol (300 mL) and CHCl<sub>3</sub> (20 mL) to afford the title compound as a white powder in 79% yield (1.96 g, 2.88 mmol). <sup>1</sup>H NMR (400 MHz, CDCl<sub>3</sub>) δ 8.34 (s, 2H), 8.13 (s, 4H), 7.76–7.72 (m, 12H), 7.58 (t, *J* = 7.6 Hz, 2H), 1.49 (s, 36H); <sup>13</sup>C{<sup>1</sup>H} NMR (100 MHz, CDCl<sub>3</sub>) δ 152.3, 141.7, 141.6, 129.3, 127.7, 125.2, 124.9, 122.6 (2C), 35.1, 31.6; HRMS (APPI) *m/z* [M]<sup>+</sup> calcd for C<sub>52</sub>H<sub>56</sub> 680.4376, found 680.4391.

*[6]CMP derivative 4*: A mixture of **3** (400 mg, 0.590 mmol), bis(pinacolato)diboron (598 mg, 2.35 mmol), [Ir(cod)(OMe)]<sub>2</sub> (78.0 mg, 0.560 mmol) and 4,4'-di-*tert*-butyl-2,2'-bipyridine (63.0 mg, 0.240 mmol) in THF (115 mL) was stirred at 65 °C for 24 h. The solvent was removed in vacuo and the residue was washed with methanol to afford the

title compound as a white powder in 97% yield (534 mg, 0.573 mmol).  $^1\text{H}$  NMR (400 MHz,  $\text{CDCl}_3$ )  $\delta$  8.39 (s, 2H), 8.14 (s, 4H), 8.05 (s, 4H), 7.79 (s, 4H), 7.71 (s, 4H), 1.50 (s, 36H), 1.44 (s, 24H);  $^{13}\text{C}\{^1\text{H}\}$  NMR (100 MHz,  $\text{CDCl}_3$ )  $\delta$  152.2, 141.5, 141.3, 141.0, 131.5, 131.0, 124.9, 122.9, 122.7, 84.0, 35.1, 31.7, 24.9; HRMS (APPI)  $m/z$   $[\text{M}]^+$  calcd for  $\text{C}_{64}\text{H}_{78}\text{B}_2\text{O}_4$  932.6081, found 932.6082.

### Synthesis of hoop $\Phi_{6n}$

A mixture of **4** (200 mg, 0.210 mmol),  $\text{PtCl}_2(\text{cod})$  (80.4 mg, 0.210 mmol) and  $\text{CsF}$  (320 mg, 2.10 mmol) in THF (21 mL) was stirred at 65 °C for 24 h. The solvent was removed by vacuo, and the residue was diluted with toluene (10 mL). After addition of  $\text{PPh}_3$  (550 mg, 2.10 mmol), the mixture was stirred at 100 °C for 17 h. The resulting mixture was poured into methanol (1 L) to afford a crude solid material. The crude material was roughly purified by passing through a pad of silica gel and then separated by GPC and HPLC to afford hoop  $\Phi_{18}$  in 3% (4.0 mg, 2.0  $\mu\text{mol}$ ), hoop  $\Phi_{24}$  in 6% (8.2 mg, 3.0  $\mu\text{mol}$ ) and hoop  $\Phi_{30}$  in 3% yields (3.7 mg, 1.1  $\mu\text{mol}$ ) as white powders.

*hoop  $\Phi_{18}$* :  $^1\text{H}$  NMR (600 MHz,  $\text{CDCl}_3$ )  $\delta$  7.99 (d,  $J$  = 1.4 Hz, 12H), 7.80 (s, 12H), 7.70 (s, 12H), 7.70 (s, 6H), 7.66 (s, 12H), 1.46 (s, 108H);  $^{13}\text{C}\{^1\text{H}\}$  NMR (150 MHz,  $\text{CDCl}_3$ )  $\delta$  152.3, 144.3, 142.6, 138.2, 137.1, 128.1, 126.2, 123.4, 122.2, 120.6, 35.1, 31.6; HRMS (MALDI-TOF)  $m/z$   $[\text{M}]^+$  calcd for  $\text{C}_{156}\text{H}_{162}$  2036.2705, found 2036.2728; UV-vis ( $1.37 \times 10^{-6}$  M,  $\text{CHCl}_3$ ):  $\lambda_{\text{max}}$  = 253 nm (Abs = 0.362), 303 nm (Abs = 0.065); fluorescence (excitation = 254 nm,  $1.37 \times 10^{-6}$  M,  $\text{CHCl}_3$ ):  $\lambda_{\text{max}}$  = 360 nm. A single crystal of hoop  $\Phi_{18}$  suitable for X-ray crystallographic analysis was obtained by vapor diffusion of MeOH into a 1,2-dichloroethane solution of hoop  $\Phi_{18}$  at 25 °C.

*hoop  $\Phi_{24}$* :  $^1\text{H}$  NMR (600 MHz,  $\text{CDCl}_3$ )  $\delta$  8.08 (s, 16H), 7.97 (s, 8H), 7.88 (s, 16H), 7.86 (d,  $J$  = 1.6 Hz, 16H), 7.73 (s, 16H), 1.48 (s, 144H);  $^{13}\text{C}\{^1\text{H}\}$  NMR (150 MHz,  $\text{CDCl}_3$ )  $\delta$  152.3, 143.5, 141.9, 141.1, 138.3, 127.5, 124.8, 124.7, 122.6, 120.8, 35.2, 31.6; HRMS (MALDI-TOF)  $m/z$   $[\text{M}]^+$  calcd for  $\text{C}_{208}\text{H}_{216}$  2715.6964, found 2715.6961; UV-vis ( $1.03 \times 10^{-6}$  M,  $\text{CHCl}_3$ ):  $\lambda_{\text{max}}$  = 259 nm (Abs = 0.445); fluorescence (excitation = 254 nm,  $1.03 \times 10^{-6}$  M,  $\text{CHCl}_3$ ):  $\lambda_{\text{max}}$  = 356 nm. A single crystal of hoop  $\Phi_{24}$  suitable for X-ray crystallographic analysis was obtained by vapor diffusion of 2-propanol into a  $\text{CHCl}_3$  solution of hoop  $\Phi_{24}$  at 25 °C.

*hoop  $\Phi_{30}$* :  $^1\text{H}$  NMR (600 MHz,  $\text{CDCl}_3$ )  $\delta$  8.27 (s, 20H), 8.17 (s, 10H), 8.01 (d,  $J$  = 1.2 Hz, 20H), 7.91 (s, 20H), 7.82 (s, 20H), 1.49 (s, 180H);  $^{13}\text{C}\{^1\text{H}\}$  NMR (150 MHz,

CDCl<sub>3</sub>)  $\delta$  152.5, 142.8, 141.4, 141.3, 138.7, 126.9, 124.3, 124.0, 122.6, 121.2, 35.2, 31.6; HRMS (MALDI-TOF)  $m/z$  [M]<sup>+</sup> calcd for C<sub>260</sub>H<sub>270</sub> 3394.1189, found 3394.1166; UV-vis (5.94  $\times$  10<sup>-7</sup> M, CHCl<sub>3</sub>):  $\lambda_{\text{max}}$  = 261 nm (Abs = 0.301); fluorescence (excitation = 254 nm, 5.94  $\times$  10<sup>-7</sup> M, CHCl<sub>3</sub>):  $\lambda_{\text{max}}$  = 359 nm. A single crystal of hoop  $\Phi_{30}$  suitable for X-ray crystallographic analysis was obtained by vapor diffusion of MeOH into a CHCl<sub>3</sub> solution of hoop  $\Phi_{30}$  at 25 °C.

### Complexation of hoop $\Phi_{24}$ with C<sub>70</sub>

The association behavior between hoop  $\Phi_{24}$  and C<sub>70</sub> was analyzed by <sup>1</sup>H NMR spectroscopy. We first prepared solutions of hoop  $\Phi_{24}$  (4.0  $\times$  10<sup>-5</sup> M in toluene-*d*<sub>8</sub>) and C<sub>70</sub> (4.6  $\times$  10<sup>-5</sup> M in toluene-*d*<sub>8</sub>). Aliquots of each solution were then mixed by varying their ratio so that the total concentration became 4.3  $\times$  10<sup>-5</sup> M, and the mixed solutions were subjected to the NMR analysis at 25 °C. The chemical-shift of the five proton resonances moved upfield as the mole fraction of C<sub>70</sub> increased (Figure 6a). The most prominent change was observed in the resonance labeled c, and thus it was used for the analysis. The chemical shift changes relative to free hoop  $\Phi_{24}$  ( $\Delta\delta$ ) were used for the Job plot analysis, revealing the 1:1 complexation (Figure 6b). The  $\Delta\delta$  values were also plotted against the molar fraction of C<sub>70</sub> to obtain a binding isotherm (Figure 6c). The binding isotherm was subjected to curve fitting analyses with the following equation<sup>31</sup>

$$\Delta\delta = \frac{\delta_{\text{AHG}}}{2} \left\{ 1 + \frac{[\text{C}_{70}]}{[\text{Host}]} + \frac{1}{K_a[\text{Host}]} - \sqrt{\left( 1 + \frac{[\text{C}_{70}]}{[\text{Host}]} + \frac{1}{K_a[\text{Host}]} \right)^2 - 4 \frac{[\text{C}_{70}]}{[\text{Host}]}} \right\}$$

to elucidate two variables,  $K_a$  and  $\delta_{\text{AHG}}$ , where  $K_a$  is the association constant and  $\delta_{\text{AHG}}$  is the change of the chemical shift between free hoop  $\Phi_{24}$  and the complex. A single crystal of the complex suitable for X-ray crystallographic analysis was obtained by slow evaporation of a solution of 1:2 mixture of hoop  $\Phi_{24}$  and C<sub>70</sub> in chlorobenzene/2-propnaol at 25 °C. We also got a single crystal from a 1:1 mixture of hoop  $\Phi_{24}$  and C<sub>70</sub> in *o*-dichlorobenzene/2-propnaol at 25 °C. Both of the crystals shared a similar structure with the 1:3 stoichiometry of hoop  $\Phi_{24}$  and C<sub>70</sub> according to single-crystal X-ray diffraction analyses.

## Crystallographic Analysis

Single-crystal X-ray diffraction analyses were carried out with synchrotron X-ray source at the beamline BL38B1 in the SPring-8 with a Rayonix CCD MX225HE detector or at the beamline BL2S1 in the Aichi Synchrotron Radiation Research Center with an ADSC CCD Q315r detector. The collected diffraction data were processed with the XDS software program.<sup>32</sup> The structure was solved by the direct method with SHELXT program<sup>33</sup> and refined by full-matrix least-squares on  $F^2$  using the SHELXL program suite<sup>34</sup> running on the Yadokari-XG 2009 software program.<sup>35</sup> In the refinements, electron densities attributed to the severely disordered solvent molecules are not modeled and subjected to the PLATON/SQUEEZE protocol.<sup>36,37</sup> The non-hydrogen atoms were analyzed anisotropically, and hydrogen atoms were input at the calculated positions and refined with a riding model.

## MALDI-TOF mass spectra

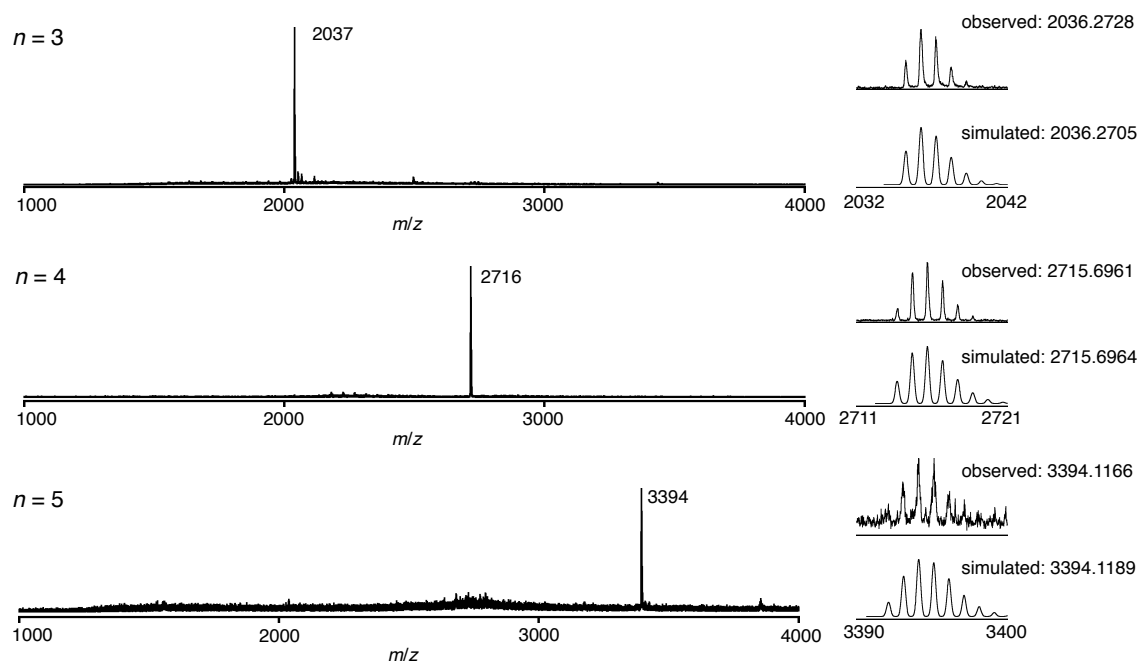


**Figure S1.** MALDI-TOF mass spectra of hoop  $\Phi_{6n}$  (positive mode, matrix: pyrene).



## Chromatograms

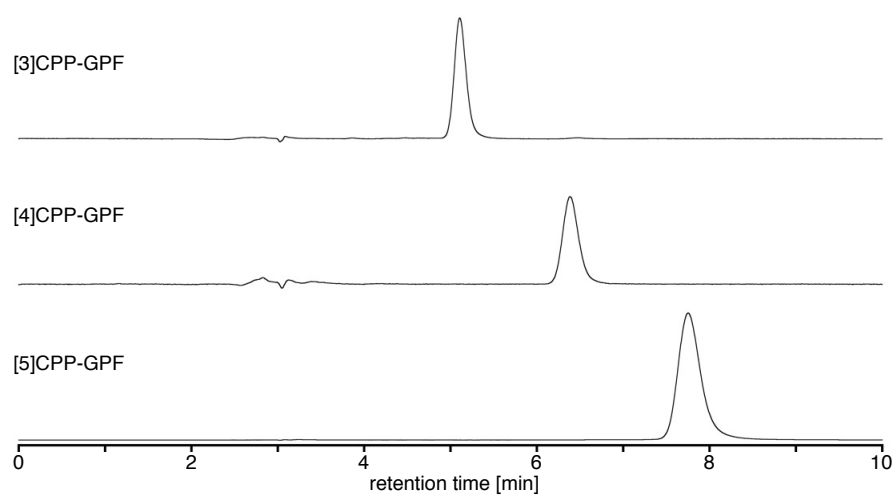


**Figure S2.** HPLC analysis of hoop  $\Phi_{6n}$  with Buckyprep 4.6  $\phi \times 250$  mm. Flow rate: 1.0 mL/min; eluent: 40% methanol/ $\text{CHCl}_3$ ; column temperature: 40 °C; detection wavelength: 260 nm.

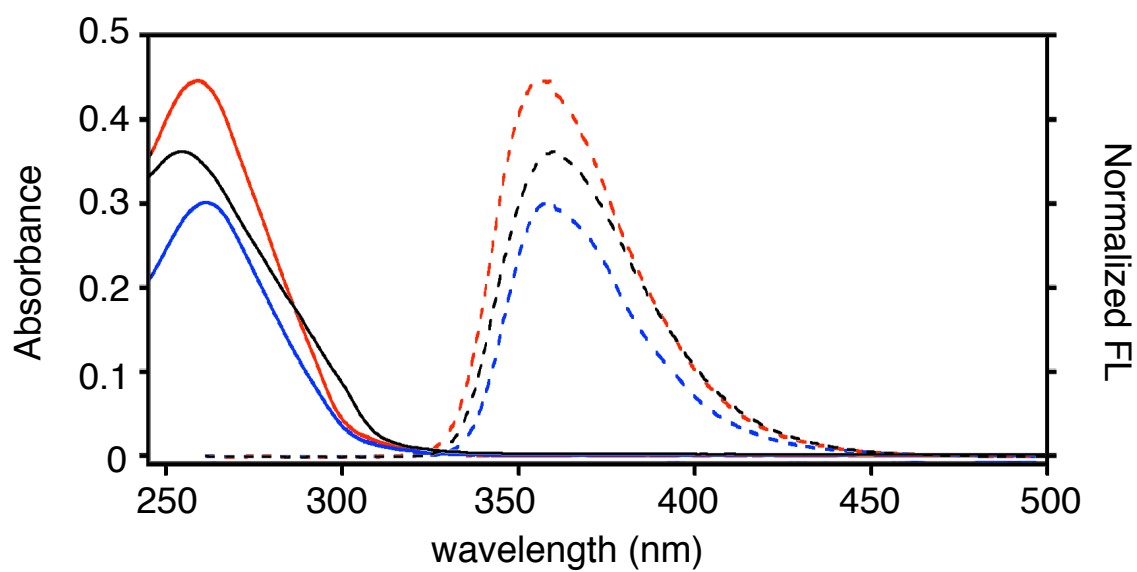


**Figure S3.** Overlaid UV-vis/fluorescence spectra of hoop  $\Phi_{18}$  (black), hoop  $\Phi_{24}$  (red) and hoop  $\Phi_{30}$  (blue) in  $\text{CHCl}_3$ .

# NMR spectra

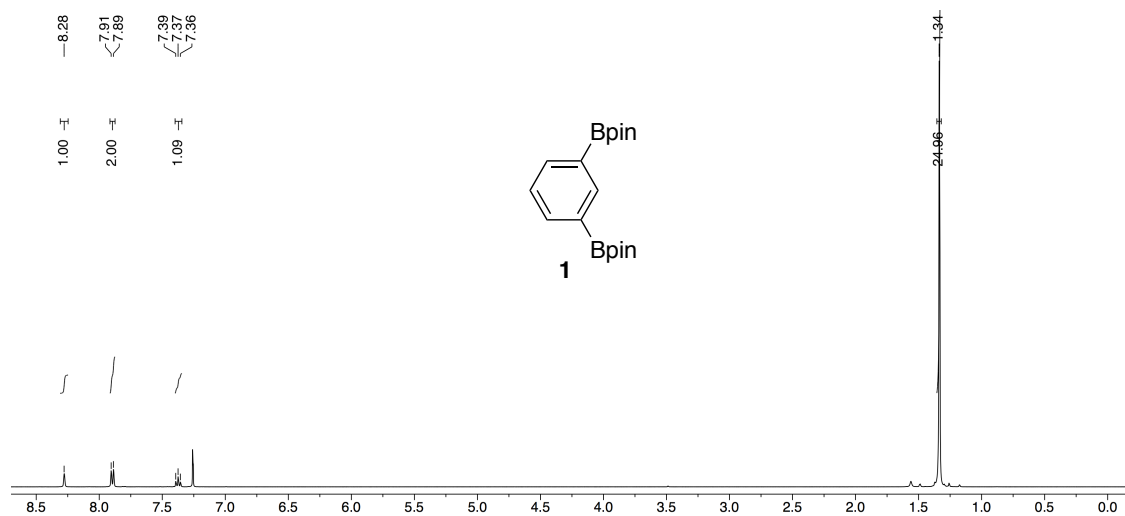


**Figure S4.** <sup>1</sup>H NMR spectrum of **1** in CDCl<sub>3</sub> (25 °C, 600 MHz).

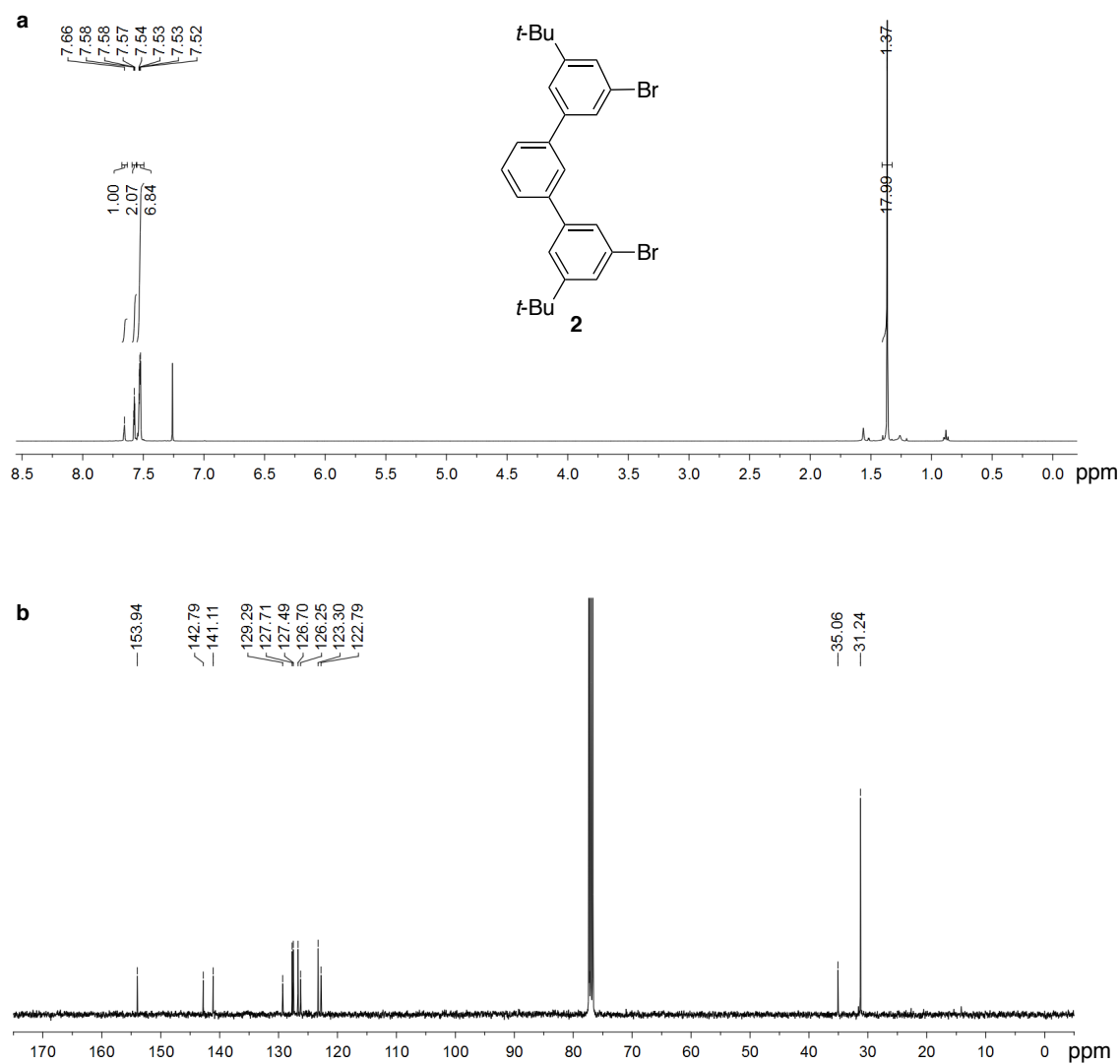


**Figure S5.** (a) <sup>1</sup>H NMR spectrum of **2** in CDCl<sub>3</sub> (25 °C, 400 MHz). (b) <sup>13</sup>C NMR spectrum of **2** in CDCl<sub>3</sub> (25 °C, 100 MHz).

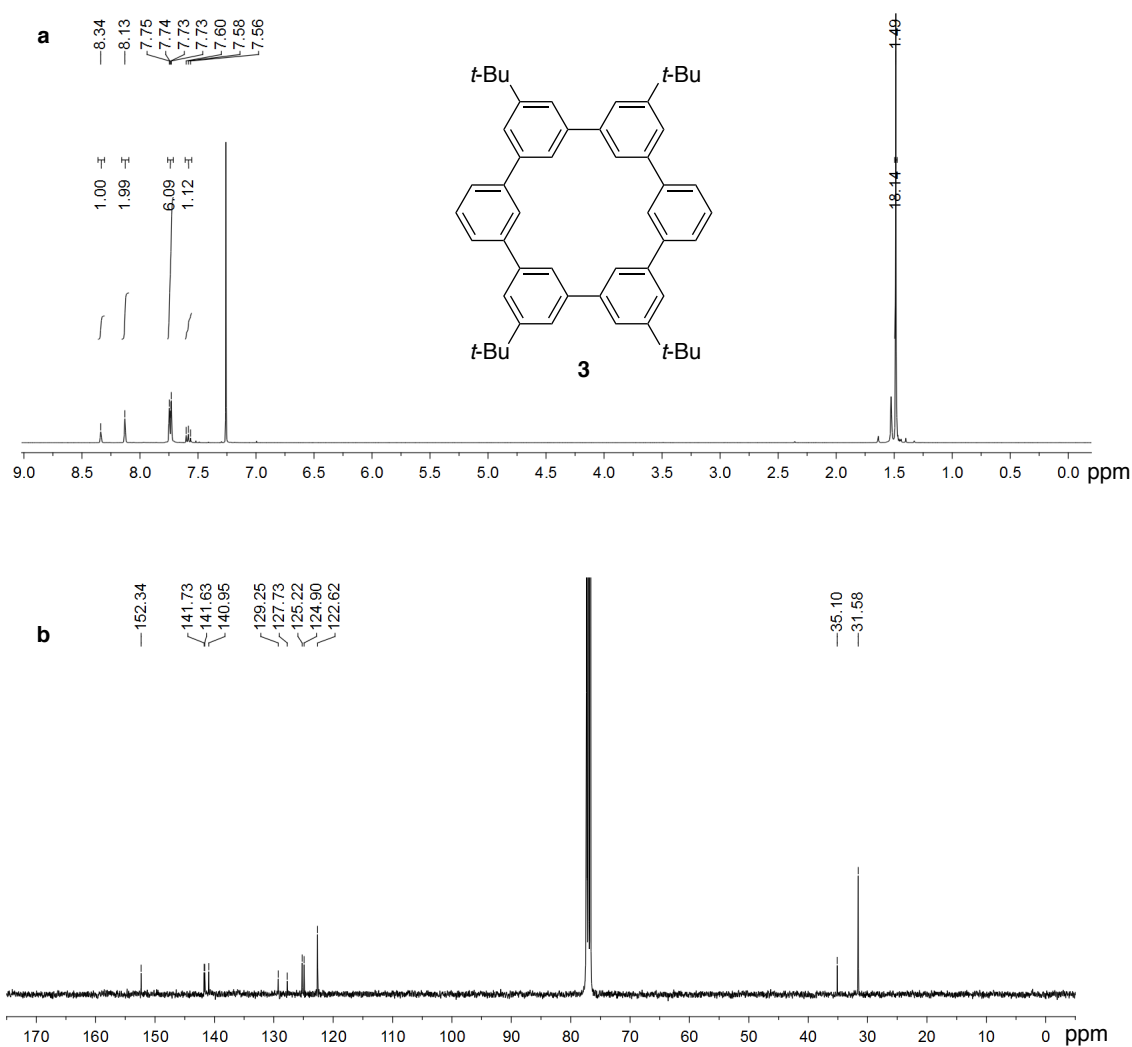


**Figure S6.** (a) <sup>1</sup>H NMR spectrum of **3** in CDCl<sub>3</sub> (25 °C, 400 MHz). (b) <sup>13</sup>C NMR spectrum of **3** in CDCl<sub>3</sub> (25 °C, 100 MHz).

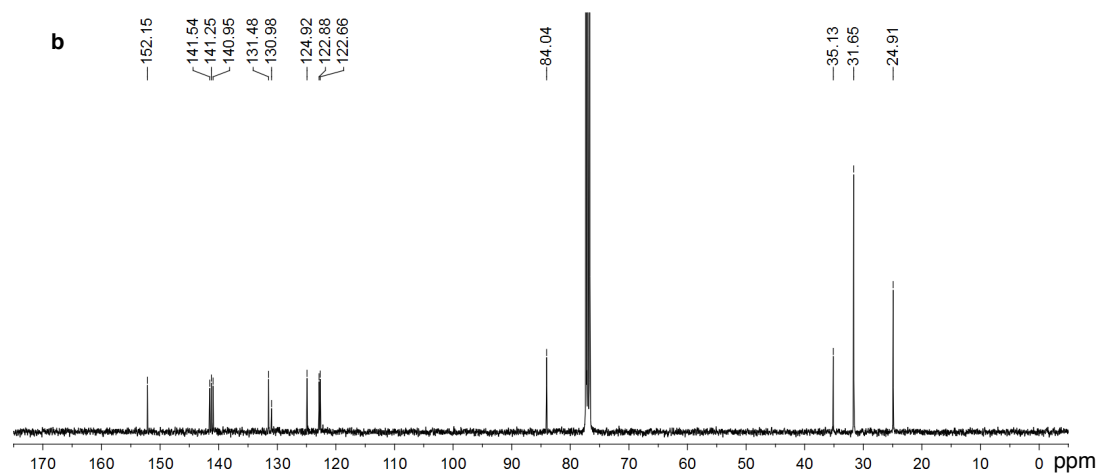
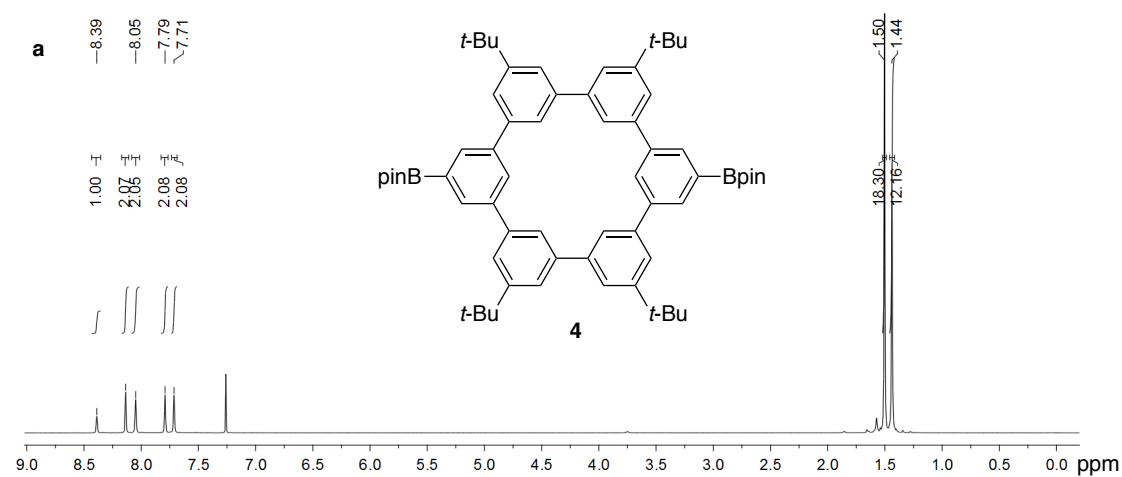


**Figure S7. a** <sup>1</sup>H NMR spectrum of **4** in CDCl<sub>3</sub> (25 °C, 400 MHz). **b** <sup>13</sup>C NMR spectrum of **4** in CDCl<sub>3</sub> (25 °C, 100 MHz).

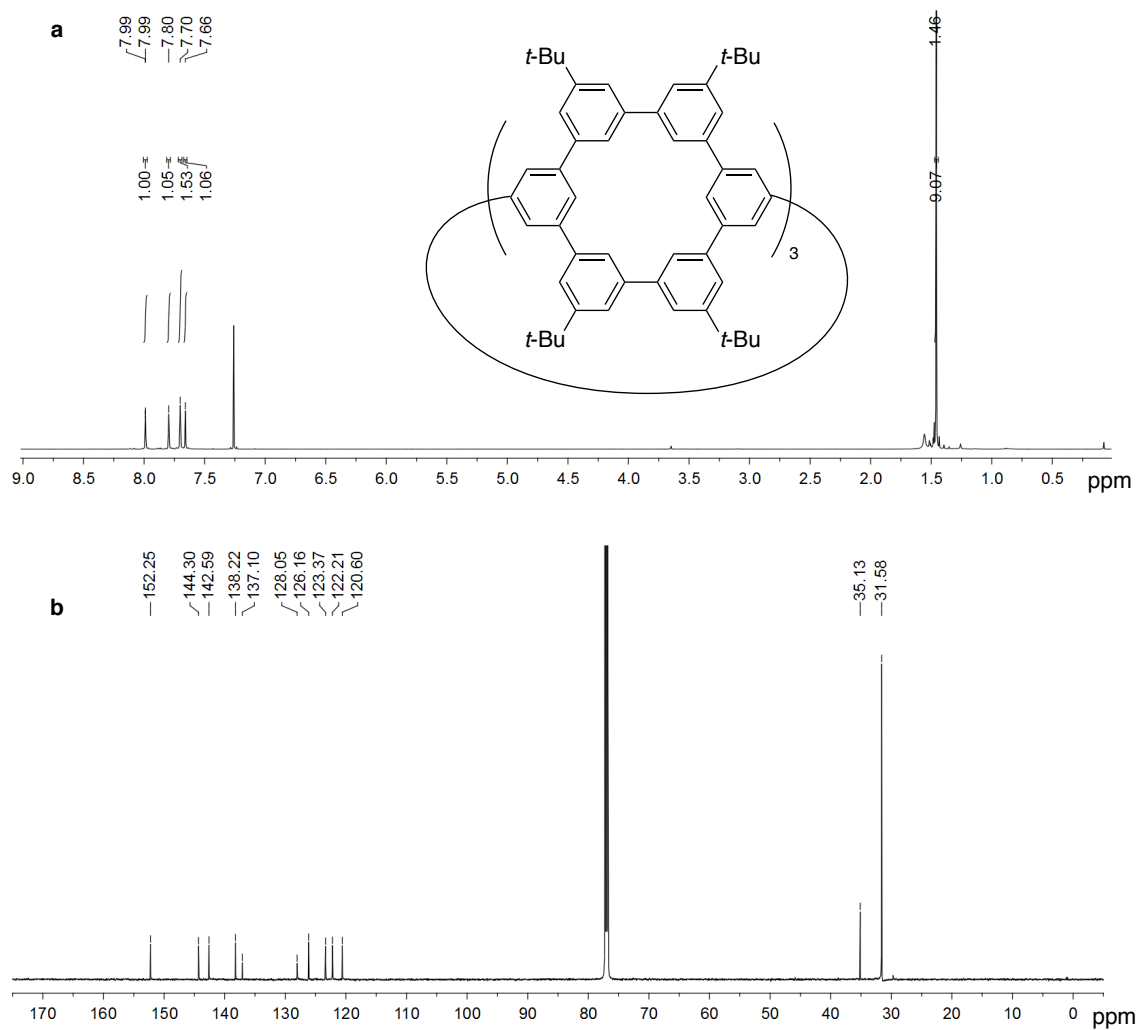


**Figure S8.** (a)  $^1\text{H}$  NMR spectrum of hoop  $\Phi_{18}$  in  $\text{CDCl}_3$  (25  $^\circ\text{C}$ , 600 MHz). (b)  $^{13}\text{C}$  NMR spectrum of hoop  $\Phi_{18}$  in  $\text{CDCl}_3$  (25  $^\circ\text{C}$ , 150 MHz).

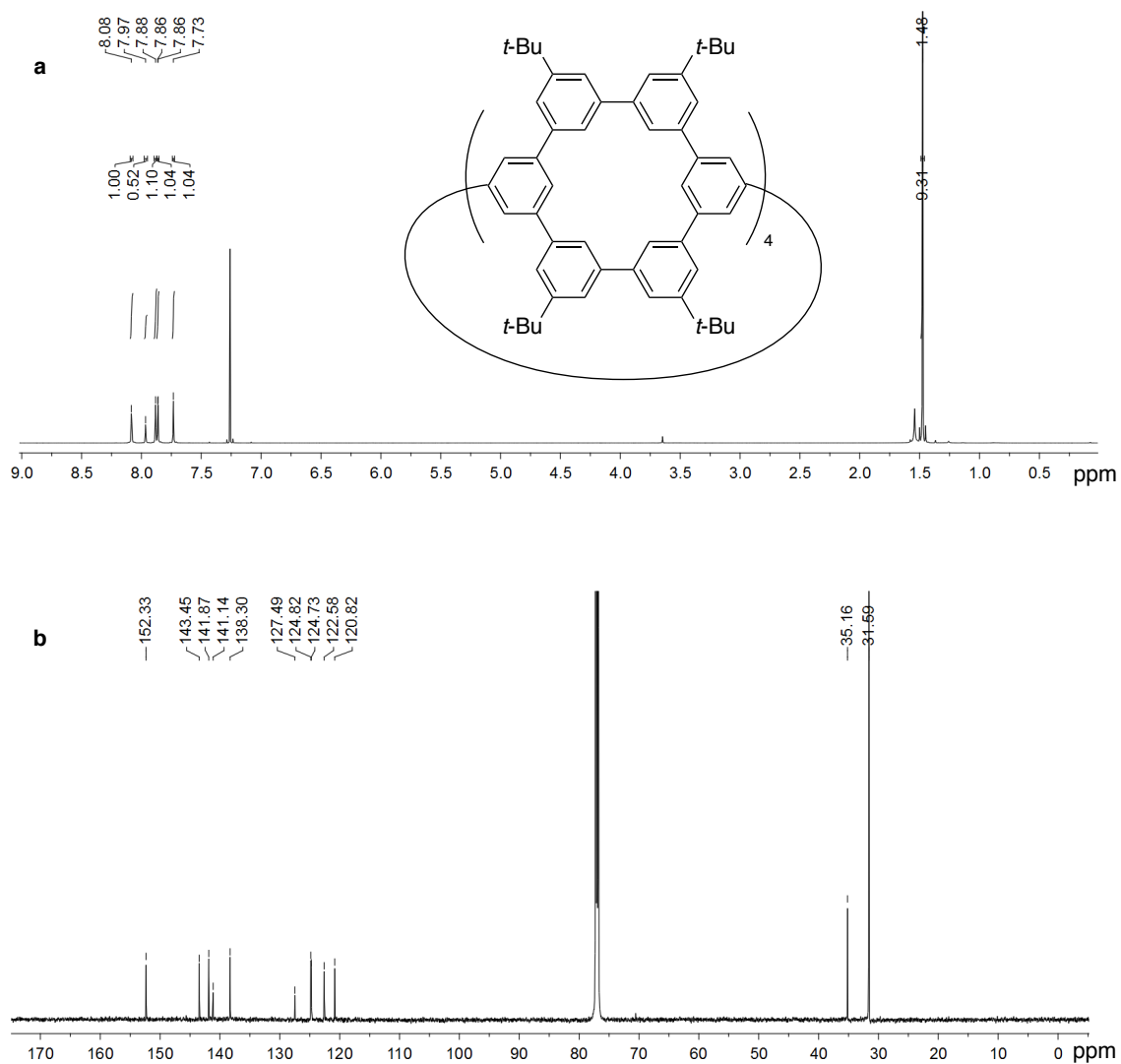


**Figure S9.** (a)  $^1\text{H}$  NMR spectrum of hoop  $\Phi_{24}$  in  $\text{CDCl}_3$  (25 °C, 600 MHz). (b)  $^{13}\text{C}$  NMR spectrum of hoop  $\Phi_{24}$  in  $\text{CDCl}_3$  (25 °C, 150 MHz).



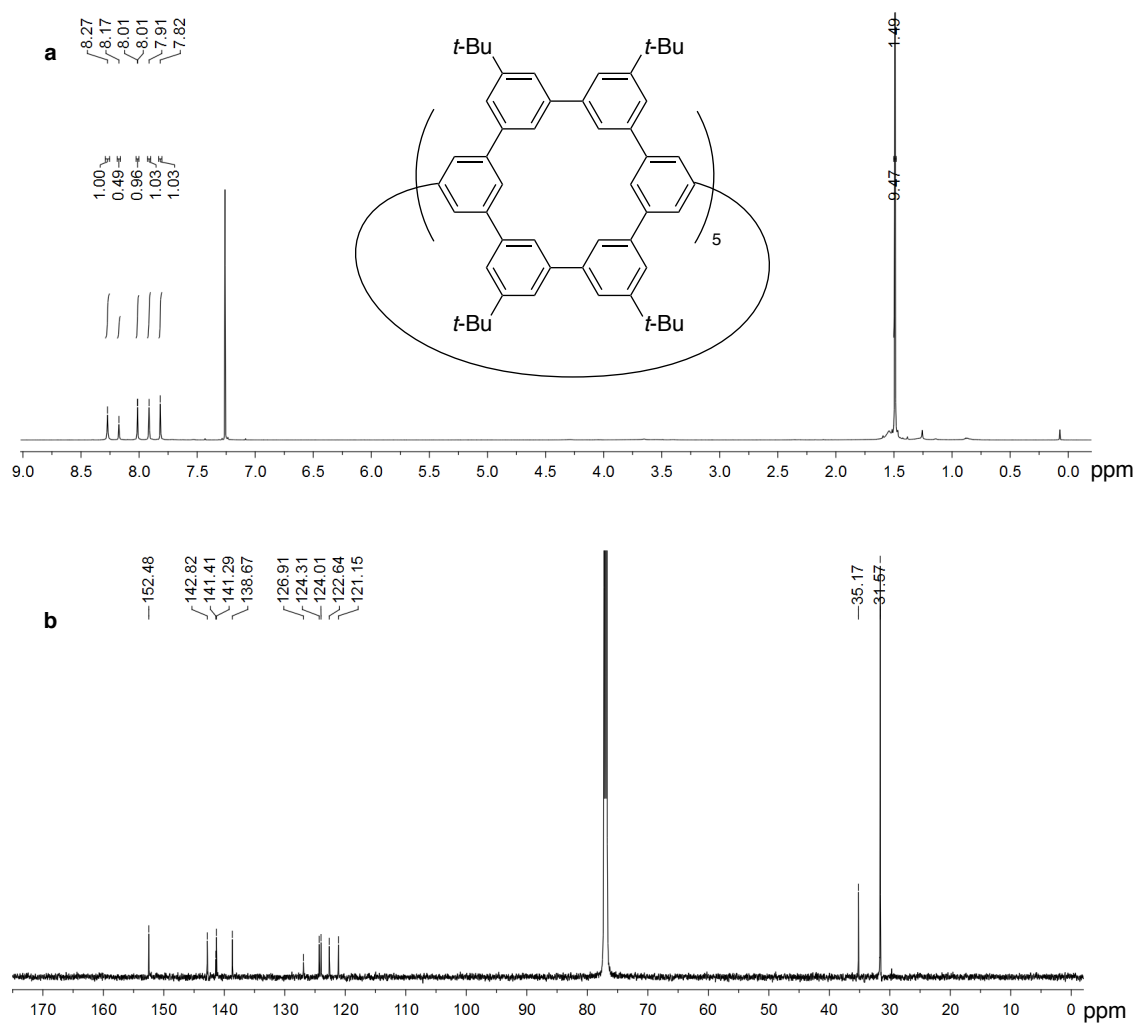


**Figure S10.** (a)  $^1\text{H}$  NMR spectrum of hoop  $\Phi_{30}$  in  $\text{CDCl}_3$  (25  $^\circ\text{C}$ , 600 MHz). (b)  $^{13}\text{C}$  NMR spectrum of hoop  $\Phi_{30}$  in  $\text{CDCl}_3$  (25  $^\circ\text{C}$ , 150 MHz).

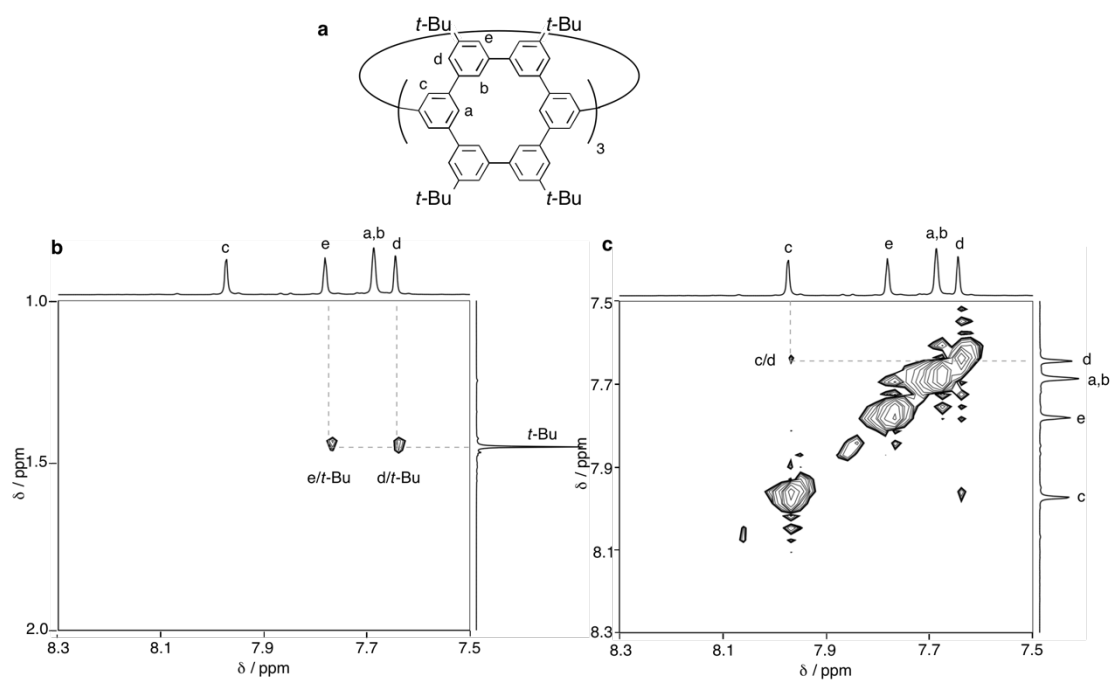


**Figure S11.** (a) Chemical structure for hoop  $\Phi_{18}$ , (b) a NOESY spectrum for aromatic/aliphatic correlations and (c) a NOESY spectrum for aromatic/aromatic correlations in  $\text{CDCl}_3$ .

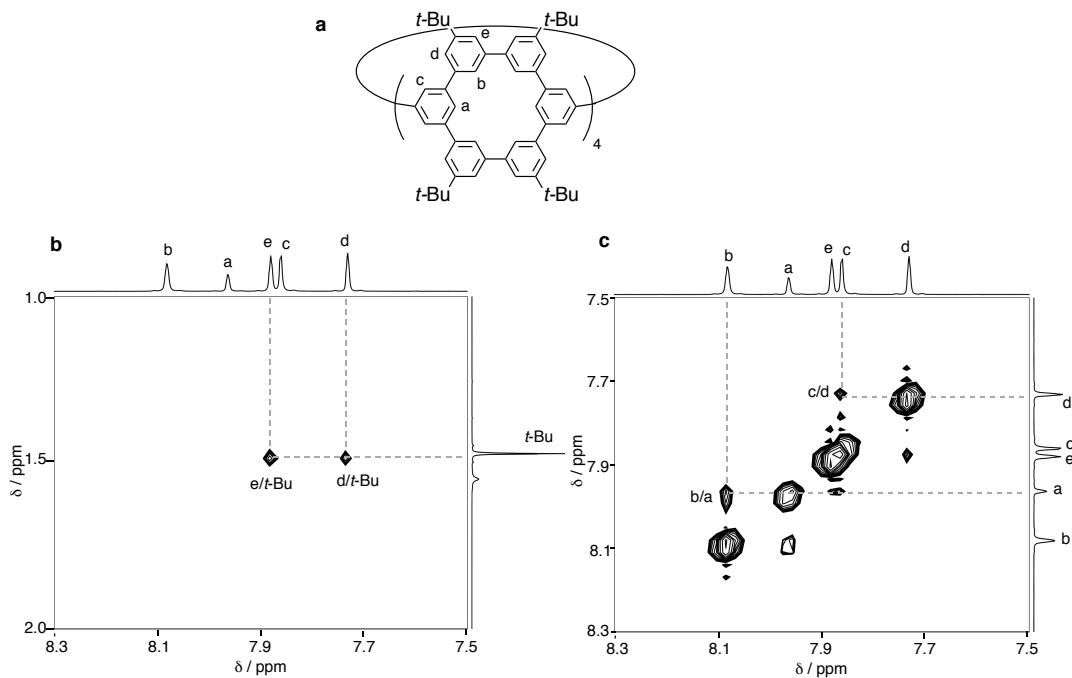


**Figure S12.** a Chemical structure for hoop  $\Phi_{24}$ , b a NOESY spectrum for aromatic/aliphatic correlations and c a NOESY spectrum for aromatic/aromatic correlations in  $\text{CDCl}_3$ .

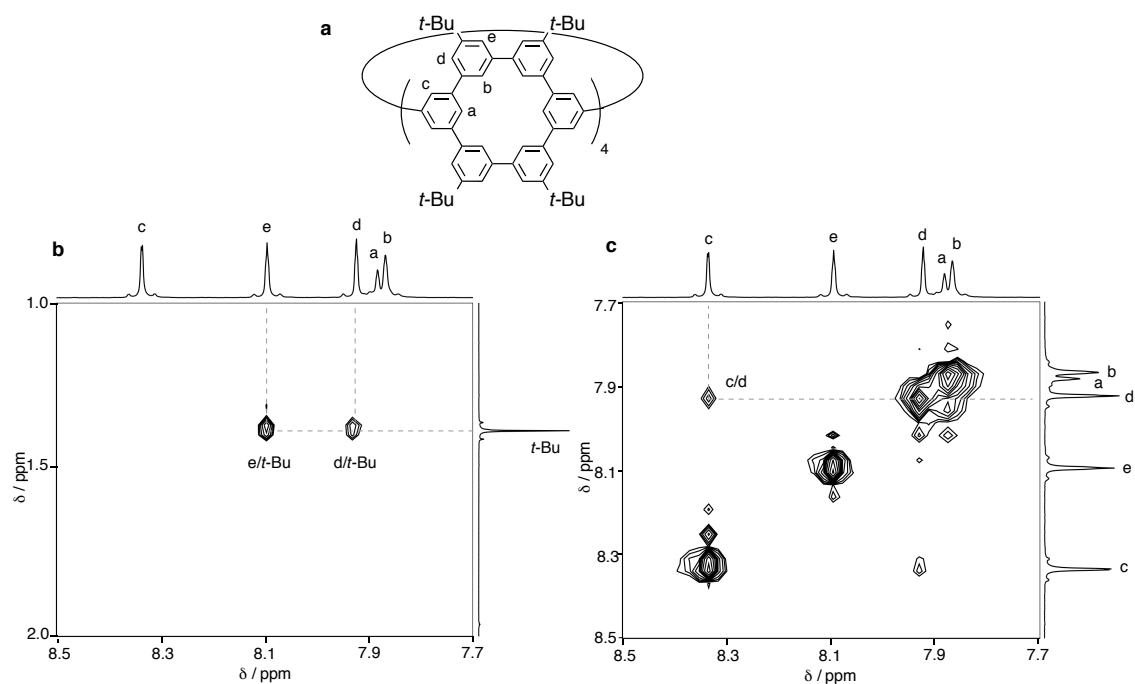


**Figure S13.** (a) Chemical structure for hoop  $\Phi_{24}$ , (b) a NOESY spectrum for aromatic/aliphatic correlations and (c) a NOESY spectrum for aromatic/aromatic correlations in toluene- $d_8$ .

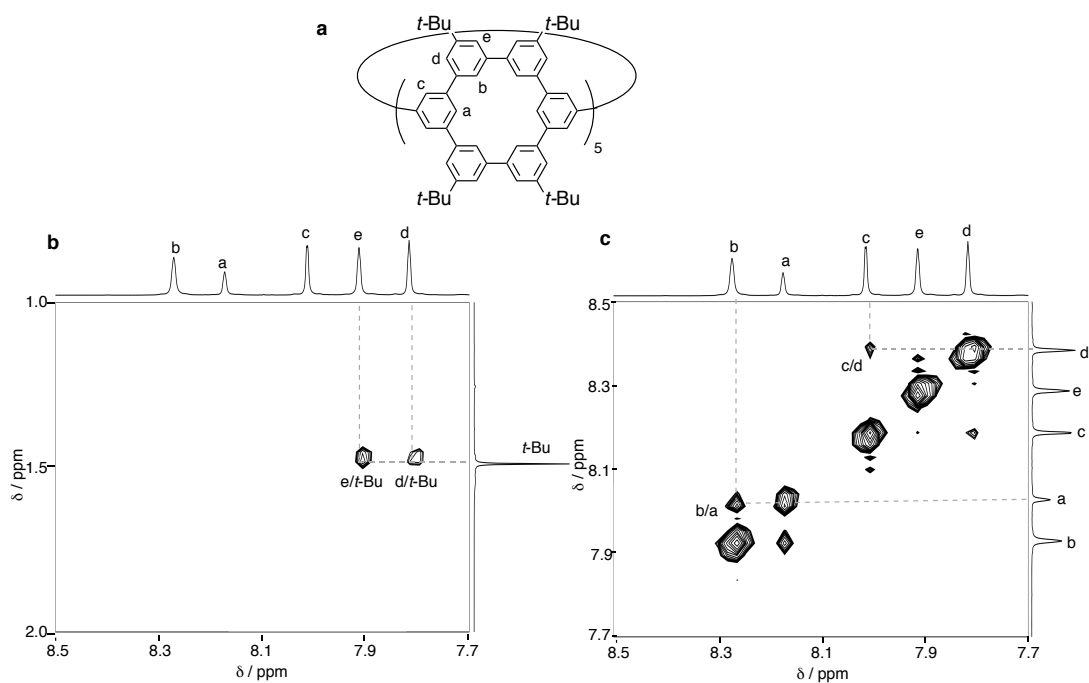


**Figure S14.** (a) Chemical structure for hoop  $\Phi_{30}$ , (b) a NOESY spectrum for aromatic/aliphatic correlations and (c) a NOESY spectrum for aromatic/aromatic correlations in  $\text{CDCl}_3$ .

## Crystallographic Analysis

**Table S1.** Crystal data and structure refinement for hoop  $\Phi_{18}$  from 1,2-dichloroethane/methanol.

Data deposition	CCDC 1864540
Empirical formula	C <sub>180</sub> H <sub>210</sub> Cl <sub>24</sub>
Formula weight	3224.27
Temperature	100(2) K
Wavelength	0.85000 Å
Crystal system	Monoclinic
Space group	$P2_1/m$
Unit cell dimensions	$a = 18.830(4)$ Å $\alpha = 90^\circ$ $b = 32.960(7)$ Å $\beta = 119.64(3)^\circ$ $c = 18.840(4)$ Å $\gamma = 90^\circ$
Volume	10163(4) Å <sup>3</sup>
Z	2
Density (calculated)	1.054 g/cm <sup>3</sup>
Absorption coefficient	0.593 mm <sup>-1</sup>
$F(000)$	3396
Crystal size	0.10 × 0.03 × 0.03 mm <sup>3</sup>
Theta range for data collection	0.739 to 30.799°
Limiting indices	$-22 \leq h \leq 22$ , $-39 \leq k \leq 39$ , $-22 \leq l \leq 22$
Reflections collected	160768
Independent reflections	18893 [ $R(\text{int}) = 0.0381$ ]
Completeness to theta = 30.799°	99.6%
Absorption correction	multi-scan
Refinement method	Full-matrix least-squares on $F^2$
Data / restraints / parameters	18893 / 1279 / 1704
Goodness-of-fit on $F^2$	1.898
Final R indices [ $I > 2\sigma(I)$ ]	$R_1 = 0.1387$ , $wR_2 = 0.3864$
R indices (all data)	$R_1 = 0.1496$ , $wR_2 = 0.4040$
Extinction coefficient	n/a
Largest diff. peak and hole	0.688 and $-0.633$ e•Å <sup>-3</sup>

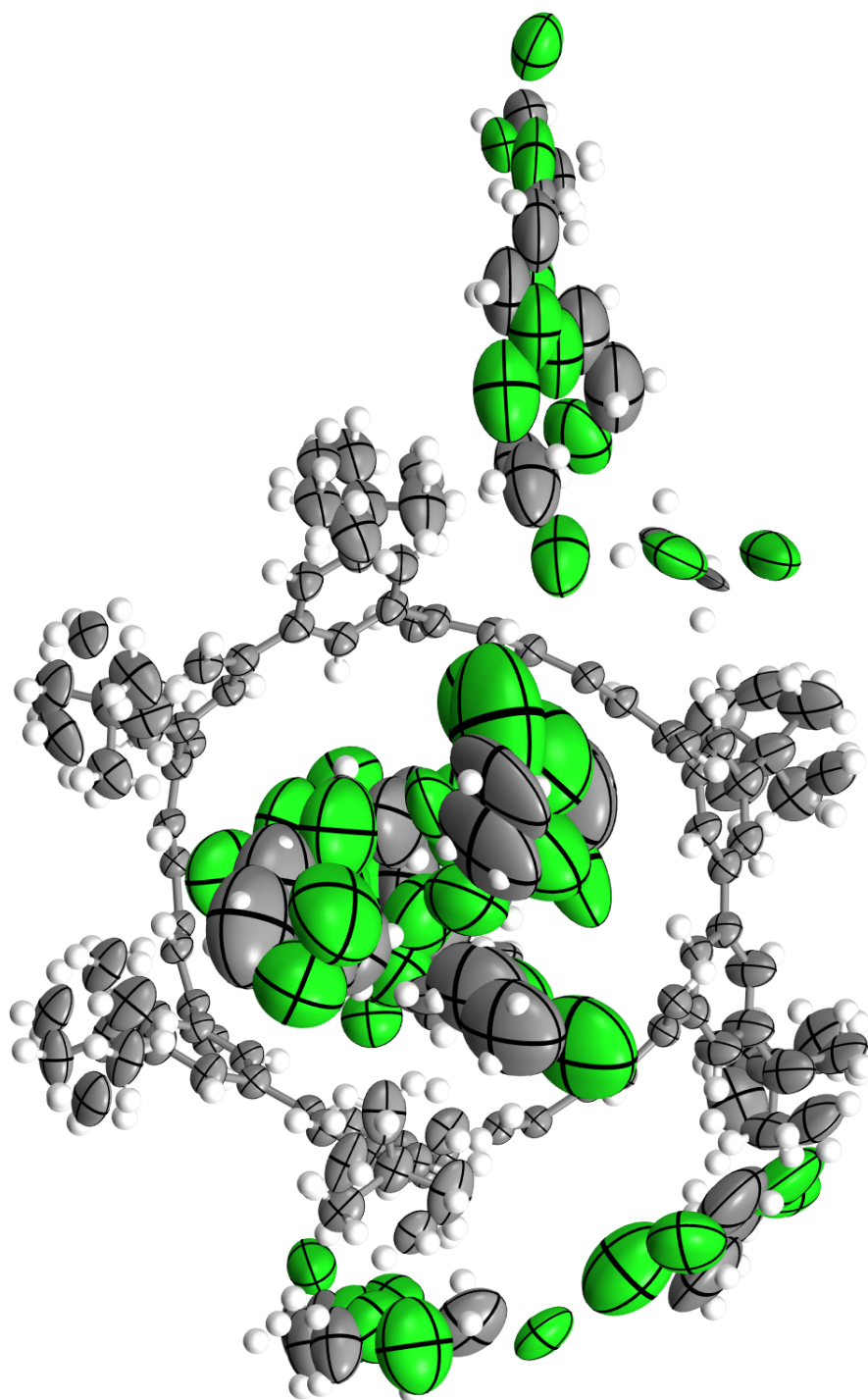


**Figure S15.** Crystal structure of hoop  $\Phi_{18}$ . ORTEP diagram of an asymmetric unit (50% probability level).

**Table S2.** Crystal data and structure refinement for hoop  $\Phi_{18}$  from 1,2-dichloroethane/methanol with squeeze process.

Data deposition	CCDC 1864541
Empirical formula	C <sub>156</sub> H <sub>162</sub>
Formula weight	2036.85
Temperature	100(2) K
Wavelength	0.85000 Å
Crystal system	Monoclinic
Space group	<i>P</i> 2 <sub>1</sub> / <i>m</i>
Unit cell dimensions	$a = 18.830(4)$ Å $\alpha = 90^\circ$ $b = 32.960(7)$ Å $\beta = 119.64(3)^\circ$ $c = 18.840(4)$ Å $\gamma = 90^\circ$
Volume	10163(4) Å <sup>3</sup>
Z	2
Density (calculated)	0.666 g/cm <sup>3</sup>
Absorption coefficient	0.054 mm <sup>-1</sup>
<i>F</i> (000)	2196
Crystal size	0.10 × 0.03 × 0.03 mm <sup>3</sup>
Theta range for data collection	0.739 to 30.799°
Limiting indices	−22 ≤ <i>h</i> ≤ 22, −39 ≤ <i>k</i> ≤ 39, −22 ≤ <i>l</i> ≤ 22
Reflections collected	160774
Independent reflections	18899 [ <i>R</i> (int) = 0.0381]
Completeness to theta = 30.799°	99.7%
Absorption correction	multi-scan
Refinement method	Full-matrix least-squares on <i>F</i> <sup>2</sup>
Data / restraints / parameters	18899 / 254 / 929
Goodness-of-fit on <i>F</i> <sup>2</sup>	1.537
Final R indices [ <i>I</i> > 2σ( <i>I</i> )]	<i>R</i> <sub>1</sub> = 0.0931, <i>wR</i> <sub>2</sub> = 0.3243
R indices (all data)	<i>R</i> <sub>1</sub> = 0.1069, <i>wR</i> <sub>2</sub> = 0.3390
Extinction coefficient	n/a
Largest diff. peak and hole	0.518 and −0.505 e <sup>−</sup> Å <sup>−3</sup>

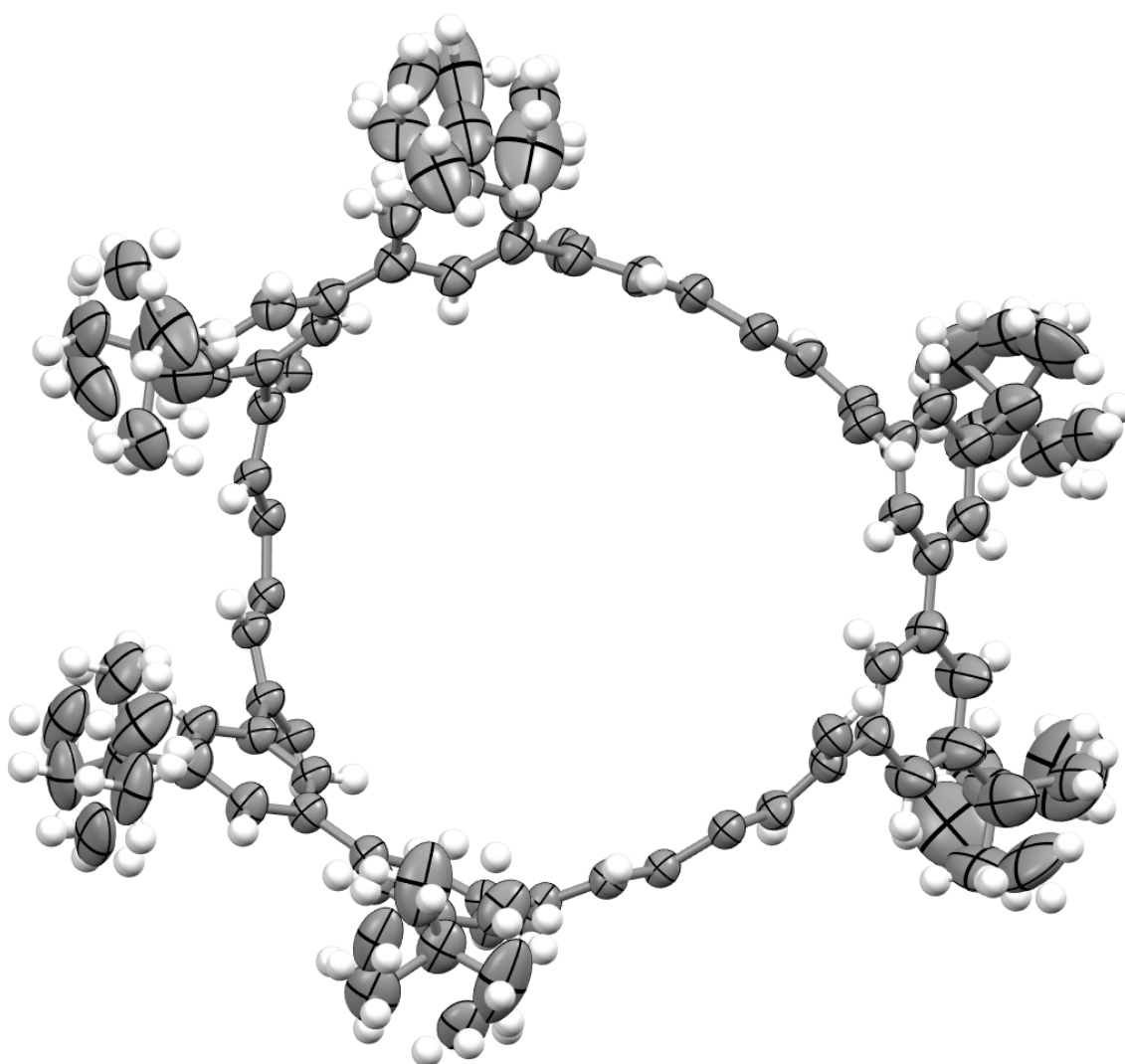


**Figure S16.** Crystal structure of hoop  $\Phi_{18}$  with the squeeze process. ORTEP diagram of an asymmetric unit (50% probability level).

**Table S3.** Crystal data and structure refinement for hoop  $\Phi_{24}$  from  $\text{CHCl}_3/2$ -propanol.

Data deposition	CCDC 1864542
Empirical formula	$\text{C}_{218}\text{H}_{226}\text{Cl}_{30}$
Formula weight	3909.47
Temperature	100(2) K
Wavelength	0.90000 Å
Crystal system	Orthorhombic
Space group	<i>Ccca</i>
Unit cell dimensions	$a = 30.560(6)$ Å $\alpha = 90^\circ$ $b = 35.210(7)$ Å $\beta = 90^\circ$ $c = 22.180(4)$ Å $\gamma = 90^\circ$
Volume	23866(8) Å <sup>3</sup>
Z	4
Density (calculated)	1.088 g/cm <sup>3</sup>
Absorption coefficient	0.739 mm <sup>-1</sup>
<i>F</i> (000)	8176
Crystal size	0.15 × 0.12 × 0.01 mm <sup>3</sup>
Theta range for data collection	2.519 to 30.001°
Limiting indices	$-33 \leq h \leq 33$ , $-36 \leq k \leq 36$ , $-24 \leq l \leq 24$
Reflections collected	8206
Independent reflections	6767 [ <i>R</i> (int) = 0.0593]
Completeness to theta = 30.001°	95.7%
Absorption correction	multi-scan
Refinement method	Full-matrix least-squares on <i>F</i> <sup>2</sup>
Data / restraints / parameters	8206 / 534 / 705
Goodness-of-fit on <i>F</i> <sup>2</sup>	1.896
Final R indices [ <i>I</i> > 2σ( <i>I</i> )]	<i>R</i> <sub>1</sub> = 0.1405, <i>wR</i> <sub>2</sub> = 0.4142
R indices (all data)	<i>R</i> <sub>1</sub> = 0.1527, <i>wR</i> <sub>2</sub> = 0.4283
Extinction coefficient	n/a
Largest diff. peak and hole	0.531 and -0.481 e <sup>+</sup> Å <sup>-3</sup>



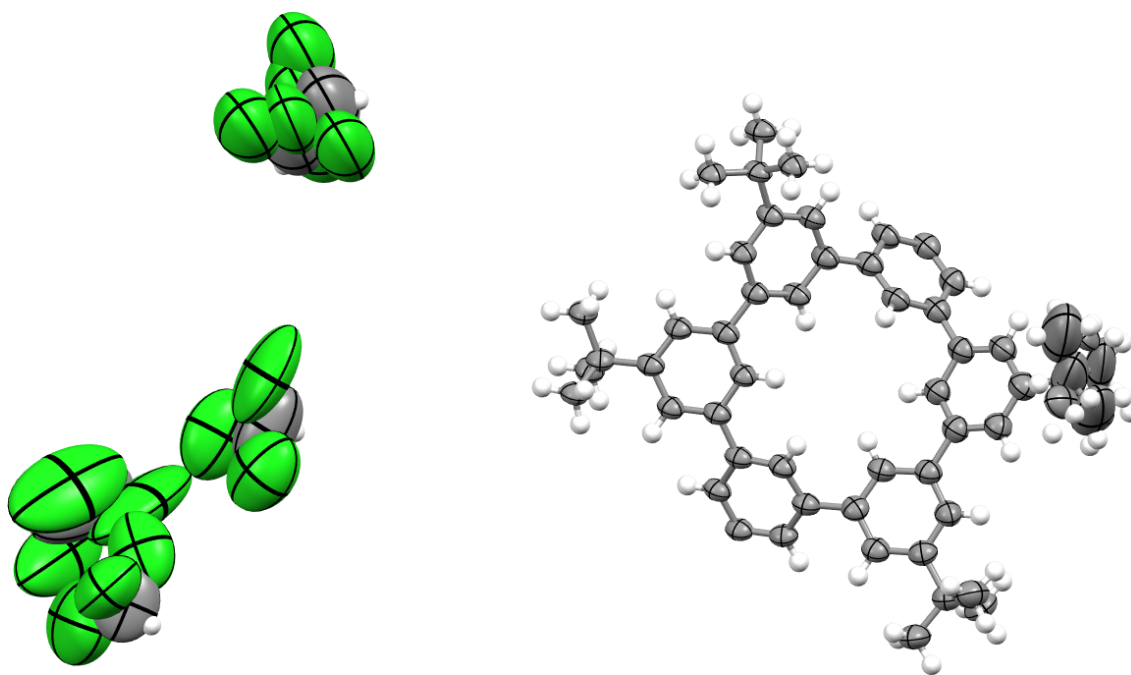


**Figure S17.** Crystal structure of hoop  $\Phi_{24}$ . ORTEP diagram of an asymmetric unit (50% probability level).

**Table S4.** Crystal data and structure refinement for hoop  $\Phi_{24}$  from  $\text{CHCl}_3/2$ -propanol with squeeze process.

Data deposition	CCDC 1864543
Empirical formula	$\text{C}_{208}\text{H}_{216}$
Formula weight	2715.80
Temperature	100(2) K
Wavelength	0.90000 Å
Crystal system	Orthorhombic
Space group	<i>Ccca</i>
Unit cell dimensions	$a = 30.560(6)$ Å $\alpha = 90^\circ$ $b = 35.210(7)$ Å $\beta = 90^\circ$ $c = 22.180(4)$ Å $\gamma = 90^\circ$
Volume	23866(8) Å <sup>3</sup>
Z	4
Density (calculated)	0.756 g/cm <sup>3</sup>
Absorption coefficient	0.070 mm <sup>-1</sup>
<i>F</i> (000)	5856
Crystal size	0.15 × 0.12 × 0.01 mm <sup>3</sup>
Theta range for data collection	1.465 to 30.001°
Limiting indices	−33 ≤ <i>h</i> ≤ 33, −36 ≤ <i>k</i> ≤ 36, −24 ≤ <i>l</i> ≤ 24
Reflections collected	8211
Independent reflections	6772 [ <i>R</i> (int) = 0.0592]
Completeness to theta = 30.001°	95.7%
Absorption correction	multi-scan
Refinement method	Full-matrix least-squares on <i>F</i> <sup>2</sup>
Data / restraints / parameters	8211 / 357 / 524
Goodness-of-fit on <i>F</i> <sup>2</sup>	1.026
Final R indices [ <i>I</i> > 2σ( <i>I</i> )]	<i>R</i> <sub>1</sub> = 0.0893, <i>wR</i> <sub>2</sub> = 0.2758
R indices (all data)	<i>R</i> <sub>1</sub> = 0.0982, <i>wR</i> <sub>2</sub> = 0.2870
Extinction coefficient	n/a
Largest diff. peak and hole	0.279 and −0.215 e <sup>−</sup> Å <sup>−3</sup>

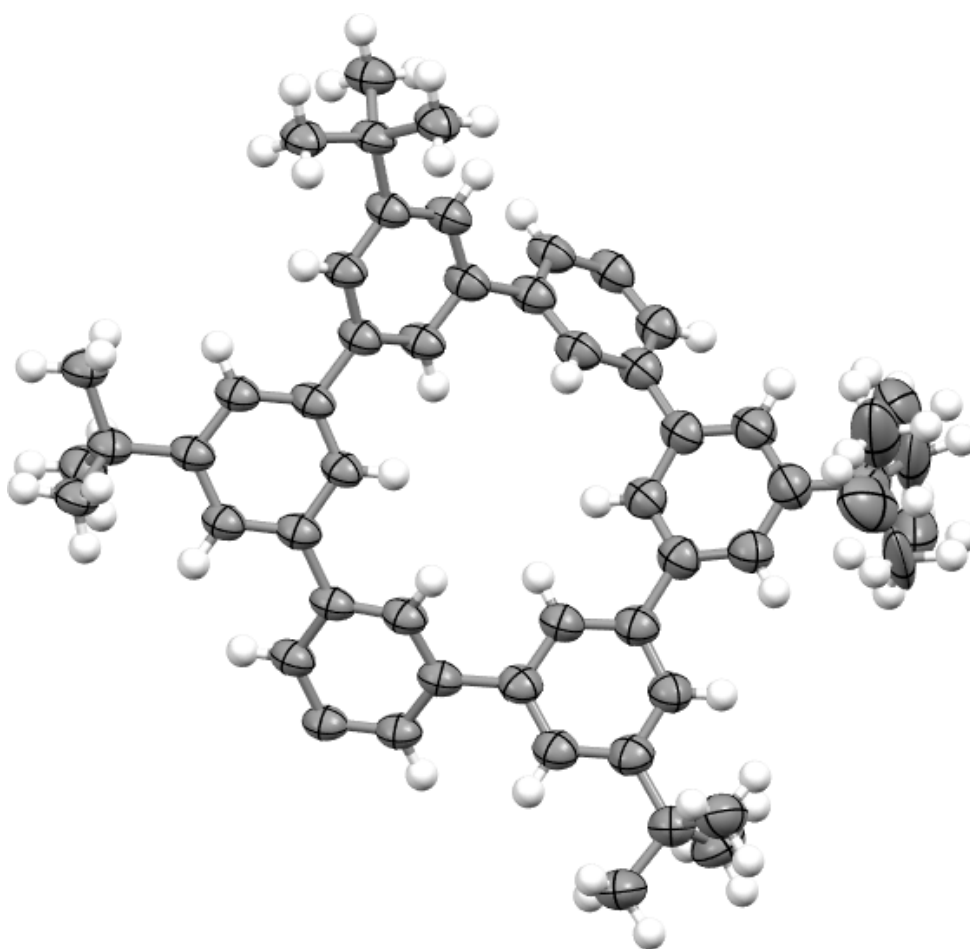


**Figure S18.** Crystal structure of hoop  $\Phi_{24}$  with the squeeze process. ORTEP diagram of an asymmetric unit (50% probability level).

**Table S5.** Crystal data and structure refinement for hoop  $\Phi_{30}$  from  $\text{CHCl}_3$ /methanol with squeeze process.

Data deposition	CCDC 1864544
Empirical formula	$\text{C}_{260}\text{H}_{270}$
Formula weight	3394.74
Temperature	95(2) K
Wavelength	0.75000 Å
Crystal system	Monoclinic
Space group	$P2_1$
Unit cell dimensions	$a = 16.570(3)$ Å $\alpha = 90^\circ$ $b = 42.930(9)$ Å $\beta = 96.72(3)^\circ$ $c = 57.470(12)$ Å $\gamma = 90^\circ$
Volume	40600(14) Å <sup>3</sup>
Z	4
Density (calculated)	0.555 g/cm <sup>3</sup>
Absorption coefficient	0.031 mm <sup>-1</sup>
$F(000)$	7320
Crystal size	0.22 × 0.08 × 0.04 mm <sup>3</sup>
Theta range for data collection	0.753 to 23.240°
Limiting indices	$-17 \leq h \leq 17$ , $-44 \leq k \leq 44$ , $-60 \leq l \leq 60$
Reflections collected	98006
Independent reflections	51504 [ $R(\text{int}) = 0.0672$ ]
Completeness to $\theta = 23.240^\circ$	99.4%
Absorption correction	multi-scan
Refinement method	Full-matrix least-squares on $F^2$
Data / restraints / parameters	98006 / 3911 / 5319
Goodness-of-fit on $F^2$	0.968
Final R indices [ $I > 2\sigma(I)$ ]	$R_1 = 0.0927$ , $wR_2 = 0.2568$
R indices (all data)	$R_1 = 0.1421$ , $wR_2 = 0.3055$
Extinction coefficient	n/a
Largest diff. peak and hole	0.242 and $-0.357 \text{ e} \cdot \text{Å}^{-3}$

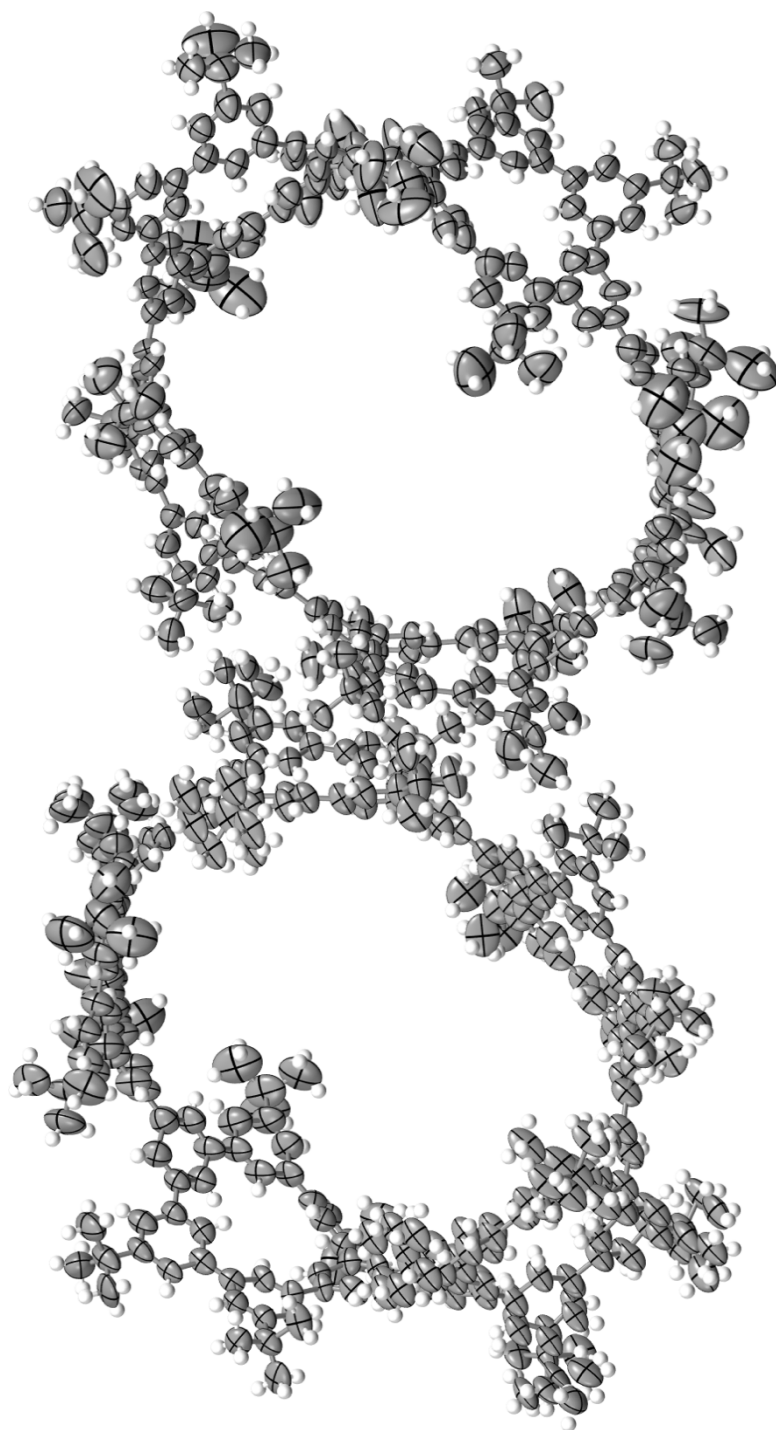


**Figure S19.** Crystal structure of hoop  $\Phi_{30}$  with the squeeze process. ORTEP diagram of an asymmetric unit (50% probability level).

**Table S6.** Crystal data and structure refinement for the complex of hoop  $\Phi_{24}$  with  $C_{70}$  from chlorobenzene/2-propanol

Data deposition	CCDC 1872559
Empirical formula	$C_{460}H_{251}Cl_7$
Formula weight	6025.76
Temperature	100(2) K
Wavelength	0.85000 Å
Crystal system	Triclinic
Space group	$P\bar{1}$
Unit cell dimensions	$a = 19.820(4)$ Å $\alpha = 81.65(3)^\circ$ $b = 20.510(4)$ Å $\beta = 78.06(3)^\circ$ $c = 38.690(8)$ Å $\gamma = 77.99(3)^\circ$
Volume	14965(6) Å <sup>3</sup>
Z	2
Density (calculated)	1.337 g/cm <sup>3</sup>
Absorption coefficient	0.211 mm <sup>-1</sup>
$F(000)$	6260
Crystal size	0.10 × 0.03 × 0.03 mm <sup>3</sup>
Theta range for data collection	1.221 to 26.575°
Limiting indices	$-20 \leq h \leq 20$ , $-21 \leq k \leq 21$ , $-40 \leq l \leq 40$
Reflections collected	35805
Independent reflections	23332 [ $R(\text{int}) = 0.0906$ ]
Completeness to $\theta = 26.575^\circ$	97.9%
Absorption correction	multi-scan
Refinement method	Full-matrix least-squares on $F^2$
Data / restraints / parameters	35805 / 13813 / 5189
Goodness-of-fit on $F^2$	1.621
Final R indices [ $I > 2\sigma(I)$ ]	$R_1 = 0.1330$ , $wR_2 = 0.3685$
R indices (all data)	$R_1 = 0.1772$ , $wR_2 = 0.4073$
Extinction coefficient	n/a
Largest diff. peak and hole	1.140 and $-1.087$ e•Å <sup>-3</sup>

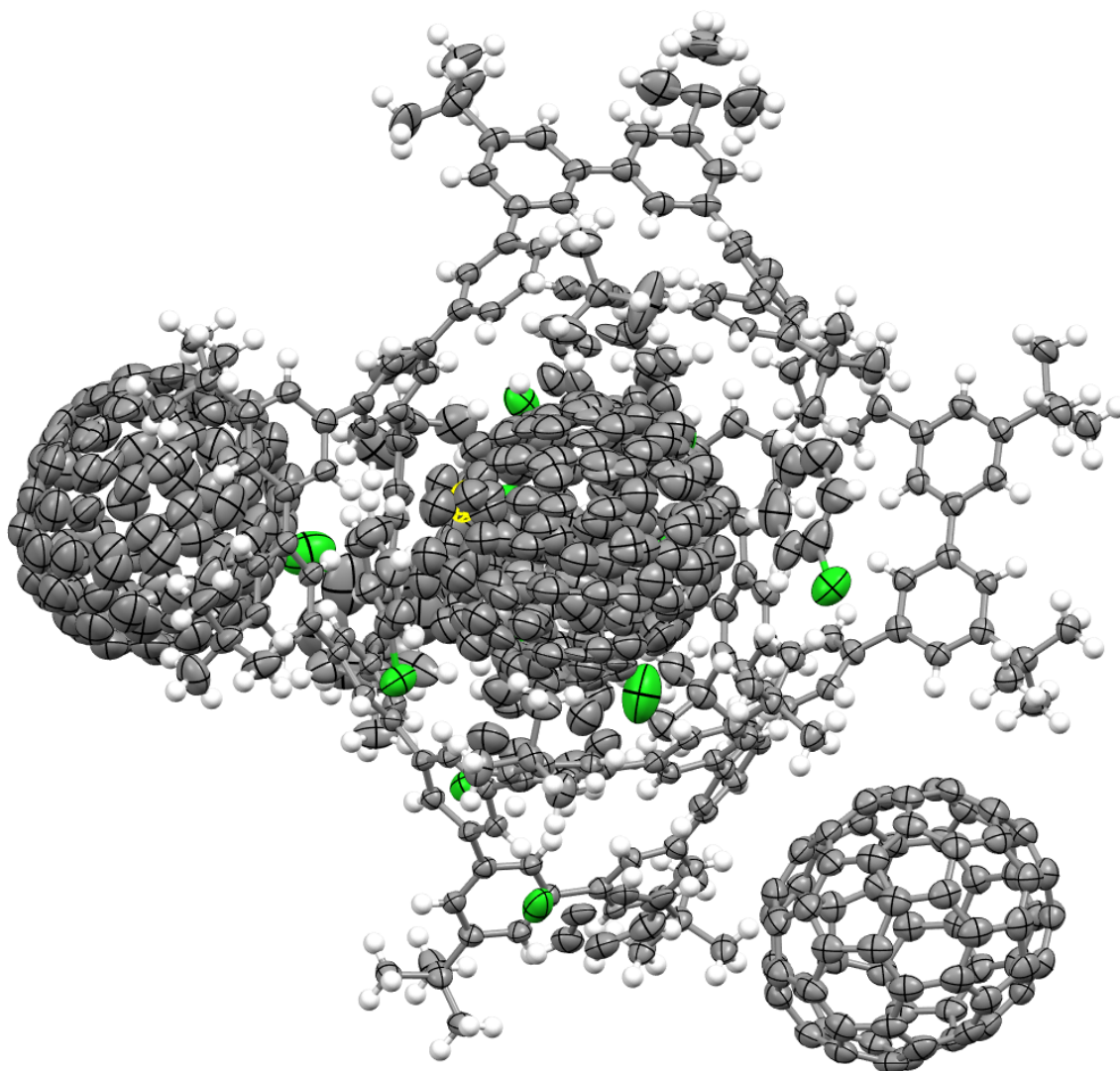


**Figure S20.** Crystal structure of the complex of hoop  $\Phi_{24}$  with  $C_{70}$ . ORTEP diagram of an asymmetric unit (50% probability level).

## 2.10 References

1. R. Jasti, J. Bhattacharjee, J. B. Neaton, C. R. Bertozzi, *J. Am. Chem. Soc.* **2008**, *130*, 17646-17647.
2. H. Takaba, H. Omachi, Y. Yamamoto, J. Bouffard, K. Itami, *Angew. Chem. Int. Ed.* **2009**, *48*, 6112-6116.
3. S. Yamago, Y. Watanabe, T. Iwamoto, *Angew. Chem. Int. Ed.* **2010**, *49*, 757-759.
4. P. J. Evans, E. R. Darzi, R. Jasti, *Nat. Chem.* **2014**, *6*, 404-408.
5. R. Saito, G. Dresselhaus, M. S. Dresselhaus. *Physical Properties of Carbon Nanotubes*; Imperial College Press: London, 1998.
6. Z. Sun, K. Ikemoto, T. M. Fukunaga, T. Koretsune, R. Arita, S. Sato, H. Isobe. *Science*, **2019**, *363*, 151-155.
7. The hoop size of hoop  $\Phi_{6n}$  is identical to that of  $[3n]$ CPP.
8. N. Miyaura, A. Suzuki. *Chem. Rev.* **1995**, *95*, 2457-2483.
9. A. Yoshii, K. Ikemoto, T. Izumi, H. Kita, H. Taka, S. Sato, H. Isobe. *ECS J. Solid State Sci. Technol.* **2017**, *6*, M3065-M3067.
10. T. Ishiyama, J. Takagi, K. Ishida, N. Miyaura, N. R. Anastasi, J. F. Hartwig. *J. Am. Chem. Soc.* **2002**, *124*, 390-391.
11. S. Hitosugi, S. Sato, T. Matsuno, T. Koretsune, R. Arita, H. Isobe. *Angew. Chem., Int. Ed.* **2017**, *56*, 9106-9110.
12. (a) P. J. Evans, E. R. Darzi, R. Jasti. *Nat. Chem.* **2014**, *6*, 404-408. (b) E. Kayahara, V. K. Patel, S. Yamago. *J. Am. Chem. Soc.* **2014**, *136*, 2284-2287.
13. (a) R. Jasti, J. Bhattacharjee, J. B. Neaton, C. R. Bertozzi. *J. Am. Chem. Soc.* **2008**, *130*, 17646-17647. (b) T. Iwamoto, Y. Watanabe, Y. Sakamoto, T. Suzuki, S. Yamago. *J. Am. Chem. Soc.* **2011**, *133*, 8354-8361. (c) Y. Segawa, A. Fukazawa, S. Matsuura, H. Omachi, S. Yamaguchi, S. Irle, K. Itami. *Org. Biomol. Chem.* **2012**, *10*, 5979-5984.
14. Z. Sun, N. Miyamoto, S. Sato, H. Tokuyama, H. Isobe. *Chem. Asian J.* **2017**, *12*, 271-275.
15. (a) C. Camacho, T. A. Niehaus, K. Itami, S. Irle. *Chem. Sci.* **2013**, *4*, 187-195. (b) M. Fujitsuka, D. W. Cho, T. Iwamoto, S. Yamago, T. Majima. *Phys. Chem. Chem. Phys.* **2012**, *14*, 14585-14588. (c) Y. Noguchi, O. Sugino. *J. Chem. Phys.* **2017**, *146*, 144304.
- <sup>16</sup> Z. Sun, T. Matsuno, H. Isobe. *Bull. Chem. Soc. Jpn.* **2018**, *91*, 907-921.



17. T. Matsuno, H. Naito, S. Hitosugi, S. Sato, M. Kotani, H. Isobe. *Pure Appl. Chem.* **2014**, *86*, 489-495.
18. This downfield-shift tendency was similar to those observed with [n]CPP with  $n = 8$ -12. See refs. 12 and 13.
19. T. A. Halgren. Merck molecular force field. *J. Comput. Chem.* **1996**, *17*, 490-519.
20. I. Kolossváry, W. C. Guida. *J. Am. Chem. Soc.* **1996**, *118*, 5011-5019.
21. Considering the rigid cylindrical structure of hoop  $\Phi_{18}$ , we may apply vector descriptions of (9,9)-carbon nanotube to this molecule: length index ( $t_r$ ) = 4.0, bond-filling index ( $F_b$ ) = 57% and atom-filling index ( $F_a$ ) = 67% (ref. 17).
22. G. Povie, Y. Segawa, T. Nishihara, Y. Miyauchi, K. Itami. *Science* **2017**, *356*, 172-175.
23. Z. Sun, T. Suenaga, P. Sarkar, S. Sato, M. Kotani, H. Isobe. *Proc. Natl. Acad. Sci. U.S.A.* **2016**, *113*, 8109-8114.
24. M. J. Turner, J. J. McKinnon, D. Jayatilaka, M. A. Spackman. *CrystEngComm* **2011**, *13*, 1804-1813.
25. The diameters of hoop  $\Phi_{6n}$  are identical to those of [9]-, [12]- and [15]CPP.
26. (a) T. Iwamoto, Y. Watanabe, T. Sadahiro, T. Haino, S. Yamago. *Angew. Chem., Int. Ed.* **2011**, *50*, 8342-8344. (b) T. Iwamoto, Y. Watanabe, H. Takaya, T. Haino, N. Yasuda, S. Yamago. *Chem. Eur. J.* **2013**, *19*, 14061-14068. (c) Y. Nakanishi, H. Omachi, S. Matsuura, Y. Miyata, R. Kitaura, Y. Segawa, K. Itami, H. Shinohara. *Angew. Chem., Int. Ed.* **2014**, *53*, 3102-3106.
27. T. Matsuno, S. Sato, H. Isobe. Curved  $\pi$ -Receptors. In *Comprehensive Supramolecular Chemistry II*; Atwood, J. L., Ed.; Elsevier: Oxford, **2017**, pp 311-328.
28. (a) K. Ikemoto, R. Kobayashi, S. Sato, H. Isobe. *Angew. Chem., Int. Ed.* **2017**, *56*, 6511-6514. (b) K. Ikemoto, R. Kobayashi, S. Sato, H. Isobe. *Org. Lett.* **2017**, *19*, 2362-2365.
29. T. Matsuno, M. Fujita, K. Fukunaga, S. Sato, H. Isobe. *Nat. Commun.* **2018**, *9*, 3779.
30. F. S. Han, M. Higuchi, D. G. Kurth. *Org. Lett.* **2007**, *9*, 559-562.
31. P. Thordarson. *Chem. Soc. Rev.* **2011**, *40*, 1305-1323.
32. W. Kabsch. *J. Appl. Cryst.* **1993**, *26*, 795-800.
33. G. M. Sheldrick. *Acta Crystallogr. A* **2015**, *71*, 3-8.

- 34. G. M. Sheldrick. *Acta Crystallogr. A* **2008**, *64*, 112-122.
- 35. C. Kabuto, S. Akine, T. Nemoto, E. Kwon. Release of software (Yadokari-XG 2009) for crystal structure analyses. *J. Cryst. Soc. Jpn.* **2009**, *51*, 218-224.
- 36. A. L. Spek. *J. Appl. Cryst.* **2003**, *36*, 7-13.
- 37. P. van der Sluis, A. L. Spek. *Acta Crystallogr A* **1990**, *46*, 194-201.

## Chapter 3. Hemispherical Phenine Nanocarbon

### 3.1 Introduction

Combinations of polygons of  $sp^2$ -carbons result in carbon-rich molecules, so-called geodesic polyarenes.<sup>1,2</sup> Their unique shapes and properties have currently been exploited, and their intimate relevance to nanocarbons such as fullerene and carbon nanotubes further stimulated bottom-up chemical syntheses of various congeners. Segments of fullerenes, for instance, have been synthesized by a combination of hexagons and pentagons to afford curved  $\pi$ -rich molecules such as corannulene<sup>3</sup> and a  $C_{30}H_{12}$  bisection (**A**)<sup>4,5,6,7</sup> (Figure 1). However, the synthesis of geodesic polyarenes requires elaborations of synthetic routes unique to each target (see Chapter 1), which slows an expansion of the structural library of congeners. Recently, we introduced a design concept of phenine nanocarbons to explore large geodesic structures via concise and versatile synthesis.<sup>8</sup> By adopting planar trigonal panels of phenine as the basic unit to form polygons,<sup>9</sup> synthetic assembly of the multiple panels via biaryl coupling reactions becomes accessible. Combinations of phenine polygons were originally made possible by devising a synthetic strategy to decorate an omphalos polygon with terphenyl rims that were eventually closed to form outer polygons at the periphery (Figure 1). With this synthetic strategy, we previously synthesized a GPF bowl ( $C_{160}H_{150}$ ) and a GPF saddle ( $C_{224}H_{210}$ ) that possess isorecticular networks of corannulene ( $C_{20}H_{10}$ )<sup>3</sup> and [7]circulene ( $C_{28}H_{14}$ )<sup>[10]</sup> in a much larger dimension (Figure 1).<sup>[8]</sup> This terphenyl decoration strategy, however, requires radiated expansions of periphery, which increases numbers of bond formations upon expansion of the GPF networks. For instance, the final periphery-forming reactions took place 5 times for the GPF bowl, which increased to 7 times for the GPF saddle. The increase in the bond formation inevitably resulted in lower yields despite the same order of bond-forming efficiency. To eliminate such deficiency in the synthetic scope of GPFs, we herein devise a polygon assembling strategy for the synthesis of larger GPFs (Figure 1). In place of the terphenyl rims, preformed polygons were assembled on the omphalos, which enable us to reduce the bonds to be formed at the final step. As a target for the first demonstration of this synthetic strategy, we designed a GPF hemisphere (**1**). An isorecticular polyarene, *i.e.*, a hemispherical  $C_{30}H_{10}$  bisection of [60]fullerene (**B**), has been conceived as a synthetic precursor of  $C_{60}$ ,<sup>[4,6,7]</sup> but its synthesis has not been achieved.

Albeit simple, the polygon assembling strategy allowed for the synthesis of a large hemispherical hydrocarbon of  $C_{220}H_{180}$ . Detailed structures were investigated by crystallography and spectroscopy with an aid of theoretical calculations to reveal important structural elements to control the shape of the nanometer-sized GPFs.

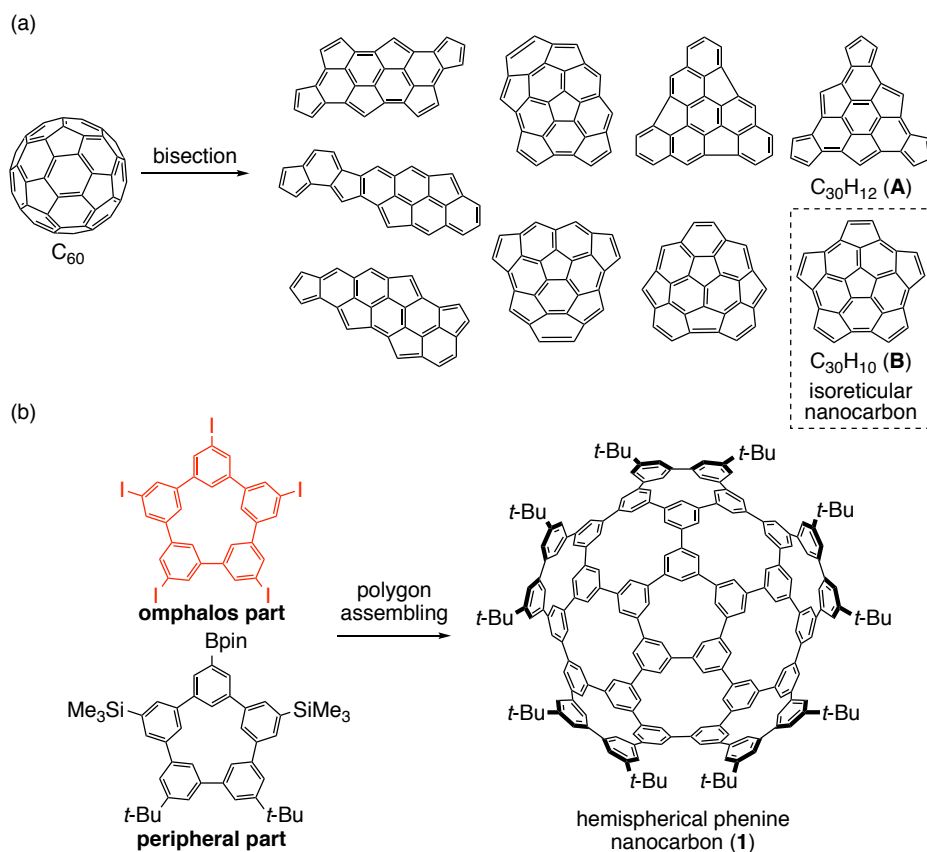
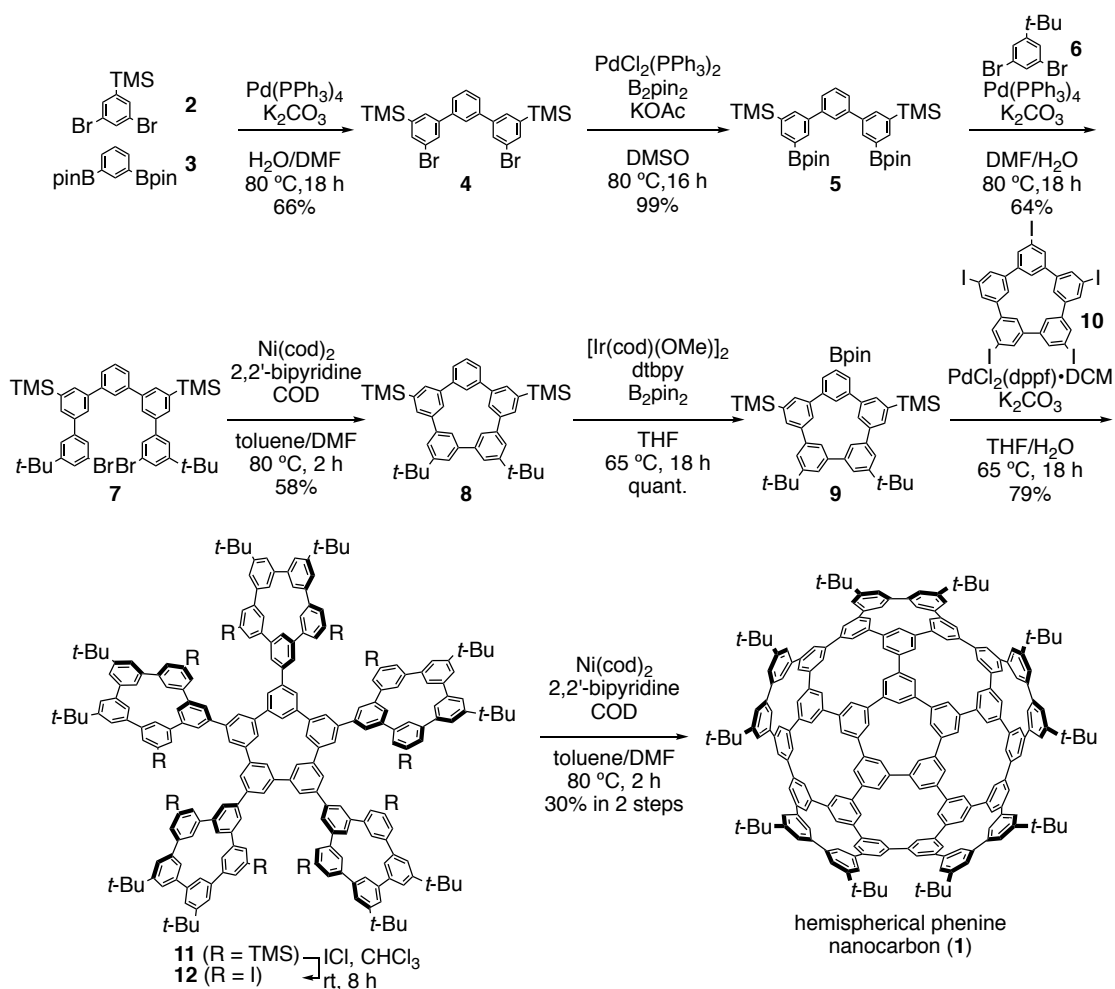


**Figure 1.** (a) Possible bisections of buckminsterfullerene (see ref. 6). (b) Polygon assembling strategy applied to the hemispherical phenine nanocarbon **1**.

### 3.2 Synthesis

A unique mechanism, called the pentagon road, has been proposed to be an energetically favorable path of fullerene formations,<sup>11</sup> and we coincidentally followed this pentagon road for the synthesis of **1**. A 5-step synthesis was first devised for a pentagonal [5]cyclo-*meta*-phenylene ([5]CMP) unit to be installed as the periphery unit (Scheme 1), as the periphery [5]CMP unit must be furnished with three different substituents. Thus, terphenyl **4** was synthesized by Suzuki-Miyaura coupling of **2** and **3**<sup>12</sup> and was further extended with two other phenyl groups to afford a linear pentameric molecule **7**.

Cyclization with Yamamoto-type coupling reaction completed the [5]CMP skeleton (**8**), and a boryl group was installed for subsequent Suzuki-Miyaura coupling with another [5]CMP unit at the omphalos. The [5]CMP omphalos (**10**) with five iodine substituents was separately prepared by the one-pot macrocyclization synthesis.<sup>13</sup> Six [5]CMP units, *i.e.*, five at the periphery (**9**) and one at the omphalos (**10**) were then assembled by five-fold Suzuki-Miyaura coupling reactions to afford a starfish-shaped molecule (**11**). We converted 10 TMS groups of **11** into 10 iodine substituents for the final cyclization and, finally, performed Yamamoto-type cyclization to furnish 5 additional hexagon units to complete the hemisphere **1**.<sup>14</sup> Owing to the polygon assembling strategy with preformed pentagons, the final Yamamoto cyclization required 5 biaryl bonds to be completed, which resulted in moderate yield of 30% for the final two steps (efficiency = 79%/bond). The synthesis stitched 40 biaryl bonds among 30 phenine units in total, which were larger than those of bowl-shaped GPF (25 biaryl bonds/ 20 phenine units). The longest linear route to **1** counted 8 steps from **2/3**, which recorded an overall yield of 5.7%.



**Scheme 1.** Synthesis of the hemispherical phenine nanocarbon.

### 3.3 Spectroscopic properties

The target was first characterized by spectroscopy (Figure 2). The NMR spectra thus indicated the presence of a highly symmetric structure. Originating from 90 aromatic hydrogen atoms, only 9 aromatic resonances appeared in the  $^1\text{H}$  NMR spectrum, and an overlap of two aromatic  $^1\text{H}$  resonances was confirmed by the observation of 10 aromatic CH resonances in the DEPT135 spectrum. The MALDI-TOF-MS spectrum confirmed the chemical composition of  $\text{C}_{220}\text{H}_{180}$  with  $m/z = 2821$  ( $[\text{M}]^+$ ).

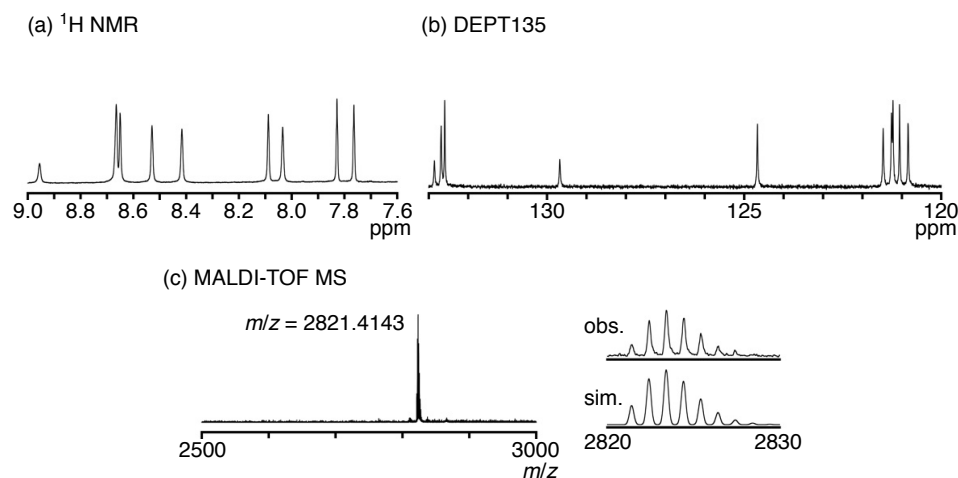


**Figure 2.** The aromatic regions of (a)  $^1\text{H}$  NMR and (b) DEPT135 spectra and (c) MALDI-TOF mass spectrum of the hemispherical phenine nanocarbon **1**.

### 3.4 Crystal structures

Atomic-level molecular structures of **1** were fully established by X-ray crystallographic analysis. A single crystal was obtained from a solution in chlorobenzene in the presence of propan-2-ol vapor at 25 °C. The crystal was subjected to the diffraction analysis with a synchrotron X-ray source at the PF BL17A beamline in the KEK Photon Factory. After the structural refinements, two independent structures of **1** were located, and for both of them, the molecular shape was severely deformed (Figure 3). Thus, unlike the preceding phenine nanocarbons,<sup>8</sup> the present geodesic structure considerably deviated from an ideal, hemispherical shape that was expected from the combination of pentagons and hexagons.<sup>15</sup> The crystal structures were further analyzed with the  $\pi$ -orbital axis vector (POAV) as references.<sup>16, 17</sup> Thus, curved shapes of geodesic polyarenes intrinsically originate from the POAV pyramidalization angles ( $\theta_P$ ), whereas the molecular shapes of the GPF hemisphere was mainly defined by POAV dihedral angles ( $\phi$ ). The uniqueness of such structural deformations was thoroughly investigated with an aid of theoretical calculations (see below). The crystallographic analysis revealed that the GPF hemisphere did not form stacking structures in the crystal, although the previous GPF bowl formed stacking assembly both in the crystal and the solution. A method for structural analysis more suitable for phenine nanocarbon molecules will be introduced in the next chapter.

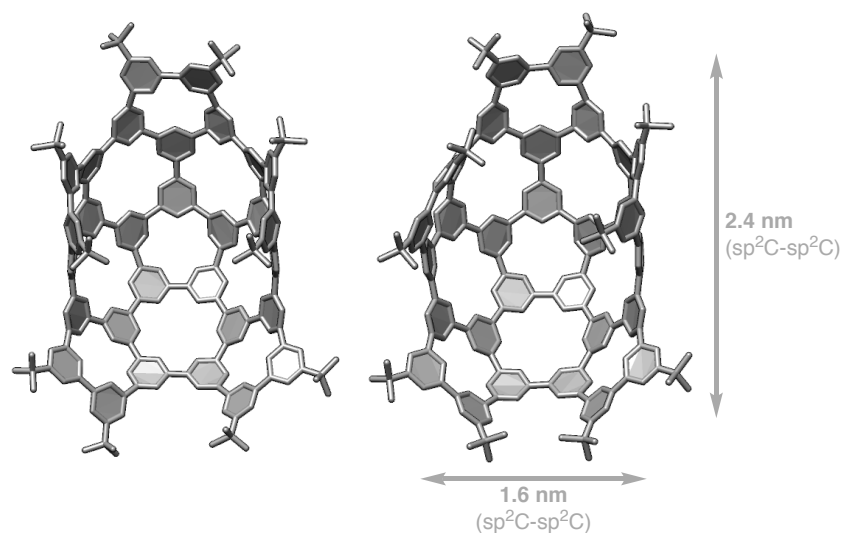


**Figure 3.** Two independent structures found in the crystal of **1**. Minor disordered conformers, solvent molecules and hydrogen atoms are omitted for clarity.

### 3.5 Dynamic structure

The spectroscopically observed structure in solution was correlated with the crystal structure with an aid of theoretical calculations via in-depth analyses of the POAV angles. The solution-phase NMR spectra of **1** showed only 10 aromatic CH resonances originating from 90 CH moieties of the molecule (Figure 2). The result demonstrated that the molecule spectroscopically possessed the  $C_{5v}$  symmetry, which, for instance, gave rise to one  $^1\text{H}$  resonance from 5 innermost hydrogen atoms. In contrast, the crystal structures possessed the  $C_1$  symmetry, which at a glance failed to explain the spectra. The origin of the high symmetry that was spectroscopically observed in the solution phase was thus investigated with an aid of semiempirical PM6 calculations. Thus, starting from the crystal structure as the initial structure, we replaced the *t*-Bu groups with hydrogen and located a structure with pseudo- $C_s$  symmetry by PM6 calculations.<sup>8,18</sup> As shown in Figure 4b, the pseudo- $C_s$  structure did not deviate much from the oval shape of the crystal structure. As this pseudo- $C_s$  structure still failed to explain the highly symmetric structure observed by NMR spectroscopy, dynamic conformational changes were further investigated by a torsional scan analysis with PM6 calculations.<sup>8</sup> When the torsion angles at innermost phenine linkages were scanned over  $5^\circ$  intervals, the molecular shape fluctuated (see Figure 5 in Chapter 4). The structural fluctuation accompanied minute energy changes, and the highest energy barrier was estimated to be  $0.12 \text{ kcal mol}^{-1}$ .

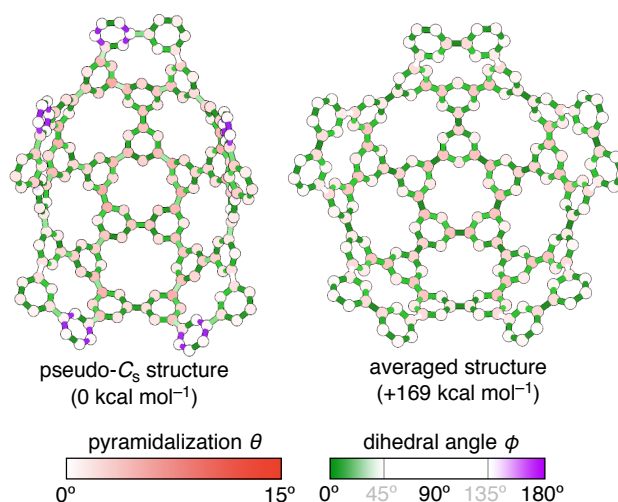


Figure 1 consists of two parts. Part (a) is a 3D model of a C<sub>60</sub>-like cage with a C<sub>2v</sub>-like symmetry axis. The cage is shown with a central cavity. The C<sub>2v</sub>-like axis is indicated by a dashed line. The angles between the C<sub>2v</sub>-like axis and the C-C bonds are labeled: -25°, 25°, 12°, -12°, and 0°. Part (b) is a plot of the energy difference  $\Delta E$  [kcal mol<sup>-1</sup>] versus the dihedral angles [°]. The plot shows five peaks corresponding to the angles in (a). The energy difference ranges from 0 to 0.12 kcal/mol.

### 3.6 Structural analyses

65

in solution. Thus, unlike the smaller GPF bowl that formed a dimer in solution,<sup>8</sup> the bowl-shaped, stacking-ready structure did not exist with **1** as actual species, which thereby hampered the stacking of **1** in solution. It is possible that the absence of the bow-in-bowl stacks would be beneficial for further reactions such as dimerization of **1**.<sup>4,5,6</sup>



**Figure 5.** POAV analyses of the pseudo- $C_s$  minimum-energy structure and the time-averaged structure.

### 3.7 Host–guest interaction

#### 第 7 節

本節については、5 年以内に雑誌等で刊行予定のため非公開。

#### 第7節

本節については，5年以内に雑誌等で刊行予定のため非公開．

## 第 7 節

本節については，5 年以内に雑誌等で刊行予定のため非公開．

### 3.8 Conclusion

A polygon assembling strategy for the synthesis of GPFs was devised and afforded a large, intrinsically hemispherical GPF composed of a 30 phenine panels. The synthesis successfully furnished a previous bowl-shaped GPF with 10 extra phenine bridges via a concise synthetic route. Although the spectroscopic analysis showed the presence of expected, highly symmetric hemispherical shape of the molecule, the crystallographic analysis unexpectedly revealed highly deformed, oval-shaped structures of the molecule. The discrepancy between the solution-phase structure and the crystal structure was resolved with the aid of the theoretical calculations, which indicated the presence of rapid structural fluctuations in solution. In-depth structural analysis was performed with POAV as the reference to reveal that the structural deformation was largely dictated by the POAV dihedral angles  $\phi$ . The deformed structure resided at the global minima, which hampered the stacking assembly of the molecules both in solution and in solid. Thus, this study should facilitate the development of GPF design by providing a novel synthetic strategy. We believe that, for instance, ball-shaped GPF molecules become a realistic synthetic target via the present groundwork.<sup>4,5,6,19</sup> The present results should also stimulate further interest in the dynamic structural behaviors, which, we believe, should lead to the development of GPF materials in future.

### 3.9 Supplementary data

#### General

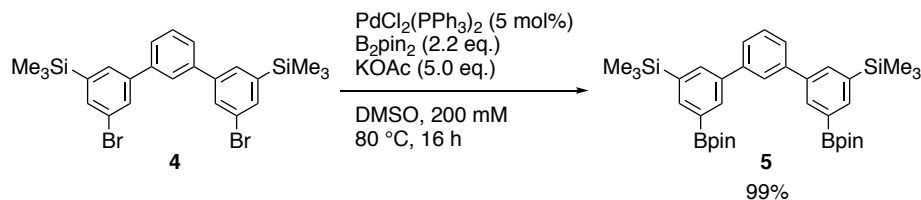
Flash column chromatography was performed on silica gel 60N (spherical and neutral gel, 40–50  $\mu\text{m}$ , Kanto). Gel permeation chromatography (GPC) was performed on JAI LC-9104 systems or on JASCO LC-2000Plus series under the conditions specified below. Analytical high-performance liquid chromatography (HPLC) for purity verifications was performed with two-types of columns (COSMOSIL BuckyPrep, 4.6 $\phi$   $\times$  250 mm and COSMOSIL  $\pi$ NAP, 4.6 $\phi$   $\times$  250 mm) in a column oven (40  $^{\circ}\text{C}$ ) at the flow rate of 1.0 mL/min with a UV detection (280 nm).  $^1\text{H}$  and  $^{13}\text{C}$  NMR spectra were recorded on a JEOL RESONANCE JNM-ECA II 600 equipped with an UltraCOOL probe. Chemical shift values are given with respect to internal  $\text{CHCl}_3$  for  $^1\text{H}$  NMR ( $\delta$  7.26) and  $\text{CDCl}_3$  for  $^{13}\text{C}$  NMR ( $\delta$  77.16). Data are reported as follows: chemical shift, multiplicity (s = singlet, d = doublet, t = triplet), coupling constant in hertz (Hz) and a relative integration value. High-resolution mass spectra were performed on a Bruker Daltonics autoflex speed using matrix assisted laser desorption ionization (MALDI) method with pyrene as a matrix (ionization mode: reflector positive) or on a Bruker micrOTOF II spectrometer equipped with an APCI probe equipped with a DirectProbe (DIP). Elemental analyses were performed on an ELEMENTAR vario MICRO cube (Elemental Analysis Center, Graduate School of Science, The University of Tokyo).

#### Materials

Anhydrous THF (stabilizer free), DMF and toluene were purified by a solvent purification system (GlassContour) equipped with columns of activated alumina and supported copper catalyst (Q-5).<sup>20</sup> Milli Q water was used for reactions and degassed prior to use. All other chemicals were of reagent grade and used without any further purification. Terphenyl **4** was prepared by a method reported in the literature.<sup>8</sup> All reactions were performed under  $\text{N}_2$  atmosphere.

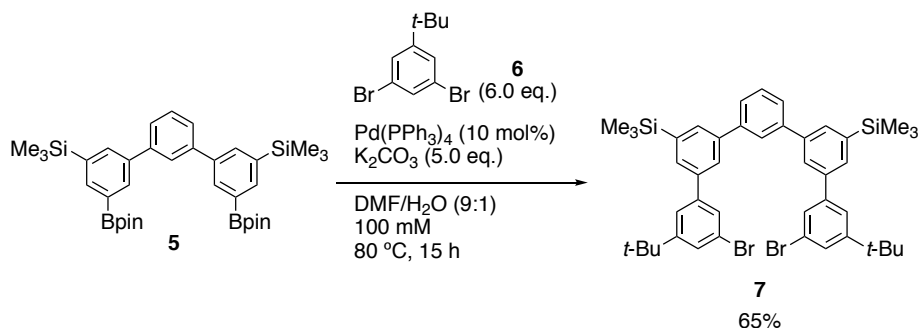
## Methods

### Diborylated terphenyl **5**



A mixture of terphenyl **4** (1.67 g, 3.13 mmol), bis(pinacolato)diboron (1.75 g, 6.90 mmol),  $\text{PdCl}_2(\text{PPh}_3)_2$  (110 mg, 0.157 mmol) and potassium acetate (1.54 g, 15.7 mmol) in DMSO (15.7 mL) was stirred at  $80^\circ\text{C}$  for 16 h. After the mixture was cooled to ambient temperature,  $\text{H}_2\text{O}$  (30 mL) was added. The resulting precipitate was collected and washed with  $\text{H}_2\text{O}$  (20 mL). The solid was dissolved with  $\text{AcOEt}$  (40 mL) and was filtrated. The filtrate was washed with brine (40 mL), dried over  $\text{Na}_2\text{SO}_4$  and concentrated in vacuo. The title compound was obtained as an off-white powder in 99% yield (1.95 g).  $^1\text{H}$  NMR (600 MHz,  $\text{CDCl}_3$ , 298 K):  $\delta$  8.07 (dd,  $J = 2.0$  Hz, 1.1 Hz, 2H), 7.96 (t,  $J = 1.1$  Hz, 2H), 7.85 (dd,  $J = 2.0$  Hz, 1.1 Hz, 2H), 7.81 (t,  $J = 1.8$  Hz, 1H), 7.58 (dd,  $J = 7.5$ , 1.8 Hz, 2H), 7.49 (t,  $J = 7.5$  Hz, 1H), 1.36 (s, 24H), 0.33 (s, 18H);  $^{13}\text{C}$  NMR (150 MHz,  $\text{CDCl}_3$ , 298 K):  $\delta$  142.3, 140.4, 140.0, 138.8 (CH), 135.4 (CH), 134.6 (CH), 129.0 (CH), 126.9 (CH), 126.5 (CH), 84.0, 25.0 ( $\text{CH}_3$ ),  $-0.8$  ( $\text{CH}_3$ ) (the signal for the carbon nucleus bonded to a boron nucleus was not observed due to the quadrupolar relaxation induced by the boron nuclei); HRMS (APCI) ( $m/z$ ):  $[\text{M}+\text{H}]^+$  calcd. for  $\text{C}_{36}\text{H}_{53}\text{B}_2\text{O}_4\text{Si}$  625.3736, found 625.3710.

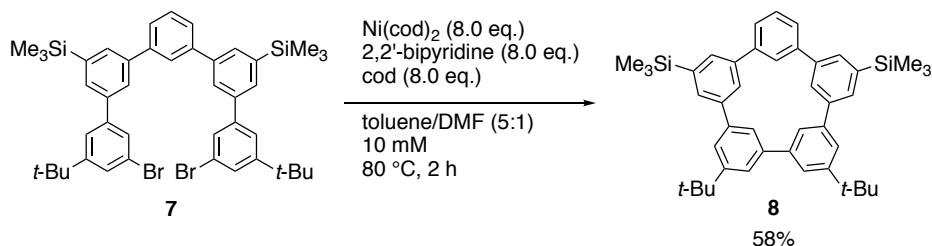
### Quinquephenyl **7**



A mixture of diborylated terphenyl **5** (1.88 g, 3.00 mmol), 1,3-dibromo-5-*tert*-butylbenzene (**6**) (5.26 g, 18.0 mmol),  $\text{Pd}(\text{PPh}_3)_4$  (347 mg, 0.300 mmol) and potassium carbonate (2.07 g, 15.0 mmol) in DMF (27 mL) and  $\text{H}_2\text{O}$  (3 mL) was stirred at  $80^\circ\text{C}$  for

15 h before the addition of water (30 mL) and AcOEt (50 mL). The organic layer was separated, and the aqueous layer was extracted with AcOEt (30 mL  $\times$  3). The combined organic layer was washed with brine (150 mL), dried over Na<sub>2</sub>SO<sub>4</sub> and concentrated in vacuo. The crude material was purified by silica gel column chromatography (eluent: from hexane to hexane/toluene = 25:1) and GPC (YMC-GPC T30000-40, T4000-40 and T2000-40 columns; eluent: CHCl<sub>3</sub>). The title compound was obtained as a white powder in 65% yield (1.56 g). <sup>1</sup>H NMR (600 MHz, CDCl<sub>3</sub>, 298 K):  $\delta$  7.98 (s, 1H), 7.89 (d, *J* = 1.8 Hz, 2H), 7.87 (t, *J* = 1.8 Hz, 2H), 7.78 (s, 2H), 7.76 (dd, *J* = 7.8, 1.8 Hz, 2H), 7.70 (t, *J* = 1.8 Hz, 2H), 7.68 (t, *J* = 7.8 Hz, 1H), 7.65 (t, *J* = 1.8 Hz, 2H), 7.63 (t, *J* = 1.8 Hz, 2H), 1.50 (s, 18H), 0.47 (s, 18H); <sup>13</sup>C NMR (150 MHz, CDCl<sub>3</sub>, 298 K):  $\delta$  154.1, 143.5, 142.3, 142.2, 141.4, 140.7, 131.9 (CH), 131.5 (CH), 129.5 (CH), 127.8 (CH), 127.8 (CH), 127.3 (CH), 126.9 (CH), 126.8 (CH), 123.6 (CH), 123.0, 35.2, 31.5 (CH<sub>3</sub>), -0.8 (CH<sub>3</sub>); HRMS (APCI) (*m/z*): [M]<sup>+</sup> calcd. for C<sub>44</sub>H<sub>52</sub>Br<sub>2</sub>Si<sub>2</sub> 794.1969, found 794.1971.

#### [5]CMP 8

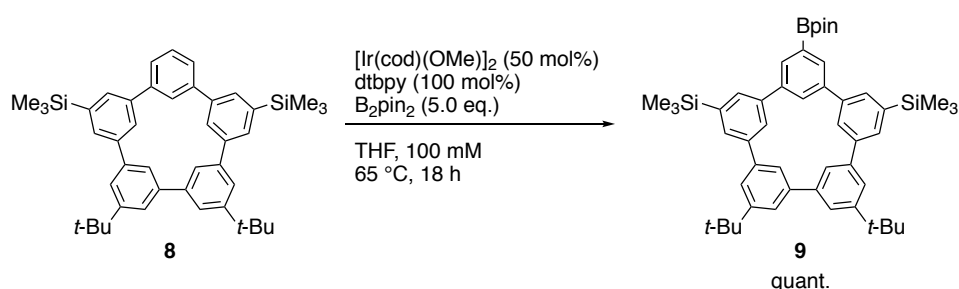


A mixture of 2,2'-bipyridine (1.57 g, 10.0 mmol), 1,5-cyclooctadiene (1.23 mL, 10.0 mmol) and bis(1,5-cyclooctadiene)nickel(0) (2.76 g, 10.0 mmol) in a mixture of toluene (21 mL) and DMF (21 mL) was stirred at 80 °C for 30 min. A solution of quinquiphenyl **7** (1.00 g, 1.25 mmol) in toluene (84 mL) was added dropwise to the mixture over 1 h, and the stirring was continued for an additional 2 h at 80 °C. After the reaction mixture was cooled to room temperature, 1 M HCl aq. (*ca.* 100 mL) was added, and the mixture was stirred vigorously for 2 h. The organic layer was separated, and the aqueous layer was extracted with toluene (80 mL  $\times$  3). The combined organic layer was washed with brine (200 mL), dried over Na<sub>2</sub>SO<sub>4</sub> and concentrated in vacuo. The residue was passed through a pad of silica gel with toluene as eluent and purified by GPC (YMC-GPC T30000-40, T4000-40 and T2000-40 columns; eluent: CHCl<sub>3</sub>). The title compound was obtained as a white powder in 58% yield as a CHCl<sub>3</sub> adduct (474 mg). <sup>1</sup>H NMR (600 MHz, CDCl<sub>3</sub>, 298 K):  $\delta$  8.49 (s, 1H), 8.44 (s, 2H), 8.23 (s, 2H), 7.85 (m, 4H), 7.76 (m,



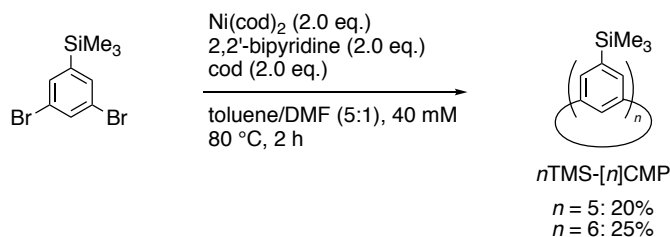
6H), 7.53 (t,  $J = 7.8$  Hz, 1H), 1.51 (s, 18H), 0.40 (s, 18H);  $^{13}\text{C}$  NMR (150 MHz,  $\text{CDCl}_3$ , 298 K):  $\delta$  152.2, 141.5, 141.5 (2C), 141.4, 141.4, 140.6, 135.6 (CH), 135.1 (CH), 133.0 (CH), 128.9 (2 $\times$ CH), 128.8 (CH), 124.0 (CH), 121.2 (CH), 121.2 (CH), 35.5, 32.0 ( $\text{CH}_3$ ),  $-0.6$  ( $\text{CH}_3$ ); HRMS (APCI) ( $m/z$ ):  $[\text{M}]^+$  calcd. for  $\text{C}_{44}\text{H}_{52}\text{Si}_2$  636.3602, found 636.3596; Elemental analysis (%): calcd. for  $(\text{C}_{44}\text{H}_{52}\text{Si}_2)_1(\text{CHCl}_3)_{0.15}$ , C 80.96, H 8.03, Cl 2.44, found, C 80.81, H 8.04, Cl 2.26.

### Borylated [5]CMP 9



Prior to the reaction, powders of [5]CMP **8**• $(\text{CHCl}_3)_{0.15}$  (118.5 mg, 0.186 mmol) were dissolved in cyclohexane 10 mL and evaporated, which was repeated three times for removal of  $\text{CHCl}_3$ . The thus-obtained powders were then mixed with bis(pinacolato)diboron (236 mg, 0.930 mmol), (1,5-cyclooctadiene)(methoxy)iridium(I) dimer (62 mg, 0.093 mmol), and 4,4'-di-*tert*-butyl-2,2'-bipyridyl (dtbpy; 50 mg, 0.186 mmol) in THF (2.0 mL), and the reaction was stirred at 65 °C for 18 h. After the mixture was cooled to ambient temperature, it was passed through a pad of silica gel with THF as eluent and the solvent was removed in vacuo. The residue was purified by GPC (YMC-GPC T2000 and T4000 columns; eluent:  $\text{CHCl}_3$ ). The title compound was obtained as an off-white powder in quantitative yield (141 mg).  $^1\text{H}$  NMR (600 MHz,  $\text{CDCl}_3$ , 298 K):  $\delta$  8.53 (s, 1H), 8.39 (s, 2H), 8.27 (s, 2H), 8.20 (d,  $J = 1.7$  Hz, 2H), 7.92 (d,  $J = 1.7$  Hz, 2H), 7.85 (d,  $J = 1.7$  Hz, 2H), 7.76 (d,  $J = 1.7$  Hz, 4H), 1.50 (s, 18H), 1.44 (s, 12H), 0.41 (s, 18H);  $^{13}\text{C}$  NMR (150 MHz,  $\text{CDCl}_3$ , 298 K):  $\delta$  152.3, 141.4, 141.3, 141.2, 141.2, 141.2, 140.7, 138.4 (CH), 135.8 (CH), 132.6 (CH), 130.4 (CH), 129.2 (CH), 128.8 (CH), 121.2 (CH), 121.1 (CH), 84.3, 35.5, 32.0 ( $\text{CH}_3$ ), 25.1 ( $\text{CH}_3$ ),  $-0.6$  ( $\text{CH}_3$ ) (the signal for the carbon nucleus bonded to a boron nucleus was not observed due to the quadrupolar relaxation induced by the boron nuclei); HRMS (APCI) ( $m/z$ ):  $[\text{M}]^+$  calcd. for  $\text{C}_{50}\text{H}_{63}\text{BO}_2\text{Si}$  761.4490, found 761.4504.

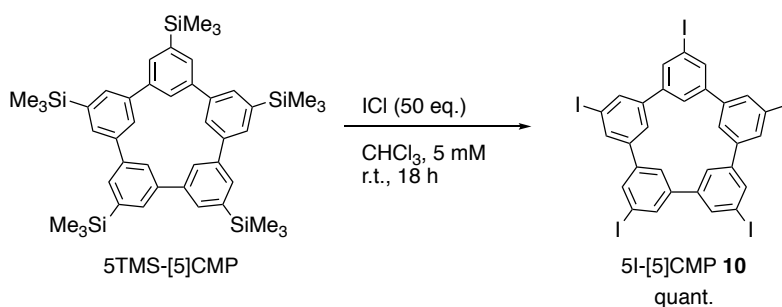
## $n$ TMS- $[n]$ CMP



A mixture of 2,2'-bipyridine (15.6 g, 100 mmol), 1,5-cyclooctadiene (13.3 mL, 100 mmol) and bis(1,5-cyclooctadiene)nickel(0) (27.5 g, 100 mmol) in a mixture of toluene (210 mL) and DMF (210 mL) was stirred at 80 °C for 30 min. A solution of 1,3-dibromo-5-trimethylsilylbenzene (15.4 g, 50 mmol) in toluene (830 mL) was added dropwise to the mixture over 1 h, and the stirring was continued for an additional 2 h at 80 °C. After the reaction mixture was cooled to room temperature, 2 M HCl aq. (*ca.* 850 mL) was added, and the mixture was stirred vigorously for 2 h. The organic layer was separated, and the aqueous layer was extracted with toluene (350 mL  $\times$  2). The combined organic layer was washed with brine (1 L), dried over Na<sub>2</sub>SO<sub>4</sub> and concentrated in vacuo. The residue was suspended in hexane 150 mL and subjected to sonication. The insoluble material was collected by filtration to give pure 6TMS-[6]CMP as a white powder in 19% yield (1.44 g). The filtrate was then purified by GPC (JAI GEL 2.5H-40, 2H-40 and 1H-40 columns, 40  $\phi$   $\times$  600 mm; eluent: CHCl<sub>3</sub>) to afford 6TMS-[6]CMP and 5TMS-[5]CMP as a white powder in 6% (0.43 g) and 20% (1.50 g), respectively. Spectra of 6TMS-[6]CMP were identical to those in the literature.<sup>21</sup>

**5TMS-[5]CMP:** <sup>1</sup>H NMR (600 MHz, CDCl<sub>3</sub>, 298 K):  $\delta$  8.52 (t,  $J$  = 1.8 Hz, 5H), 8.00 (d,  $J$  = 1.8 Hz, 10H), 0.54 (s, 45H); <sup>13</sup>C NMR (150 MHz, CDCl<sub>3</sub>, 298 K):  $\delta$  141.6, 141.0, 135.8 (CH), 128.9 (CH), -0.6 (CH<sub>3</sub>); HRMS (APCI) ( $m/z$ ): [M]<sup>+</sup> calcd. for C<sub>45</sub>H<sub>60</sub>Si<sub>5</sub> 740.3536, found 740.3511.

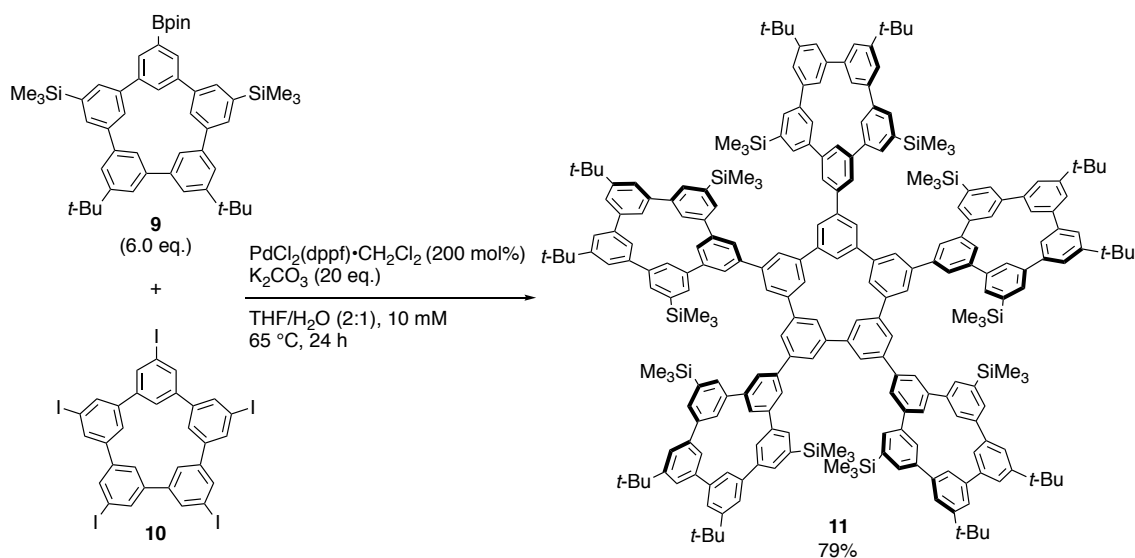
## 5I-[5]CMP 10



To a solution of 5TMS-[5]CMP (307 mg, 0.414 mmol) in CHCl<sub>3</sub> (20 mL) was added

a solution of ICl (3.40 g, 20.9 mmol) in  $\text{CHCl}_3$  (60 mL). The mixture was stirred at r.t. in dark for 18 h before the addition of 3.8 M  $\text{Na}_2\text{S}_2\text{O}_3$  aq. (40 mL). The solid was then collected by filtration and washed subsequently with water and  $\text{CHCl}_3$  to give the title compound as off-white powders in quantitative yield (417 mg).  $^1\text{H}$  NMR (600 MHz,  $\text{CDCl}_3$ , 298 K):  $\delta$  8.19 (t,  $J = 1.6$  Hz, 5H), 8.04 (d,  $J = 1.6$  Hz, 10H); The  $^{13}\text{C}$  NMR spectrum could not be obtained owing to the low solubility of the title compound. HRMS (APCI) ( $m/z$ ):  $[\text{M}]^+$  calcd. for  $\text{C}_{36}\text{H}_{18}\text{I}_6$  1009.6392, found 1009.6364.

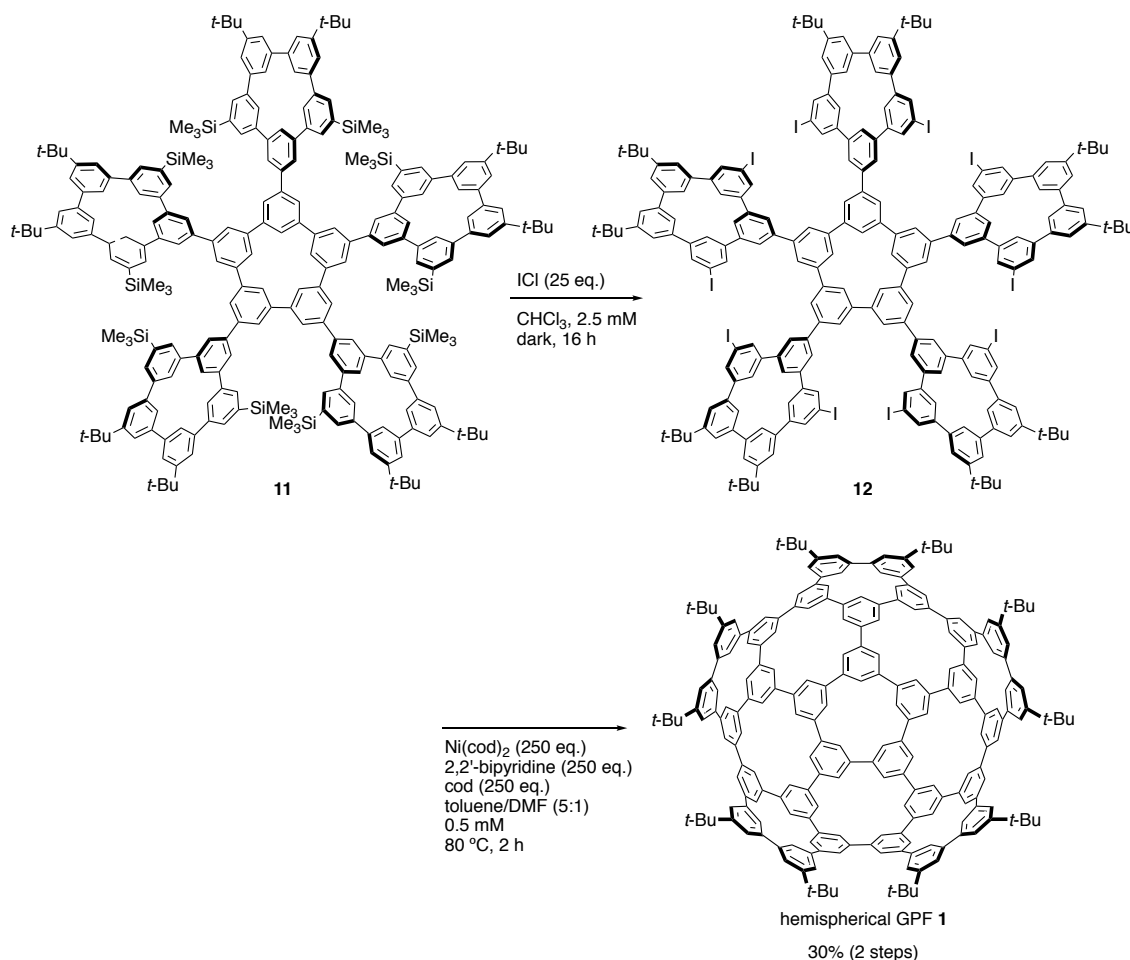
### Starfish-shaped precursor 11



To a solution of [5]CMP 7 (10.8 mg, 10.6  $\mu\text{mol}$ ), [5]CMP 5 (48.5 mg, 63.6  $\mu\text{mol}$ ) and  $\text{PdCl}_2(\text{dppf})\cdot\text{CH}_2\text{Cl}_2$  (17.3 mg, 21.2  $\mu\text{mol}$ ) in THF (1.0 mL) was added a solution of potassium carbonate (29.3 mg, 212  $\mu\text{mol}$ ) in  $\text{H}_2\text{O}$  (0.5 mL). The mixture was stirred at  $65^\circ\text{C}$  for 24 h before the addition of water (10 mL) and  $\text{CHCl}_3$  (10 mL). The organic layer was separated, and the aqueous layer was extracted with  $\text{CHCl}_3$  (10 mL  $\times$  2). The combined organic layer was washed with brine (20 mL), dried over  $\text{Na}_2\text{SO}_4$  and concentrated in vacuo. The crude material was purified by GPC (JAI GEL 2.5H-40, 2H-40, and 1H-40 columns; eluent:  $\text{CHCl}_3$ ). The title compound was obtained as a white powder in 79% yield (29.9 mg).  $^1\text{H}$  NMR (600 MHz,  $\text{CDCl}_3$ , 298 K):  $\delta$  8.85 (s, 5H), 8.52 (s, 5H), 8.49 (s, 10H), 8.28 (s, 10H), 8.27 (s, 10H), 8.10 (d,  $J = 1.8$  Hz, 10H), 7.93 (d,  $J = 1.2$  Hz, 10H), 7.85 (d,  $J = 1.2$  Hz, 10H), 7.77 (d,  $J = 1.8$  Hz, 20H), 1.50 (s, 90H), 0.35 (s, 90H);  $^{13}\text{C}$  NMR (150 MHz,  $\text{CDCl}_3$ , 298 K):  $\delta$  152.3, 144.1, 143.3, 142.1, 141.9, 141.6, 141.4 (2C), 141.3, 140.5, 135.9 (CH), 134.6 (CH), 134.5 (CH), 132.9 (CH), 129.1 (CH),

129.0 (CH), 124.6 (CH), 123.9 (CH), 121.2 (CH), 121.2 (CH), 35.5, 32.0 (CH<sub>3</sub>), −0.6 (CH<sub>3</sub>); MS (MALDI-TOF) (*m/z*): [M+H]<sup>+</sup> calcd. for C<sub>250</sub>H<sub>271</sub>Si<sub>10</sub> 3555.7, found 3555.7.

### Hemispherical GPF 1



To a solution of precursor **11** (54.6 mg, 15.4  $\mu\text{mol}$ ) in  $\text{CHCl}_3$  (1 mL) was added a solution of  $\text{ICl}$  (62.0 mg, 384  $\mu\text{mol}$ ) in  $\text{CHCl}_3$  (5 mL). The mixture was stirred at r.t. in dark for 16 h before the addition of 1 M  $\text{Na}_2\text{SO}_3$  aq. (1 mL). The organic layer was separated, and the aqueous layer was extracted with  $\text{CHCl}_3$  (25 mL  $\times$  2). The combined organic layer was washed with brine (20 mL), dried over  $\text{Na}_2\text{SO}_4$ , and concentrated in vacuo. After washing with hexane and chloroform, iodinated precursor **12** was obtained as off-white powders (51.9 mg). The crude compound was directly used for the next reductive coupling. Thus, a mixture of 2,2'-bipyridine (495 mg, 3.17 mmol), 1,5-cyclooctadiene (0.39 mL, 3.17 mmol) and bis(1,5-cyclooctadiene)nickel(0) (868 mg, 3.17 mmol) in a mixture of toluene (5 mL) and DMF (5 mL) was stirred at 80 °C for 30 min. A solution of the crude compound **12** (51.9 mg) in toluene (20 mL) was added dropwise

to the mixture over 1 h, and the stirring was continued for an additional 2 h at 80 °C. After the reaction mixture was cooled to room temperature, 1 M HCl aq. (*ca.* 10 mL) was added, and the mixture was stirred vigorously for 2 h. The organic layer was separated, and the aqueous layer was extracted with toluene (250 mL  $\times$  2). The combined organic layer was washed with brine (20 mL), dried over Na<sub>2</sub>SO<sub>4</sub> and concentrated in vacuo. The residue was purified by GPC (JAI GEL 2.5H-40, 2H-40, and 1H-40 columns; eluent: CHCl<sub>3</sub>) to afford the title compound in 30% yield (12.0 mg). <sup>1</sup>H NMR (600 MHz, CDCl<sub>3</sub>, 298 K):  $\delta$  8.96 (s, 5H), 8.67 (s, 15H), 8.65 (s, 10H), 8.53 (s, 10H), 8.42 (s, 10H), 8.09 (s, 10H), 8.03 (s, 10H), 7.83 (s, 10H), 7.76 (s, 10H), 1.47 (s, 90H); <sup>13</sup>C NMR (150 MHz, CDCl<sub>3</sub>, 298 K):  $\delta$  152.5, 144.0, 141.9, 141.7, 141.3, 140.9, 140.6, 140.4, 139.9, 139.7, 133.1 (CH), 132.9 (CH), 132.8 (CH), 129.9 (CH), 124.9 (CH), 121.7 (CH), 121.5 (CH), 121.4 (CH), 121.3 (CH), 121.0 (CH), 35.5, 31.9 (CH<sub>3</sub>); HRMS (MALDI-TOF) (*m/z*): [M]<sup>+</sup> calcd. for C<sub>220</sub>H<sub>180</sub> 2821.4080, found 2821.4143.

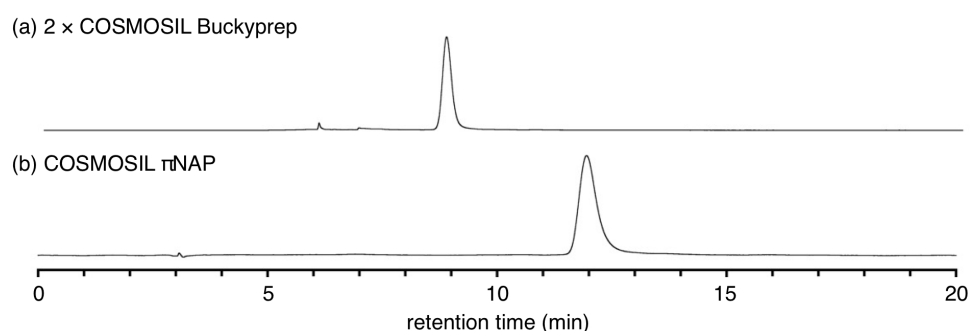


**Figure S1.** HPLC chromatograms of hemispherical GPF **1** with two different stationary phases. Conditions: flow rate = 1.0 mL/min, temperature = 40 °C and detection = UV 280 nm. (a) COSMOSIL Buckyprep, two columns connected in tandem, eluent: MeOH/CHCl<sub>3</sub> = 1:19. (b) COSMOSIL πNAP, eluent: CHCl<sub>3</sub>.

### Crystallographic analysis

A single crystal of GPF hemisphere **1** suitable for X-ray crystallographic analysis was obtained by slow diffusion of 2-propanol into chlorobenzene solution of **1**. The single crystal was mounted on a thin polymer tip with a cryoprotectant oil. The diffraction analyses were carried out initially at the SPring-8 BL26B1 beamline and finally at the KEK Photon Factory BL17A beamline with a Dectris EIGER X 16M PAD detector (95 K).<sup>22</sup> The collected diffraction data were processed with the XDS software program.<sup>23</sup> The structure was solved by the direct method with SHELXT program<sup>24</sup> and refined by

full-matrix least-squares on  $F^2$  using the SHELXL program suite<sup>25</sup> running on the Yadokari-XG 2009 software program.<sup>26</sup> In the refinements, disordered structures in GPF hemisphere molecules were restrained by SIMU, DFIX and DANG. Disordered solvent molecules were modeled with 165 molecules of 2-propanol and two chlorobenzene molecules restrained by SIMU, DFIX and DANG. The non-hydrogen atoms were analyzed anisotropically, and hydrogen atoms were input at the calculated positions and refined with a riding model. The refinement data are shown in Tables S1.

Crystallographic data were deposited in the Cambridge Crystallographic Data Centre (CCDC 1968742). The data can be obtained free of charge from The Cambridge Crystallographic Data Centre via [www.ccdc.cam.ac.uk/data\\_request/cif](http://www.ccdc.cam.ac.uk/data_request/cif).

**Table S1.** Crystal data of GPF hemisphere 1.

CCDC	1968742
Empirical formula	$C_{1179.01}H_{1506.36}ClO_{97.67}$
Formula weight	17276.40
Temperature	95(2) K
Wavelength	0.90000 Å
Crystal system	Triclinic
Space group	$P\bar{1}$
Unit cell dimensions	$a = 28.650(6)$ Å $\alpha = 85.83(3)^\circ$ $b = 31.760(6)$ Å $\beta = 80.26(3)^\circ$ $c = 34.460(7)$ Å $\gamma = 70.16(3)^\circ$
Volume	29067(12) Å <sup>3</sup>
Z	1
Density (calculated)	0.987 mg/m <sup>3</sup>
Absorption coefficient	0.107 mm <sup>-1</sup>
$F(000)$	9379
Crystal size	0.15 × 0.02 × 0.01 mm <sup>3</sup>
Theta range for data collection	0.759° to 32.827°
Index ranges	−34 ≤ $h$ ≤ 34, −38 ≤ $k$ ≤ 38, −41 ≤ $l$ ≤ 41
Reflections collected	963739
Independent reflections	104684 [ $R(\text{int}) = 0.0368$ ]
Completeness to theta = 32.684°	98.6%

Absorption correction	Semi-empirical from equivalents
Refinement method	Full-matrix least-squares on $F^2$
Data / restraints / parameters	104684 / 23646 / 10743
Goodness-of-fit on $F^2$	1.331
Final $R$ indices [ $I > 2\sigma(I)$ ]	$R_1 = 0.1107$ , $wR_2 = 0.2996$
$R$ indices (all data)	$R_1 = 0.1299$ , $wR_2 = 0.3238$
Largest diff. peak and hole	0.500 and $-0.452 \text{ e} \cdot \text{\AA}^{-3}$

### Theoretical analysis

The Gaussian 16 program suite was used in all the calculations.<sup>27</sup> Semi-empirical calculations were performed at the PM6 level.<sup>17</sup> Density functional theory (DFT) calculations were performed for geodesic polyarenes by the B3LYP functional, the gradient correction of the exchange functional by Becke<sup>28</sup> and the correlation functional by Lee, Yang and Parr<sup>29</sup> with the 6-31G(d,p) split valence plus polarization basis set.<sup>30</sup>

### Geometry optimization of polyarenes

Geometry optimizations of some representative geodesic polyarenes were performed at the B3LYP/6-31G(d,p) level of the theory. For the calculations of bisectonal segments of  $C_{60}$ , initial geometries were obtained from the literature<sup>6</sup> and was optimized. The structures were analyzed by using POAV as a reference.

### Scan analysis

The initial structure of **1** for the torsional scan analysis was first obtained as follows. The *t*-Bu groups of the crystal structure were replaced with hydrogen atoms, and the structure of [5]CMP at the rim were tweaked so that the geometry possessed the pseudo- $C_s$  symmetry after the PM6 geometry optimization. The initial structure was then subjected to the torsional scan analysis<sup>8</sup> by changing one biaryl linkage (red; Figure 4) at the omphalos from  $0^\circ$  to  $25^\circ$ . The final structure at  $25^\circ$  was then adopted as the initial structure for a second set of the scan calculations with another biaryl linkage (orange; Figure 4). The scan calculations were performed five sets of biaryl linkages in total, and the results were shown in Figure 4 and Figure S5.

Supplementary data  
NMR spectra

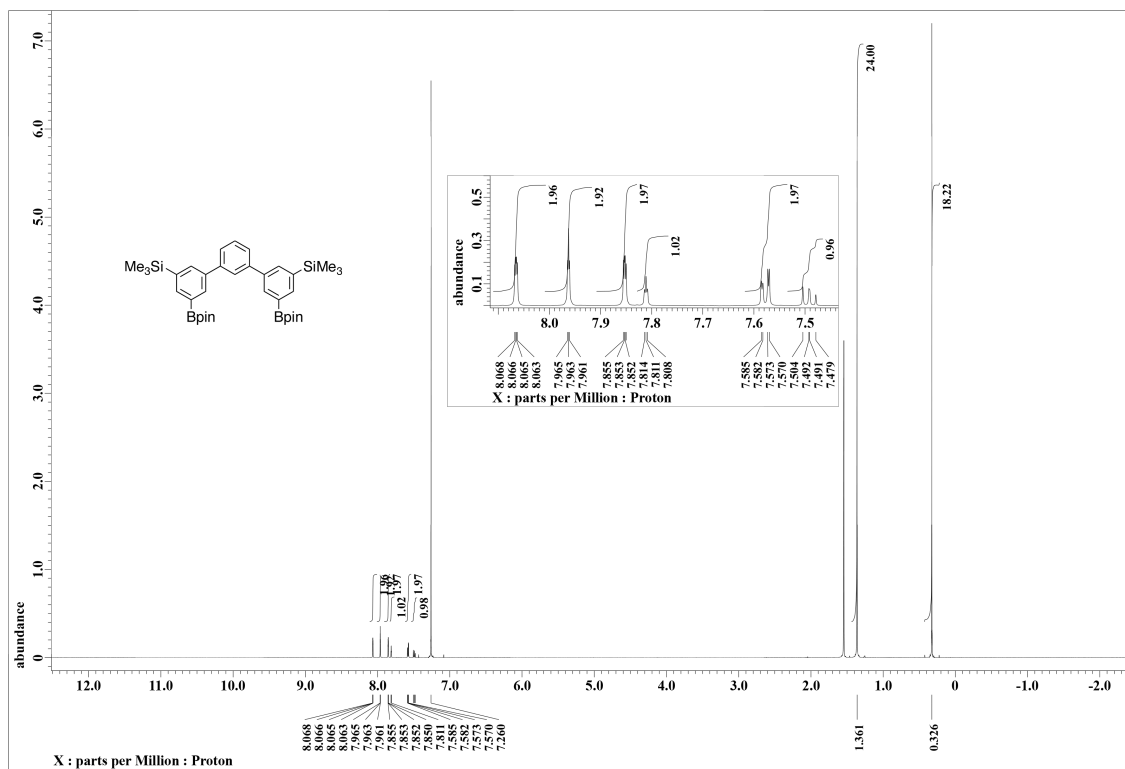


**Figure S7.**  $^1\text{H}$  NMR spectrum of diborylated terphenyl **5** (CDCl<sub>3</sub>, 600 MHz, 298 K).





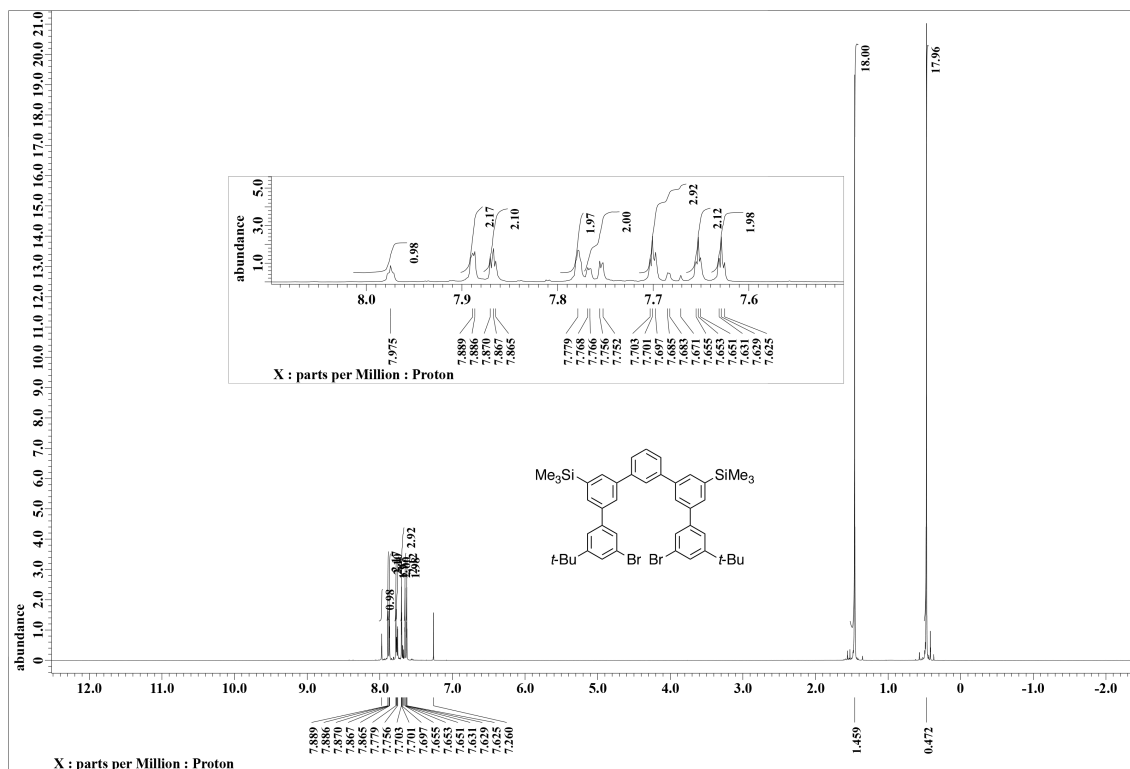


**Figure S9.** <sup>1</sup>H NMR spectrum of quinquephenyl **7** (CDCl<sub>3</sub>, 600 MHz, 298 K).

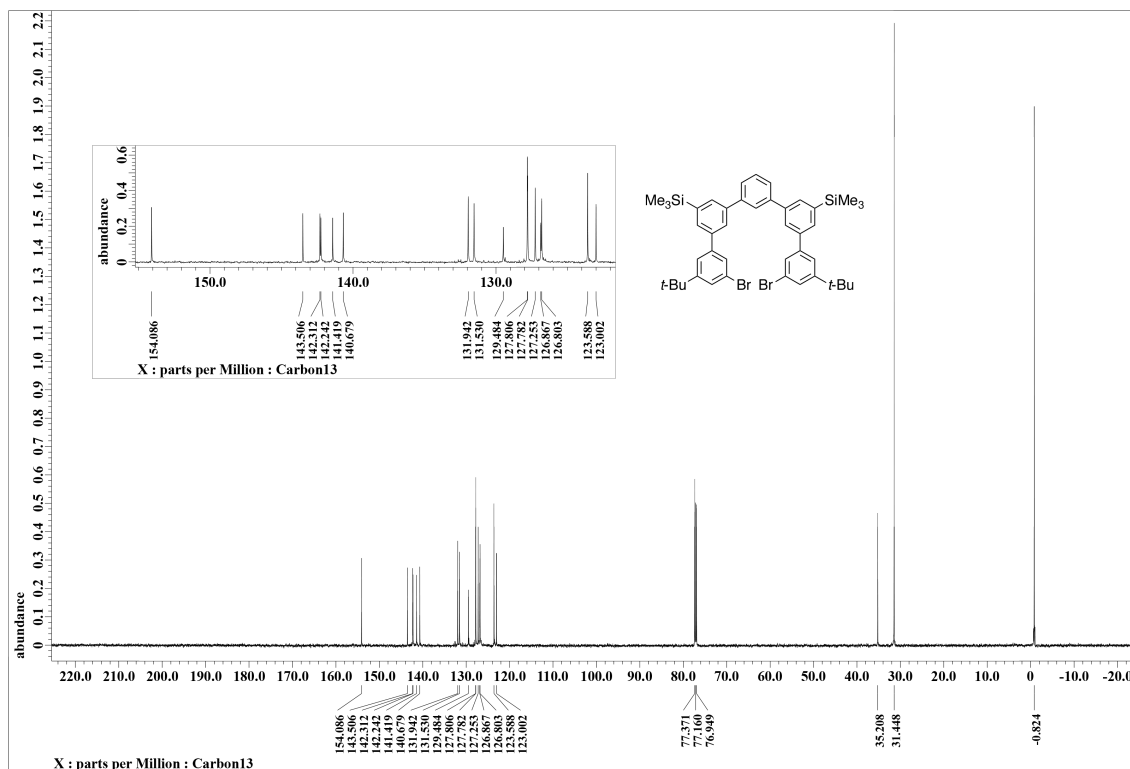


**Figure S10.**  $^{13}\text{C}$  NMR spectrum of quinquephenyl **7** (CDCl<sub>3</sub>, 150 MHz, 298 K).

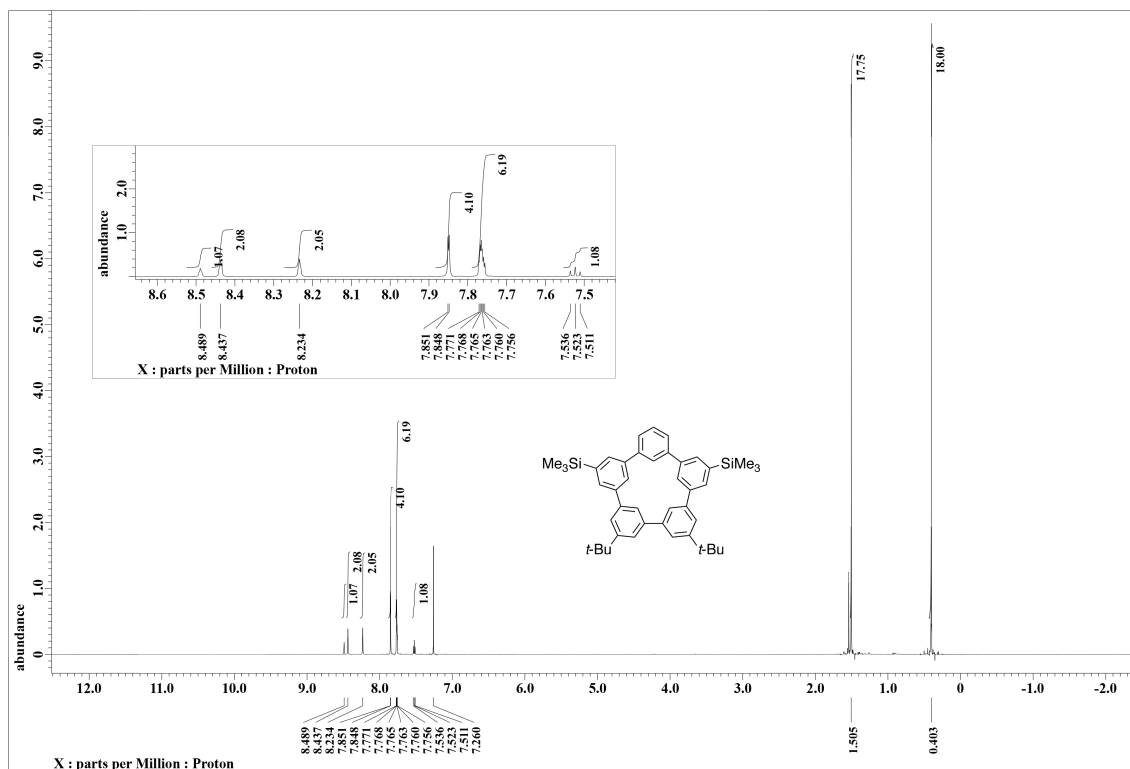


**Figure S11.**  $^1\text{H}$  NMR spectrum of [5]CMP **8** ( $\text{CDCl}_3$ , 600 MHz, 298 K).



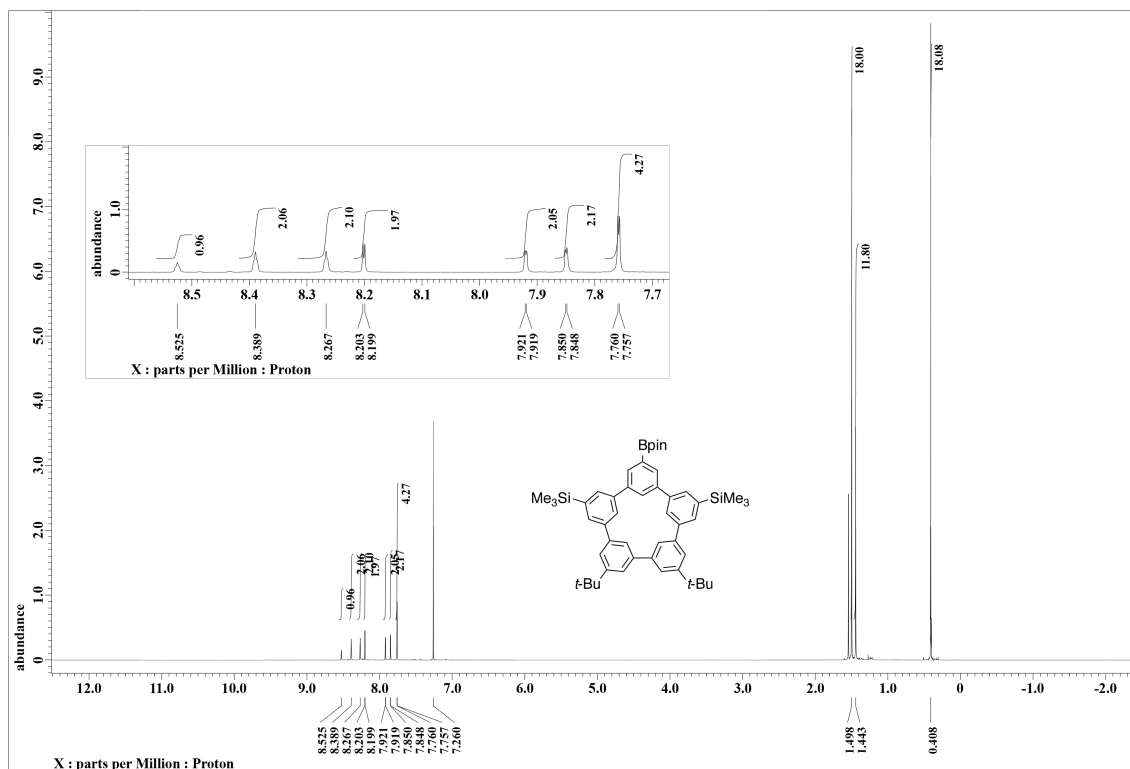


**Figure S13.**  $^1\text{H}$  NMR spectrum of [5]CMP **9** ( $\text{CDCl}_3$ , 600 MHz, 298 K).



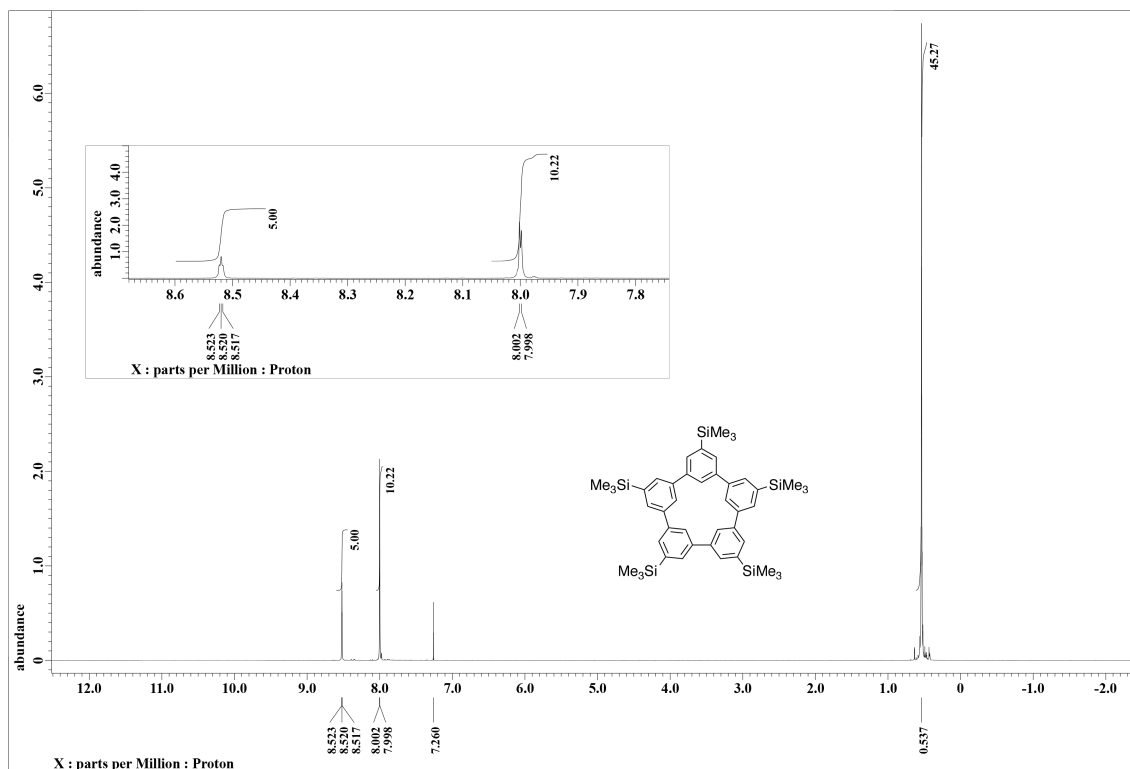


**Figure S15.**  $^1\text{H}$  NMR spectrum of 5TMS-[5]CMP ( $\text{CDCl}_3$ , 600 MHz, 298 K).



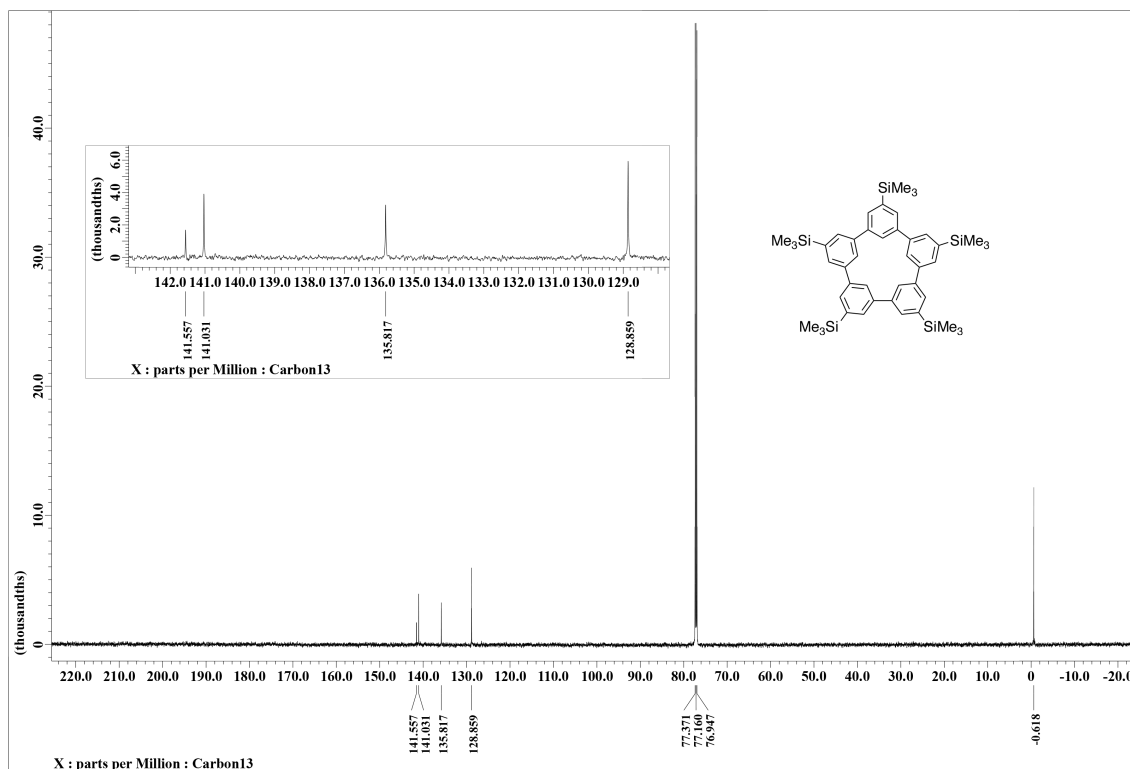


**Figure S16.**  $^{13}\text{C}$  NMR spectrum of 5TMS-[5]CMP ( $\text{CDCl}_3$ , 150 MHz, 298 K).

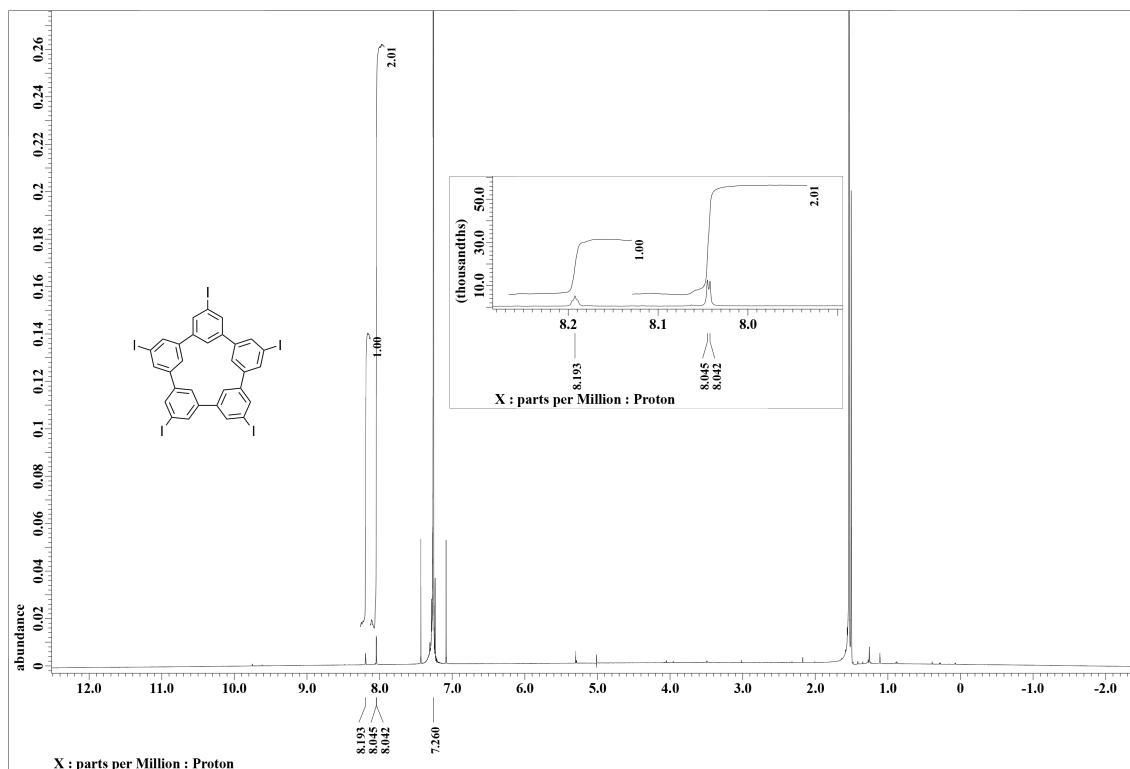


**Figure S17.**  $^1\text{H}$  NMR spectrum of 5I-[5]CMP **10** ( $\text{CDCl}_3$ , 600 MHz, 298 K).

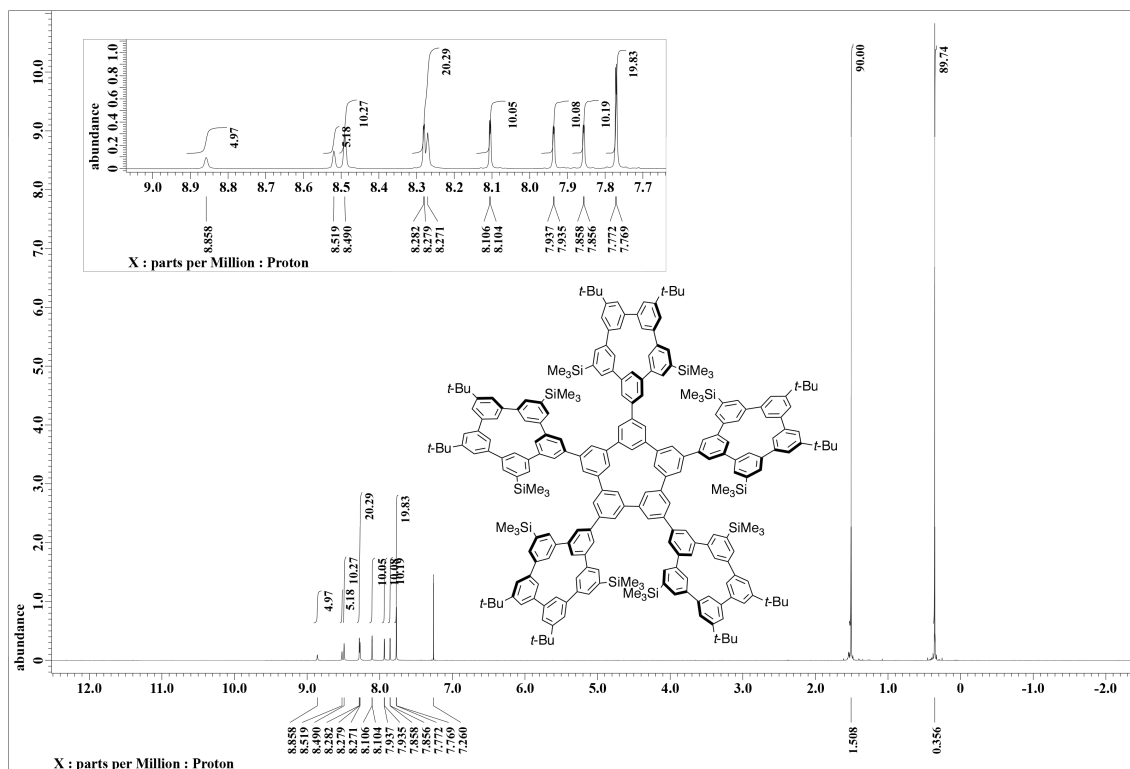


**Figure S18.**  $^1\text{H}$  NMR spectrum of precursor **11** ( $\text{CDCl}_3$ , 600 MHz, 298 K).

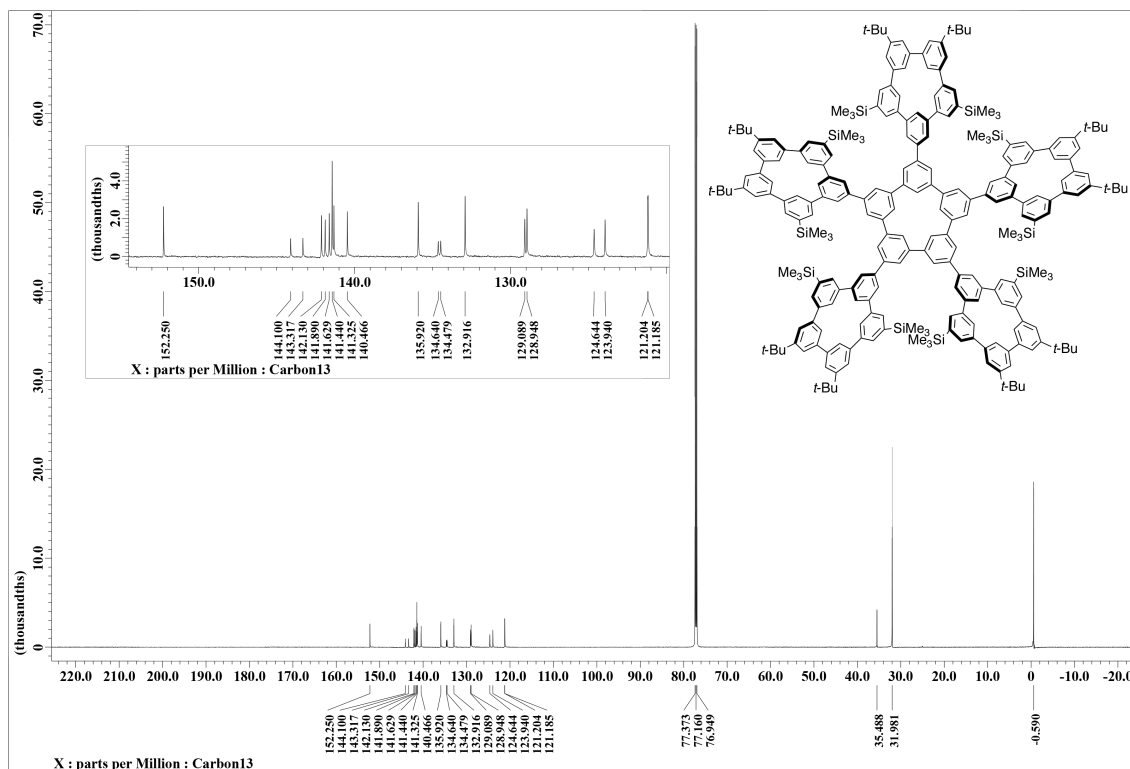


**Figure S19.** <sup>13</sup>C NMR spectrum of precursor **11** (CDCl<sub>3</sub>, 150 MHz, 298 K).

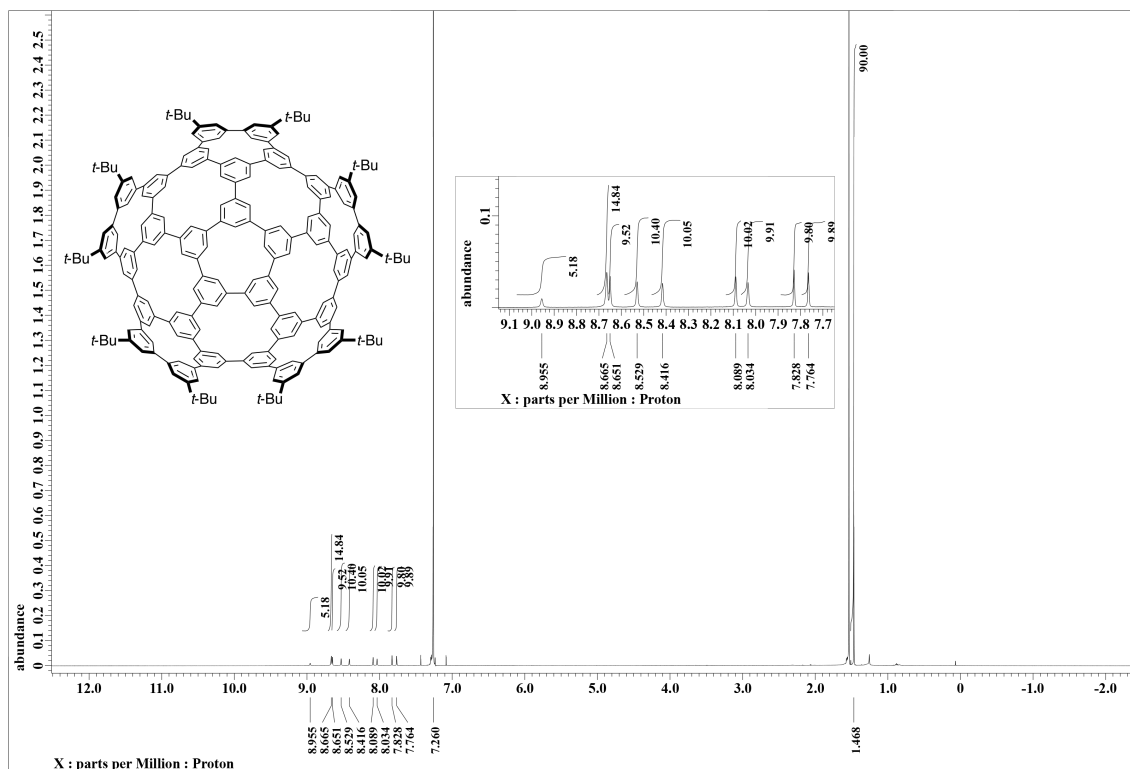


**Figure S20.**  $^1\text{H}$  NMR spectrum of hemispherical GPF 1 ( $\text{CDCl}_3$ , 600 MHz, 298 K).

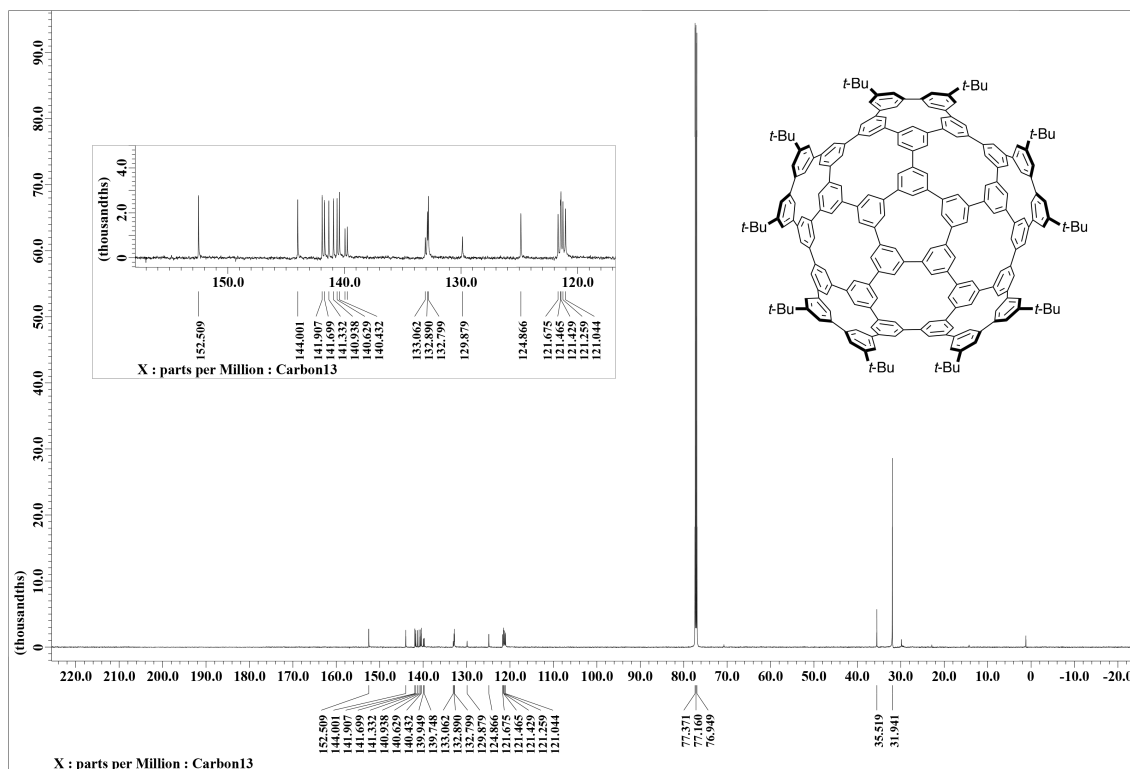


**Figure S21.**  $^{13}\text{C}$  NMR spectrum of hemispherical GPF **1** ( $\text{CDCl}_3$ , 150 MHz, 298 K).

### 3.10 References

1. (a) V. M. Tsefrikas, L. T. Scott, *Chem. Rev.* **2006**, *106*, 4868-4884; (b) Y. Segawa, H. Ito, K. Itami, *Nat. Rev. Mater.* **2016**, *1*, 1-14.
2. H. Kenner, *Geodesic Math and How to Use It*, 2nd ed., University of California Press, Berkeley, **1976**.
3. (a) W. E. Barth, R. G. Lawton, *J. Am. Chem. Soc.* **1966**, *88*, 380-381. (b) L. T. Scott, M. M. Hashemi, D. T. Meyer, H. B. Warren, *J. Am. Chem. Soc.* **1981**, *113*, 7082-7084. (c) A. M. Butterfield, B. Gilomen, J. S. Siegel, *Org. Process Res. Dev.* **2012**, *16*, 664-676.
4. A. H. Abdourazak, Z. Marcinow, A. Sygula, R. Sygula, P. W. Rabideau, *J. Am. Chem. Soc.* **1995**, *117*, 6410-6411.
5. S. Hagen, M. S. Bratcher, M. S. Erickson, G. Zimmermann, L. T. Scott, *Angew. Chem. Int. Ed.* **1997**, *36*, 406-408.
6. F. Geneste, A. Moradpour, G. Dive, D. Peeters, J. Malthête, J.-F. Sadoc, *J. Org. Chem.* **2002**, *67*, 605-607.
7. L. T. Scott, *Angew. Chem. Int. Ed.* **2004**, *43*, 4994-5007.
8. (a) K. Ikemoto, R. Kobayashi, S. Sato, H. Isobe, *Angew. Chem. Int. Ed.* **2017**, *56*, 6511-6514. (b) K. Ikemoto, J. Lin, R. Kobayashi, S. Sato, H. Isobe, *Angew. Chem. Int. Ed.* **2018**, *57*, 8555-8559. (c) Z. Sun, K. Ikemoto, T. M. Fukunaga, T. Koretsune, R. Arita, S. Sato, H. Isobe, *Science* **2019**, *363*, 151-155.
9. Phenine is a name coined to designate the planar trigonal structure of 1,3,5-trisubstituted benzene.
10. K. Yamamoto, T. Harada, M. Nakazaki, *J. Am. Chem. Soc.* **1983**, *105*, 7172-7173.
11. R. E. Smalley, *Acc. Chem. Res.* **1992**, *25*, 98-105.
12. (a) N. Miyaoura, K. Yamada, A. Suzuki, *Tetrahedron Lett.* **1979**, *20*, 3437-3440. (b) N. Miyaoura, A. Suzuki, *Chem. Rev.* **1995**, *95*, 2457-2483.
13. J. Y. Xue, K. Ikemoto, N. Takahashi, T. Izumi, H. Taka, H. Kita, S. Sato, H. Isobe, *J. Org. Chem.* **2014**, *79*, 9735-9739.
14. Interestingly, precursor **12** showed aggregation behavior in  $^1\text{H}$  NMR spectra, which was not observed for hemisphere **1**.
15. Theoretical calculations of **B** indeed indicated the presence of an ideal hemispherical

shape for this geodesic polyarene.

16. (a) R. C. Haddon, L. T. Scott, *Pure Appl. Chem.* **1986**, *58*, 137-142 (b) R. C. Haddon, *J. Phys. Chem. A* **2001**, *105*, 4164-4165. (c) R. C. Haddon, *Chem. Phys. Lett.* **1986**, *125*, 231-234 (d) R. C. Haddon, *Science* **1993**, *261*, 1545-1550.
17. Confusingly, there are some variations in POAV-related descriptors. In this study, we designate the POAV pyramidalization angle as  $\theta_p$  ( $= \theta_{\sigma\pi} - 90^\circ$ ) and the POAV dihedral angle between two POAV as  $\phi$ .
18. J. J. P. Stewart, *J. Mol. Model.* **2007**, *13*, 1173-1213.
19. (a) M. M. Boorum, Y. V. Vasil'ev, T. Drewello, L. T. Scott, *Science* **2001**, *294*, 828-831. (b) L. T. Scott, M. M. Boorum, B. J. McMahon, S. Hagen, J. Mack, J. Blank, H. Wegner, A. de Meijere, *Science* **2002**, *295*, 1500-1503.
20. Pangborn, A. B.; Giardello, M. A.; Grubbs, R. H.; Rosen, R. K.; Timmers, F. J. *Organometallics* **1996**, *15*, 1518-1520.
21. Pisula, W.; Kastler, M.; Yang, C.; Enkelmann, V.; Müllen, K. *Chem. Asian J.* **2007**, *2*, 51-56.
22. Förster, A.; Brandstetter, S.; Schulze-Bries, C. *Phil. Trans. R. Soc. A* **2019**, *362*, 20180241.
23. Kabsch, W. *J. Appl. Crystallogr.* **1993**, *26*, 795-800.
24. Sheldrick, G. M. *Acta Crystallogr. A* **2015**, *71*, 3-8.
25. Sheldrick, G. M. *Acta Crystallogr. A* **2008**, *64*, 112-122.
26. Kabuto, C.; Akine, S.; Nemoto, T.; Kwon, E. *J. Cryst. Soc. Jpn.* **2009**, *51*, 218-224.
27. *Gaussian 16, Revision B.01*, Frisch, M. J.; Trucks, G. W.; Schlegel, H. B.; Scuseria, G. E.; Robb, M. A.; Cheeseman, J. R.; Scalmani, G.; Barone, V.; Petersson, G. A.; Nakatsuji, H.; Li, X.; Caricato, M.; Marenich, A. V.; Bloino, J.; Janesko, B. G.; Gomperts, R.; Mennucci, B.; Hratchian, H. P.; Ortiz, J. V.; Izmaylov, A. F.; Sonnenberg, J. L.; Williams-Young, D.; Ding, F.; Lipparini, F.; Egidi, F.; Goings, J.; Peng, B.; Petrone, A.; Henderson, T.; Ranasinghe, D.; Zakrzewski, V. G.; Gao, J.; Rega, N.; Zheng, G.; Liang, W.; Hada, M.; Ehara, M.; Toyota, K.; Fukuda, R.; Hasegawa, J.; Ishida, M.; Nakajima, T.; Honda, Y.; Kitao, O.; Nakai, H.; Vreven, T.; Throssell, K.; Montgomery, Jr. J. A.; Peralta, J. E.; Ogliaro, F.; Bearpark, M. J.; Heyd, J. J.; Brothers, E. N.; Kudin, K. N.; Staroverov, V. N.; Keith, T. A.; Kobayashi, R.; Normand, J.;



- Raghavachari, K.; Rendell, A. P.; Burant, J. C.; Iyengar, S. S.; Tomasi, J.; Cossi, M.; Millam, J. M.; Klene, M.; Adamo, C.; Cammi, R.; Ochterski, J. W.; Martin, R. L.; Morokuma, K.; Farkas, O.; Foresman, J. B.; Fox, D. J. Gaussian, Inc., Wallingford CT, **2016**.
28. Becke, A. D.; *Phys. Rev. A* **1988**, 38, 3098-3100; Becke, A. D. *J. Chem. Phys.* **1993**, 98, 5648-5652.
29. Lee, C.; Yang, W.; Parr, R. G. *Phys. Rev. B* **1988**, 37, 785-789.
30. (a) Ditchfield, R.; Hehre, W. J.; Pople, J. A. *J. Chem. Phys.* **1971**, 54, 724-728. (b) Hehre, W. J.; Ditchfield, R.; Pople, J. A. *J. Chem. Phys.* **1972**, 56, 2257-2261. (c) Hariharan, P. C.; Pople, J. A. *Mol. Phys.* **1974**, 27, 209-214. (d) Gordon, M. S. *Chem. Phys. Lett.* **1980**, 76, 163-168. (e) Hariharan, P. C.; Pople, J. A. *Theor. Chim. Acta.* **1973**, 28, 213-222.

## Chapter 4. Quantitative Description of the Geometry of Phenine Nanocarbons

### 4.1 Introduction

The  $\pi$ -orbital axis vector (POAV) analysis has ingeniously introduced versatile geometric measures of curved  $\pi$ -systems,<sup>1</sup> which provides quantitative measures for the structural comparisons of curved, geodesic polyarenes (GPAs) comprising pyramidalized  $sp^2$ -carbon atoms (Figure 1).<sup>2,3</sup> By defining POAV ( $\nu_\pi$ ) as a  $\pi$ -orbital vector possessing equal angles to three  $\sigma$ -bond vectors ( $\nu_1/\nu_2/\nu_3$ ), we can evaluate the degree of nonplanarity, for instance, as a pyramidalization angle ( $\theta$ ) of the trigonal carbon atoms. The structural measures are useful not only for geometric comparisons but also for rough estimates of the strain energies induced by pyramidalizations.<sup>1</sup> As discussed in the preceding chapters, a larger trigonal planar unit, *i.e.*, 1,3,5-trisubstituted benzene (phenine), has been adopted to design larger geodesic structures called phenine nanocarbons.<sup>4,5,6,7</sup> The molecular design of GPAs and phenine nanocarbons commonly allows for synthesis of curved, geodesic structures by combining polygons of planar trigonal units. Despite the common geodesic design,<sup>8</sup> however, the sizes of the geometric structures of GPAs and phenine nanocarbons are extremely different, which hampers us in deriving and understanding the common geometric features of these isorecticular structures. We herein introduce geometric measures of phenine nanocarbons by inventing POAV-like descriptors for phenine panels. The descriptors originating from a vector named the curved phenine normal vector (CPNV) were found useful in showing the geometric features of phenine nanocarbons, and the similarities and differences between GPAs and phenine nanocarbons were visually clarified.

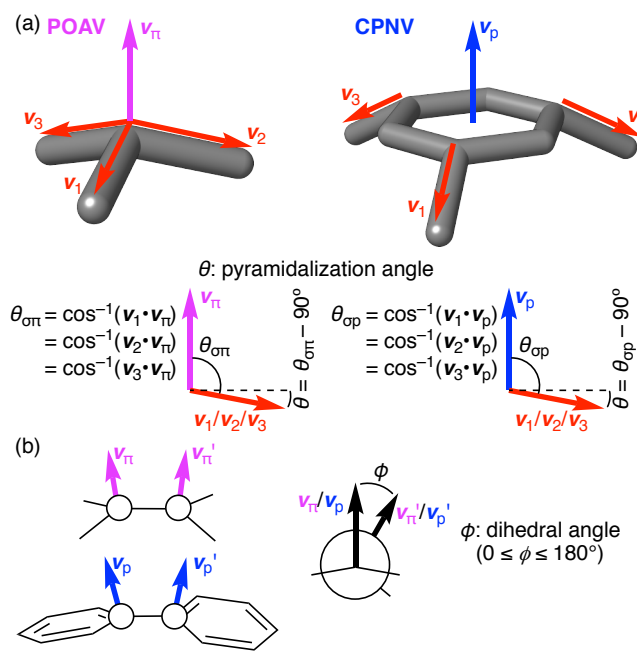


**Figure 1.** Definition of POAV, CPNV and geometric measures  $\theta$  and  $\phi$ .

## 4.2 Definition of the normal vector

The CPNV measures were invented to describe the structural deformations of phenine panels. To describe the nonplanarity of curved phenine panels, a vector normal to the deformed panel was first investigated. Among a few possible definitions examined as normal vectors (Figures 1 and 2), a definition similar to that of POAV was selected as the CPNV ( $\mathbf{v}_p$ ).<sup>1</sup> Thus, the  $\mathbf{v}_p$  vector is defined as a vector having equal angles to three  $\sigma$ -bond vectors in the following form:

$$\mathbf{v}_p = (\mathbf{v}_2 - \mathbf{v}_1) \times (\mathbf{v}_3 - \mathbf{v}_1) / |(\mathbf{v}_2 - \mathbf{v}_1) \times (\mathbf{v}_3 - \mathbf{v}_1)| \quad (1)$$

where  $\mathbf{v}_1$ ,  $\mathbf{v}_2$  and  $\mathbf{v}_3$  are  $\sigma$ -bond unit vectors of the phenine panel. Similar to the POAV definition, the angle ( $\theta_{\sigma p}$ ) between  $\mathbf{v}_p$  and  $\sigma$ -bond vectors is defined as an obtuse angle ( $\theta_{\sigma p} > 90^\circ$ ) so that the vector points to the convex face of the curved phenine panel (Figure 1). The pyramidalization angle is then derived as  $\theta = \theta_{\sigma p} - 90^\circ$ , which quantitatively measures the nonplanarity, *i.e.*, pyramidalization, of the phenine panel. Finally, the  $\mathbf{v}_p$  vector can also define a dihedral angle ( $\phi$ ) between two connected phenine panels, which provides another useful descriptor for the GPF structures. Thus, the  $\theta$  values serve as a measure of the pyramidalizations of the phenine panel, and the  $\phi$  values serve as a measure of the torsions at the phenine linkages.

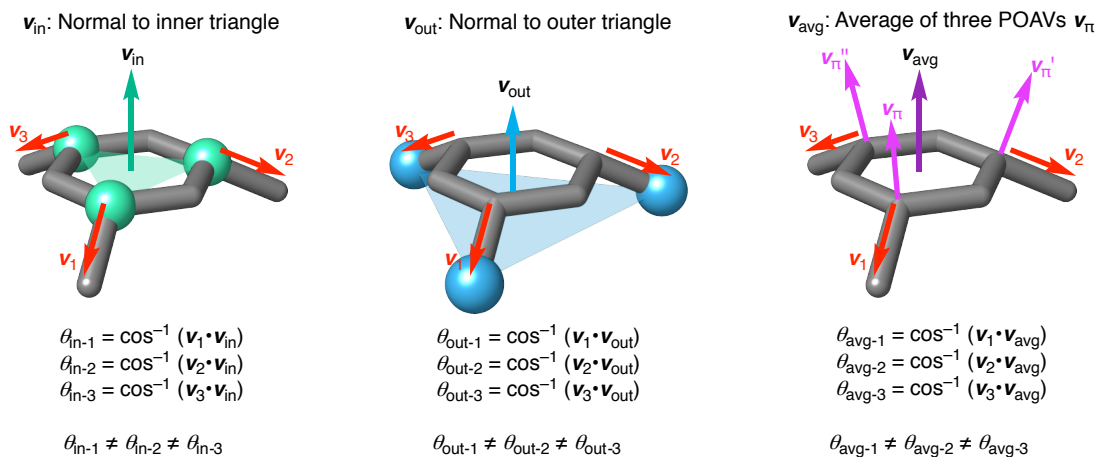


**Figure 2.** Definition of other vectors considered for structural analysis.

### 4.3 Effectiveness of CPNV analysis for phenine nanocarbon structures

The geometry of the GPF hemisphere (**1**) in the time-averaged theoretical structure was first examined by the CPNV measures.<sup>7,9,10</sup> Because the GPF hemisphere possesses an isorecticular network similar to the GPA hemisphere (**5**; Figure 3a), the overall shapes of the two molecules are similar. Thus, these two molecules commonly possess a bowl-like shape with minor warped deformations at peripheral regions of the larger hemisphere (**1**) (Figure 3a). When these structures were analyzed by the POAV measures of the  $\theta$  and  $\phi$  values, differences in the structural details were revealed.<sup>7,11</sup> When the POAV  $\theta$  values within each molecule were examined, the deformation at the central pentagon was visualized with **5** (Figure 3c), whereas the regional localizations of the pyramidalized carbon atoms were not obvious with **1** (Figure 3b). When the POAV  $\theta$  values of **1** and **5** were compared (Figures 3b and 3c), smaller pyramidalizations became apparent for the  $sp^2$ -carbon atoms in **1**, indicating smaller strains forced on each carbon atom.<sup>1,7</sup> Although subtle structural differences became apparent with the POAV analysis, the POAV mappings were not fully successful in disclosing the structural factors that determine the nanoscale molecular shapes. Thus, solely by POAV analysis, the similarity in the bowl-like molecular shape was not found, and the structural anomaly around the warped rim of **1** was not indicated. Such deficiencies were complemented by the CPNV analysis. The CPNV mappings of **1** are shown in Figure 3d. The CPNV  $\theta$  mappings of **1** successfully showed pyramidalization similar to that of **5**, demonstrating the important role of the central pentagon in dictating the bowl-like overall shape. The CPNV  $\phi$  mappings of **1**

also succeeded in highlighting interphenine torsions at the rim regions as an origin to induce warped structural deformations.

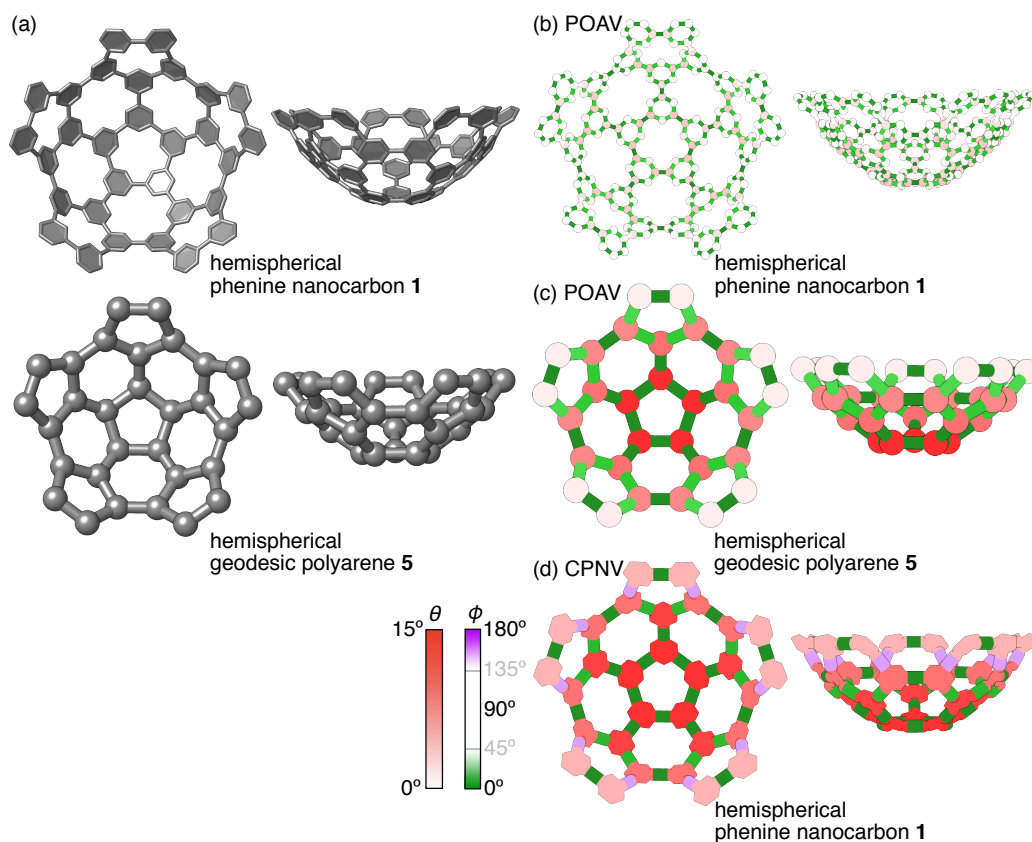


**Figure 3.** POAV and CPNV analyses of the hemispherical nanocarbon and the corresponding phenine nanocarbon. (a) Structure of the hemispherical phenine nanocarbon (**5**) and the corresponding GPA **1**. POAV analysis of (b) **1** and (c) **5**. (d) CPNV analysis of **1**.

#### 4.4 CPNV analysis of phenine nanocarbon molecules

CPNV analysis was then applied to the crystal structures of GPF molecules to reveal important geometric features that determine the unique molecular shapes. The bowl-like shape of the hemisphere (**1**) existed only as the time-averaged structure (Figure 3) and was severely deformed in solution and crystals.<sup>7</sup> The CPNV analysis showed that the deformation was mainly dictated by the interphenine torsions. Two crystal structures of **1** commonly showed subtle yet biased distributions of  $\phi$  values over the molecular structures (Figure 4), which resulted in an oval-like shape. A comparison of CPNV mappings of **1** and **2** showed that an increase of the pentagon networks resulted in an

increase of the phenine pyramidalizations, but the pyramidalizations were not necessarily localized over the pentagons. The pyramidalizations were less pronounced with the heptagon-centered GPF saddle (**3**). The saddle shape at the heptagon omphalos was also visualized by the  $v_p$  vectors pointing toward opposite directions, which was indicated by the dihedral angles colored differently in green and purple. All the GPF molecules including cylindrical **4** exhibited fewer deformed phenine panels located at the edge, indicating that smaller strains were present in these regions.

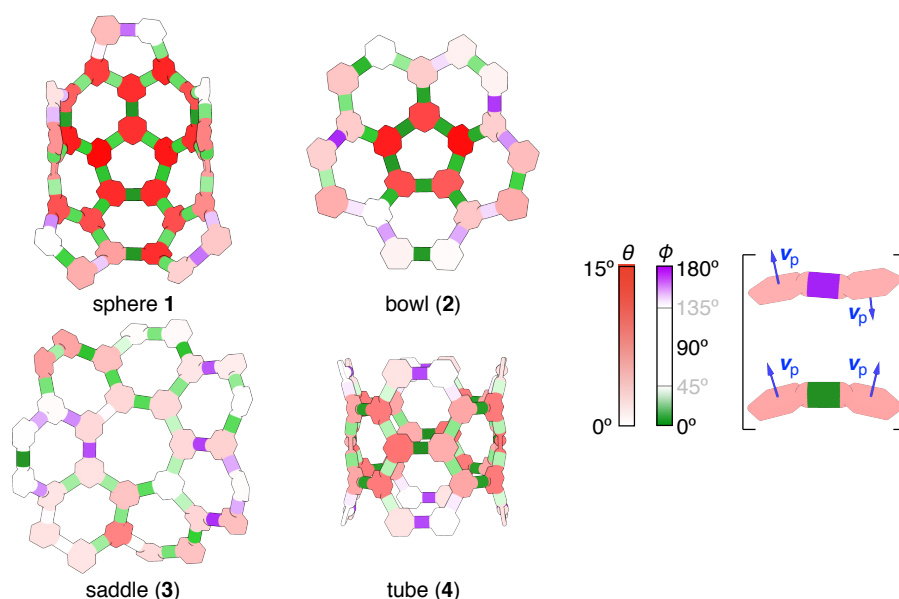


**Figure 4.** CPNV analysis of various phenine nanocarbon molecules.

#### 4.5 Origin of the deformation of the hemispherical phenine nanocarbon molecule

The CPNV mappings can also disclose geometric factors associated with dynamic structural changes of GPF molecules. The dynamic structural changes with **1** and **3** were previously revealed by theoretical calculations, and the fluctuating structures were subjected to CPNV analysis in this study.<sup>7</sup> As suggested by the CPNV mappings of static structures, the overall shapes of the 3-nm molecules were largely dictated by subtle changes in the interphenine torsions (Figures 5 and 6). Unlike the POAV  $\phi$  values, conformational energy minima do not necessarily appear at the CPNV  $\phi$  values of  $0^\circ/180^\circ$ , and the conformational energy does not increase dramatically within the  $\pm 45^\circ$  range of the  $\phi$  values. These features thus resulted in the small  $<1$ -kcal/mol energy barriers for the structural changes of **1** and **3**.<sup>12</sup> The CPNV mappings also revealed an interesting

difference in the pyramid distributions between pentagonal and heptagonal omphaloi. Thus, through the structural fluctuations of the bowl-like hemisphere (1), negligible changes in the pyramidalizations were noted with central regions around the pentagonal omphalos (Figure 5). However, with the wavy fluctuations of the saddle (3), the pyramidalized panels circulated at the heptagonal omphalos along with the torsional changes (Figure 6).

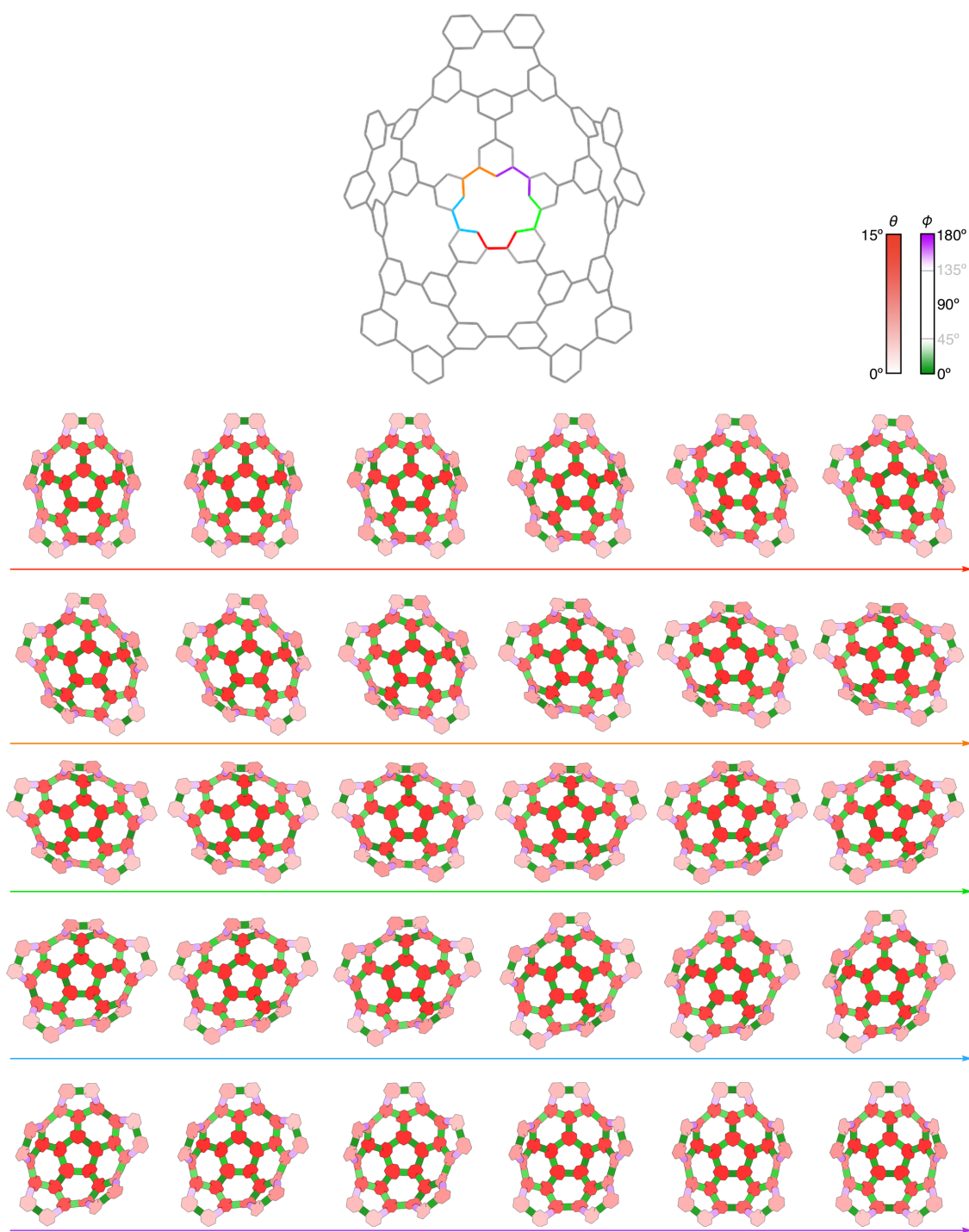


**Figure 5.** CPNV analysis of the structures of the hemispherical phenine nanocarbon during a series of dihedral angle scan calculations of the five biaryl bonds connecting phenine units of the omphalos pentagon.



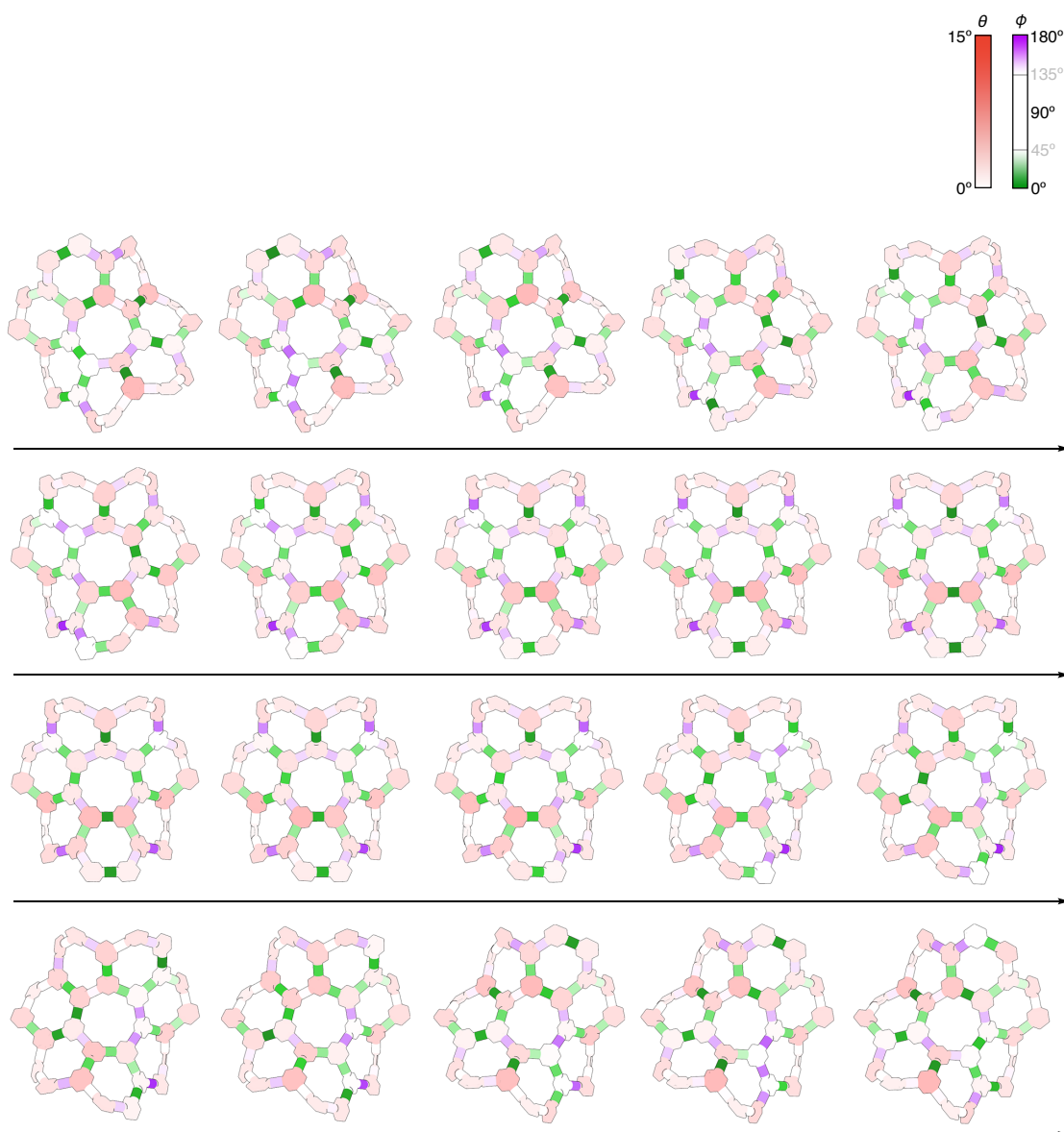


**Figure 6.** CPNV analysis of the structures of the saddle-like [7]circulene phenine nanocarbon **3** during a series of dihedral angle scan calculations. Coordinates originally reported in ref. 5.

#### 4.6 Estimation of physical properties

Finally, interesting correlations between CPNV and electrostatic potentials (ESPs) were found (Figure 7). Curved  $\pi$ -systems of GPAs are known to have biased, different electrostatic potentials, respectively, on convex and concave faces. For instance, the concave ESP surface of corannulene is more negative than that the convex surface.<sup>13</sup>

When we analyzed the ESP mappings of the GPF bowl (**2**) by density functional theory (DFT) calculations of the crystal structure, we found that the concave face was also more negative than the convex face (Figure 7b). Moreover, a comparison of ESP mappings of **2** with its CPNV  $\theta$  mappings showed that the ESP charge is more biased at the pyramidalized phenine panels (Figure 7c and d). For instance, the concave/convex difference of the ESP mappings was more apparent at the five phenine panels of the omphalos than those at the peripheral regions. Such biased charge distributions should be common features of the GPF molecules comprising pyramidalized phenine panels. We believe that the charge biases may also be one of the origins of peculiar solvation behaviors,<sup>14</sup> which dictated entropy-driven molecular assembly at the curved GPF surfaces.<sup>4,5</sup>

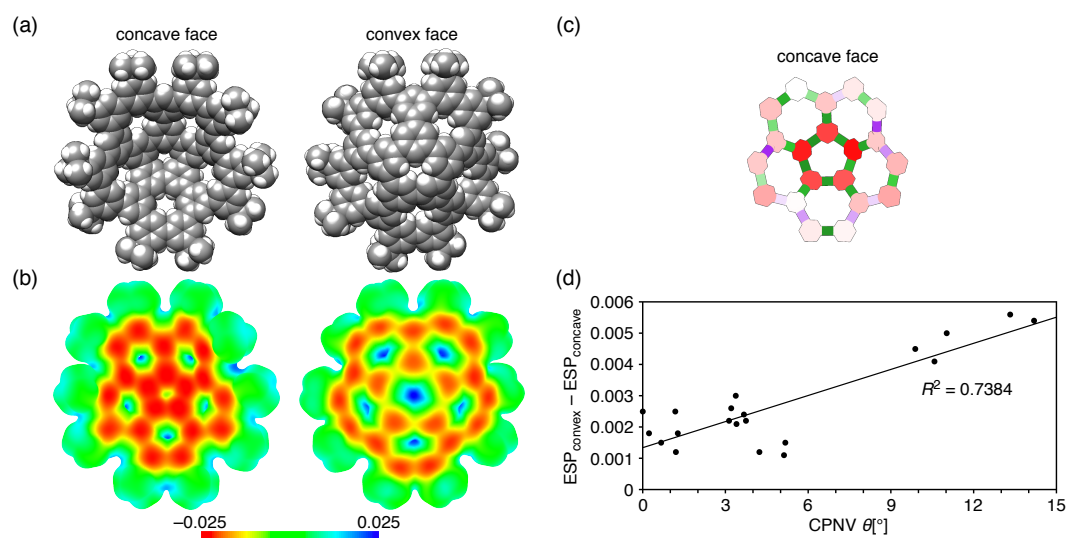


**Figure 7.** (a), (b) ESP mappings of **2** showing space-filling references to clarify molecular shapes. The single-point DFT calculations at B3LYP/6-31G(d,p) level of the theory were performed with the crystal structure to map ESP on an isosurface of 0.0004 a.u. (c) CPNV analysis of the crystal structure. (d) Correlation of CPNV pyramidalizations and ESP differences between the concave and convex faces of phenine units in **2**.

#### 4.7 Automation of CPNV analysis

To perform CPNV/POAV analysis and to visualize the results quickly, correctly and consistently, a plugin was created to be embedded in the UCSF Chimera<sup>15</sup> molecular modelling application. The structures in this chapter colored by CPNV/POAV  $\theta/\varphi$  were

rendered with the application and plugin. The plugin works by changing color of atoms/bonds depending on the  $\theta/\varphi$  values, with white representing  $\theta = 0^\circ$  and red  $\theta = 15^\circ$  for pyramidalization, and green representing  $\varphi = 0^\circ$ , purple  $\varphi = 180^\circ$  and white  $\varphi = 45-135^\circ$  for torsion. Atoms with  $\theta$  between  $0^\circ$  and  $15^\circ$ , and bonds with  $\varphi$  between  $0^\circ$  and  $45^\circ$ , and  $135^\circ$  and  $180^\circ$  were colored by interpolation in an RGB color space based on the above-mentioned reference points. Chimera's lighting mode was set to "ambient" to render the molecule with accurate colors by eliminating the effect of shades and shadows. In addition to this plugin, a standalone Python program which outputs the results of CPNV/POAV analysis to stdout was created. Its details are provided in the Methods section below.

## 4.8 Conclusion

In summary, a method was developed for quantitative structural evaluations of large, nanoscale molecules composed of phenine panels. Structural strains such as pyramidalized phenine panels and twisted interphenine torsions were easily located by the CPNV analysis. Furthermore, the quantitative CPNV values of pyramidalization and torsion angles provide geometric measures complementary to those of POAV analysis,<sup>1</sup> and the geometric analyses unveiled the similarity and difference between larger and smaller trigonal planar units (*i.e.*, phenine *vs.*  $sp^2$ -carbon). The correlations between phenine pyramidalizations and electrostatic potentials demonstrated interesting features of the CPNV analysis, which should be useful in designing supramolecular structures with GPF molecules. It is expected that CPNV measures can facilitate the design and comparison of the geodesic structures of phenines, which should also accelerate the development of unique nonplanar aromatic molecules.<sup>16</sup>

## 4.9 Supplementary data

### Coordinates

Coordinates of GPF molecules were taken from literatures: **1** and **5** = ref. 7, **2** = ref. 4a, **3** = ref. 5, **4** = ref. 6a.

### Models

Molecular models were constructed by using UCSF Chimera<sup>15</sup>. Phenine panels

were colored based on  $\theta$  by linear interpolation in RGB color space between white (FF, FF, FF) and red (FF, 00, 00) with the fraction value  $\theta/15^\circ$  for  $0^\circ \leq \theta \leq 15^\circ$  and 1 for  $\theta > 15^\circ$ . Biaryl bonds were similarly colored based on  $\varphi$  by interpolation between green (22, 8B, 22; for  $\varphi \leq 45^\circ$ ) and white, or purple (A0, 20, F0; for  $\varphi \geq 135^\circ$ ) and white, with the fraction values  $\varphi/45^\circ$  and  $(180^\circ - \varphi)/45^\circ$ . Bonds with  $45^\circ < \varphi < 135^\circ$  were colored in white. Panels representing aromatic rings were displayed using the fill thick option of the program. The radius of biaryl bonds were set to 0.6 for clarity without the "halfbond mode" being applied. The "ambient" lighting mode was employed to clarify the color.

### POAV analysis

The POAV was originally proposed in 1986,<sup>17</sup> and calculation tools for the  $\theta$  values were provided in a form of Excel spreadsheet.<sup>18,19</sup> However, the method was not readily applicable to large molecules such as GPF molecules exceeding 120  $\text{sp}^2$ -carbon atoms. We thus developed a python code (poav.py, List 1) to derive both  $\theta$  and  $\varphi$  values from Cartesian coordinates in a form of PDB format. The poav.py application depends on, and should be used along with, RDKit.<sup>20</sup>

### CPNV analysis

I developed python applications to derive  $\theta$  and  $\varphi$  values of the POAV/CPNV analysis with Cartesian coordinates in a form of PDB format. The cpnv.py application (List 2) depends on, and should be used along with, RDKit.<sup>20</sup>

#### **List 1.** Poav.py.

```
from rdkit import Chem

import sys

import math

def dihedral(v12, v23, v34):

    n1 = v12.CrossProduct(v23)

    n1.Normalize()

    n2 = v23.CrossProduct(v34)

    n2.Normalize()

    phi = math.degrees(math.acos(n1.DotProduct(n2)))

    if (n1.CrossProduct(n2).DotProduct(v23) < 0:
```

```

        return phi * -1
    else:
        return phi

def calculatePoav(cent, a1, a2, a3):
    v1 = a1 - cent
    v2 = a2 - cent
    v3 = a3 - cent
    v1.Normalize()
    v2.Normalize()
    v3.Normalize()
    poav = (v2-v1).CrossProduct(v3-v1)
    poav.Normalize()
    if v1.DotProduct(poav) > 0:
        poav = poav* -1
    theta = math.degrees(math.acos((v1.DotProduct(poav) + v2.DotProduct(poav) +
                                                                              v3.DotProduct(poav))/3)) - 90

    return poav, theta

def GetThetaPhiValues(mol):
    sp2carbons = [atom for atom in mol.GetAtoms() if len(atom.GetNeighbors()) == 3]
    ths = list()
    poavtable = dict()
    for atom in sp2carbons:
        idx = atom.GetIdx()
        nbrpos = [mol.GetConformer().GetAtomPosition(nbr.GetIdx()) for nbr in
atom.GetNeighbors()]
        centpos = mol.GetConformer().GetAtomPosition(idx)
        poav, theta = calculatePoav(centpos, nbrpos[0], nbrpos[1], nbrpos[2])
        ths.append((idx, theta))
        poavtable[idx] = poav
    phs = list()
    for bond in mol.GetBonds():
        a1 = bond.GetBeginAtomIdx()
        a2 = bond.GetEndAtomIdx()

```

```

        if (a1 in poavtable) and (a2 in poavtable):

            v23 = mol.GetConformer().GetAtomPosition(a2) -
mol.GetConformer().GetAtomPosition(a1)

            phs.append((a1, a2, dihedral(poavtable[a1] * -1, v23, poavtable[a2])))

    return ths, phs

# Main

if len(sys.argv) != 2:

    print("Invalid number of arguments")

    sys.exit(1)

tgt = Chem.rdmolfiles.MolFromPDBFile(sys.argv[1], sanitize=True, removeHs=False,

proximityBonding=True)

thetas, phis = GetThetaPhiValues(tgt)

print(" Atom | Theta (deg)")

for theta in thetas:

    print(f"{theta[0]+1:>5d} | {theta[1]:>5.2f}")

print("")

print("      Bond      | Phi (deg)")

for phi in phis:

    print(f"{phi[0]+1:>5d} {phi[1]+1:>5d} | {abs(phi[2]):>6.2f}")

```

## ***List 2.*** Cpnv.py.

```

from rdkit import Chem

import sys

import math

class Phenine:

    def __init__(self, parentmol, memberindices):

        self.parent = parentmol

        self.indices = memberindices

        atoms = [parentmol.GetAtomWithIdx(i) for i in memberindices]

        nbr = []

        for atom in atoms:

            outsidenbr = [n for n in atom.GetNeighbors() if n.GetIdx() not in memberindices]

            nbr.append(outsidenbr[0] if len(outsidenbr)==1 else None)

```

```

# based on nbr[0], we determine if the bonding pattern is (1,3,5) or (2,4,6).

# for this method to work, memberindices are required to be given in order.

if (nbr[0] is not None and nbr[0].IsInRingSize(6)) or (nbr[2] is not None and
nbr[2].IsInRingSize(6)):

    self.biarylatoms = memberindices[0::2]

    self.chatoms = memberindices[1::2]

    self.neighbors = [n.GetIdx() for n in nbr[0::2]]

else:

    self.biarylatoms = memberindices[1::2]

    self.chatoms = memberindices[0::2]

    self.neighbors = [n.GetIdx() for n in nbr[1::2]]

self.biarylcoords = [parentmol.GetConformer().GetAtomPosition(idx) for idx in
                                                                self.biarylatoms]

self.chcoords = [parentmol.GetConformer().GetAtomPosition(idx) for idx in self.chatoms]

self.neighborcoords = [parentmol.GetConformer().GetAtomPosition(idx) for idx in
                                                                self.neighbors]

self.Cpnv, self.Theta = self.calculateCpnv()

def calculateCpnv(self):

    v1 = self.neighborcoords[0] - self.biarylcoords[0]

    v2 = self.neighborcoords[1] - self.biarylcoords[1]

    v3 = self.neighborcoords[2] - self.biarylcoords[2]

    v1.Normalize()

    v2.Normalize()

    v3.Normalize()

    cpnv = (v2-v1).CrossProduct(v3-v1)

    cpnv.Normalize()

    if v1.DotProduct(cpnv) > 0:

        cpnv = cpnv* -1

    theta = math.degrees(math.acos((v1.DotProduct(cpnv) + v2.DotProduct(cpnv) +
                                                                v3.DotProduct(cpnv))/3)) - 90

    return cpnv, theta

@staticmethod

def GetPhenines(mol):

```

```

rings = [[atom for atom in ring] for ring in mol.GetRingInfo().AtomRings()

if len(ring)==6]

return [Phenine(mol, lst) for lst in rings]

@staticmethod
def dihedral(v12, v23, v34):
    n1 = v12.CrossProduct(v23)
    n1.Normalize()
    n2 = v23.CrossProduct(v34)
    n2.Normalize()
    phi = math.degrees(math.acos(n1.DotProduct(n2)))
    if (n1.CrossProduct(n2).DotProduct(v23) < 0:
        return phi * -1
    else:
        return phi

@staticmethod
def GetThetaPhiValues(mol):
    phenines = Phenine.GetPhenines(mol)
    ths = [(phenine.indices, phenine.Theta) for phenine in phenines]
    phs = list()
    phtable = dict([(ba, phenine.Cpnv) for phenine in phenines for ba in
phenine.biarylatoms])
    for bond in mol.GetBonds():
        a1 = bond.GetBeginAtomIdx()
        a2 = bond.GetEndAtomIdx()
        if (a1 in phtable) and (a2 in phtable):
            v23 = mol.GetConformer().GetAtomPosition(a2) -
mol.GetConformer().GetAtomPosition(a1)
            phs.append((a1, a2, Phenine.dihedral(phtable[a1] * -1, v23, phtable[a2])))
    return ths, phs

# Main
if len(sys.argv) != 2:
    print("Invalid number of arguments")

```



```

sys.exit(1)

tgt = Chem.rdmolfiles.MolFromPDBFile(sys.argv[1], sanitize=True, removeHs=False,
                                     proximityBonding=True)

thetas, phis = Phenine.GetThetaPhiValues(tgt)

print("      Ring (Atom Serial Numbers)      | Theta (deg)")

for theta in thetas:
    print(f"{theta[0][0]+1:>5d} {theta[0][1]+1:>5d} {theta[0][2]+1:>5d} {theta[0][3]+1:>5d}
          {theta[0][4]+1:>5d} {theta[0][5]+1:>5d} | {theta[1]:>5.2f}")

print("")

print("      Bond      | Phi (deg)")

for phi in phis:
    print(f"{phi[0]+1:>5d} {phi[1]+1:>5d} | {abs(phi[2]):>6.2f}")

```

#### 4.10 References

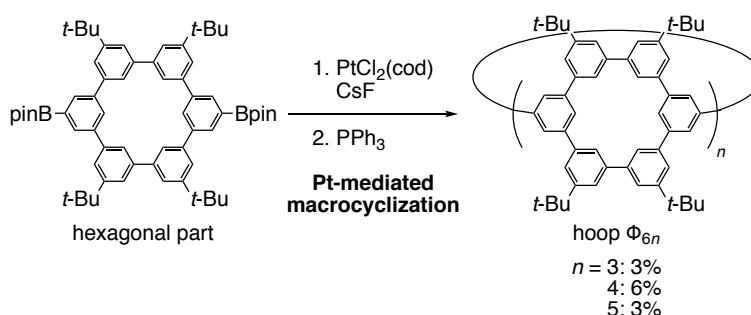
1. (a) R. C. Haddon, L. T. Scott, *Pure Appl. Chem.* **1986**, *58*, 137-142. (b) R. C. Haddon, *Acc. Chem. Res.* **1988**, *21*, 243-249. (c) R. C. Haddon, *Science* **1993**, *261*, 1545-1550. (d) R. C. Haddon, *J. Phys. Chem. A* **2001**, *105*, 4164-4165.
2. (a) V. M. Tsefrikas, L. T. Scott, *Chem. Rev.* **2006**, *106*, 4868-4884. (b) Y. Segawa, H. Ito, K. Itami, *Nat. Rev. Mater.* **2016**, *1*, 1-14.
3. (a) R. C. Haddon, *J. Am. Chem. Soc.* **1990**, *112*, 3385-3389. (b) H. Sakurai, T. Daiko, H. Sakane, T. Amaya, T. Hirao, *J. Am. Chem. Soc.* **2005**, *127*, 11580-11581. (c) E. S. Hirst, F. Wang, R. Jasti, *Org. Lett.* **2011**, *13*, 6220-6223. (d) H. Yokoi, Y. Hiraoka, S. Hiroto, D. Sakamaki, S. Seki, H. Shinokubo, *Nat. Commun.* **2015**, *6*, 8215.
4. (a) K. Ikemoto, R. Kobayashi, S. Sato, H. Isobe, *Angew. Chem. Int. Ed.* **2017**, *56*, 6511-6514. (b) K. Ikemoto, R. Kobayashi, S. Sato, H. Isobe, *Org. Lett.* **2017**, *19*, 2362-2365.
5. K. Ikemoto, J. Lin, R. Kobayashi, S. Sato, H. Isobe, *Angew. Chem. Int. Ed.* **2018**, *57*, 8555-8559.
6. (a) Z. Sun, K. Ikemoto, T. M. Fukunaga, T. Koretsune, R. Arita, S. Sato, H. Isobe, *Science* **2019**, *363*, 151-155. (b) Z. Sun, T. Mio, K. Ikemoto, S. Sato, H. Isobe, *J. Org. Chem.* **2019**, *84*, 3500-3507.
7. T. Mio, K. Ikemoto, S. Sato, H. Isobe, *Angew. Chem. Int. Ed.* **2020**, *59*, 6567-6571.
8. H. Kenner, *Geodesic Math and How to Use It*, 2nd ed., University of California Press, Berkeley, **2003**.
9. We provide python codes for the POAV/CPNV analysis in Supporting Information.
10. E. F. Pettersen, T. D. Goddard, C. C. Huang, G. S. Couch, D. M. Greenblatt, E. C. Meng, T. E. Ferrin, *J. Comput. Chem.* **2004**, *25*, 1605-1612.
11. For clarity and consistency, color codes for the POAV analysis were revised and improved from the previous study (ref. 7).
12. For instance, see: (a) E. L. Eliel, S. H. Willen, *Stereochemistry of Organic Compounds*, Wiley, New York, **1994**; (b) P. Sarkar, Z. Sun, T. Tokuhira, M. Kotani, S. Sato, H. Isobe, *ACS Cent. Sci.* **2016**, *2*, 740-747; (c) Z. Sun, T. Matsuno, H. Isobe, *Bull. Chem. Soc. Jpn.* **2018**, *91*, 907-921.
13. S. Mizyed, P. E. Georghiou, M. Bancu, B. Cuadra, A. K. Rai, P. Cheng, L. T. Scott, *J. Am. Chem. Soc.* **2001**, *123*, 12770-12774.

14. C. I. Wang, C. C. Hua, S. A. Chen, *J. Phys. Chem. B*, **2014**, *118*, 9964-9973.
15. E. F. Pettersen, T. D. Goddard, C. C. Huang, G. S. Couch, D. M. Greenblatt, E. C. Meng, T. E. Ferrin, *J. Comput Chem.* **2004**, *25*, 1605-1612.
16. M. Ball, Y. Zhong, Y. Wu, C. Schenck, F. Ng, M. Steigerwald, S. Xiao, C. Nuckolls, *Acc. Chem. Res.* **2015**, *48*, 267-276.
17. R. C. Haddon, L. T. Scott, *Pure Appl. Chem.* **1986**, *58*, 137-142.
18. R. C. Haddon, *J. Phys. Chem. A* **2001**, *105*, 4164-4165.
19. <http://carbonsolution.com>
20. <https://www.rdkit.org>

## Chapter 5. Summary

Precisely synthesized nanocarbon molecules have been important for investigating the characteristics of nanocarbon materials in detail. Since the discovery of fullerenes and carbon nanotubes, increasingly various nanocarbon molecules have been designed and synthesized through different methods. However, chemical synthesis of molecular nanocarbons is still a significant challenge. Recently, the concept of phenine nanocarbons were introduced, which is potentially an efficient way to synthesize large nanocarbon molecules through reliable coupling reactions, though the scope of accessible structures was limited with the original strategy. In this thesis, a new strategy called the polygon assembling strategy was introduced to increase the structural diversity of phenine nanocarbons. In the strategy, preformed polygonal parts of  $[n]$ CMP are assembled in late stages of the synthesis.

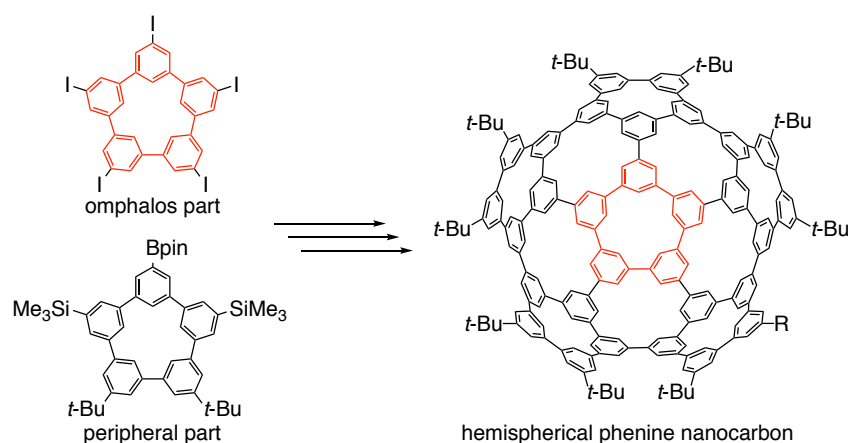
In **Chapter 2**, the strategy was applied to synthesis of hoop-shaped molecules isoreticular to  $[n]$ CPP. A hexagonal part comprising six phenine units was first synthesized by coupling reactions, and it was assembled into a hoop by Pt-mediated macrocyclization, which afforded **hoop  $\Phi_{6n}$**  molecules with  $n = 3, 4$  and  $5$  hexagonal panels with 3%, 6% and 3% yield, respectively (Scheme 1). A combination of NMR spectroscopy, UV-vis spectroscopy, crystallography and conformation search calculations revealed that their structural rigidity depended on the panel number, with smaller congeners being more rigid. In addition, a Job plot analysis showed that the four-paneled congener **hoop  $\Phi_{24}$**  was found to encapsulate  $C_{70}$  with 1:1 stoichiometry, while the crystal structure of the complex indicated 1:3 stoichiometry.



**Scheme 1.** Hexagons assembled into hoop-shaped phenine nanocarbons.

In **Chapter 3**, the strategy was applied to a hemispherical phenine nanocarbon

molecule isoreticular to a  $C_{5v}$  bisection of buckminsterfullerene. The molecule was synthesized by assembling the omphalos pentagonal part and the peripheral pentagonal part with an overall yield of 5.7% for the longest route (Scheme 2). While spectroscopic analysis indicated the expected high symmetry of  $C_{5v}$ , its crystal structure showed an ovally deformed structure. The discrepancy was explained by rapid structural fluctuation to symmetrize the time-averaged structure revealed by theoretical calculations.



**Scheme 2.** Pentagons assembled into the hemispherical phenine nanocarbon.

In **Chapter 4**, a method to quantitatively describe the deformation of phenine nanocarbon structures was developed (Figure 1). The method measures the pyramidalization of a phenine unit and the torsion between two phenine units by establishing a vector called CPNV for each phenine unit, which forms an equal angle with three biaryl bonds around the unit. The new analytic method allows structural analysis with a resolution of phenine units rather than  $sp^2$ -carbon atoms, and more effective than the conventional POAV analysis in depicting structural features of phenine nanocarbons.

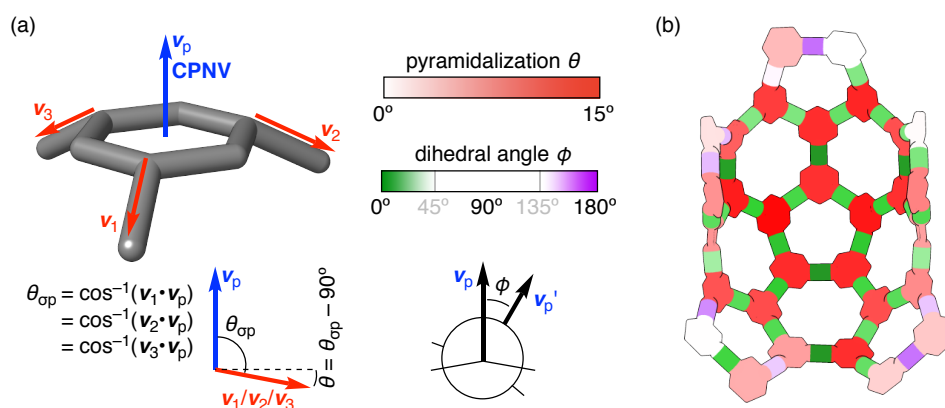


**Figure 1.** (a) Definition of CPNV  $\theta$  and  $\phi$ . (b) CPNV analysis of the crystal structure of the hemispherical phenine nanocarbon.

Through the synthesis of new phenine nanocarbon structures by the polygon assembling strategy (Chapters 2 and 3), the structural diversity of phenine nanocarbons was increased. With the synthesized compounds, the behavior of phenine nanocarbon structures were revealed in detail, which verified their potential as models of large and curved nanocarbon structures. Combined with the CPNV analysis (Chapter 4), which can be useful in designing and evaluating new phenine nanocarbon molecules, the synthetic strategy developed in this thesis is expected to boost the studies on nanocarbons by assisting synthesis of new phenine nanocarbons.

## List of Publications

"Synthesis, structures and assembly of geodesic phenine frameworks with isorecticular networks of [n]cyclo-para-phenylenes"

Sun, Z.; Mio, T.; Ikemoto, K.; Sato, S.; Isobe, H. *J. Org. Chem.* **2019**, *84* (6), 3500-3507.  
(Chapter 2)

"Synthesis of a hemispherical geodesic phenine framework via a polygon assembling strategy"

Mio, T.; Ikemoto, K.; Sato, S.; Isobe, H. *Angew. Chem. Int. Ed.* **2020**, *59* (16), 6567-6571.  
(Chapter 3)

"Curved phenine normal vectors: Geometric measures of geodesic phenine frameworks"

Mio, T.; Ikemoto, K.; Isobe, H. *Chem. Asian J.* **2020**, *15* (8), 1355-1359.  
(Chapter 4)

## Other publications

"Unbiased rotational motions of an ellipsoidal guest in a tight yet pliable host"

Sun, Z.; Mio, T.; Okada, T.; Matsuno, T.; Sato, S.; Kono, H.; Isobe, H.  
*Angew. Chem. Int. Ed.* **2019**, *58* (7), 2040-2044.

## Acknowledgments

I wish to express my profound gratitude for Professor Hiroyuki Isobe not only for providing the environment and the facilities but also for guiding me for the entire six years of my academic career full of difficulties. Without any of these, my works, including this thesis, would have never existed.

I must show my enormous appreciation to Professor Sun Zhe, Professor Sota Sato, Dr. Koki Ikemoto and Dr. Taisuke Matsuno for their continuous support through discussion and detailed advice that allowed my research to proceed. I owe the development of my scientific skills, both of experiments and of presentation, to theirs and their education.

I am also grateful to every current and former member of the research group, who supported me in direct and indirect ways, for allowing me to enjoy my life in the laboratory. I was able to continue my research for six years there, because the time spent with them was comfortable.

I thank SPring-8 and KEK for granting access to their synchrotron radiation facilities, without which many of the crystal structures in this thesis would not be available.

I thank Japan Society for the Promotion of Science for the generous financial support that enabled my research.

Finally, I would like to thank my parents for their financial and psychological support.

Tokyo, Japan  
December 20<sup>th</sup>, 2021  
**Tatsuru Mio**

Department of Chemistry  
The University of Tokyo